Implementing electrochemical phenomena in porous materials for the improvement of the conversion of heat into electricity

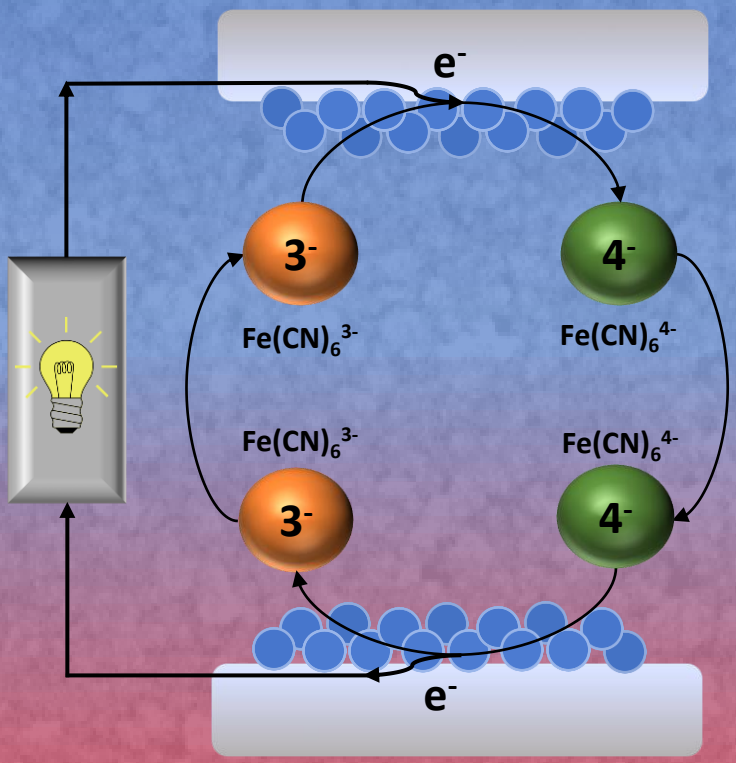

Author

Sergio Castro Ruiz

Supervised by

Dr. Jorge García Cañadas

Castelló de la Plana, April 2024

UNIVERSITAT JAUME·I

Programa de Doctorado en Tecnologías Industriales y Materiales

Escuela de Doctorado de la Universitat Jaume I

Implementing electrochemical phenomena in porous materials for the improvement of the conversion of heat into electricity

Memoria presentada por Sergio Castro Ruiz para optar al grado de doctor por la Universitat Jaume I

Author:

Sergio Castro Ruiz

CASTRO RUIZ SERGIO - 20064871Q

Firmado digitalmente por CASTRO RUIZ SERGIO - 20064871Q
Fecha: 2024.04.23 12:45:13 +02'00'

Supervised by:

Dr. Jorge García Cañadas

JORGE GARCIA CAÑADAS - NIF:02650058K

Firmado digitalmente por JORGE GARCIA CAÑADAS - NIF:02650058K
Fecha: 2024.04.23 12:59:29 +02'00'

Castelló de la Plana, April 2024

Financial support

This research has received funding from the European Union's Horizon 2020 research and innovation programme under grant agreement No 863222 (UncorrelaTEd project).

This presentation reflects only the author's view and that the funding Agency is not responsible for any use that may be made of the information it contains.

Thesis by compendium of publications

1. S. Castro-Ruiz, J. García-Cañadas. Impedance spectroscopy analysis of a thermo-electrochemical cell under operating conditions. 2022 International Workshop on Impedance Spectroscopy (IWIS), 25-27 (2022). DOI: 10.1109/IWIS57888.2022.9975126.
2. S. Castro-Ruiz, L. Márquez-García, M. Solís-de la Fuente, B. Beltrán-Pitarch, A. Mota-Babiloni, F. Vidan, P. Íñigo-Rabinal, G. Guisado-Barrios and J. García-Cañadas. Power factor improvement in a solid–liquid thermoelectric system formed by $Sb:SnO_2$ in contact with a chromium complex solution. Sustainable Energy & Fuels 7, 4254-4259 (2023). DOI: 10.1039/d3se00622k.
3. S. Castro-Ruiz, J. García-Cañadas. Nanostructured and porous antimony-doped tin oxide as electrode material for the heat-to-electricity energy conversion in thermo-electrochemical cells. Electrochemistry Communications 161, 107683-107689 (2024). DOI: 10.1016/j.elecom.2024.107683.
4. S. Castro-Ruiz, J. García-Cañadas. Evaluation of in-plane architecture in a thermo-electrochemical cell with nanostructured and porous $Sb:SnO_2$ electrodes. Electrochemistry Communications. Under review.

"This thesis has been accepted by the co-authors of the publications listed above that have waved the right to present them as part of another PhD thesis"

Agradecimientos (Acknowledgements)

Tras tres años y medio desde que mudé a Castellón (aún me parece increíble), puedo decir que mi camino hacia el doctorado está a punto de concluir. Por ello, me gustaría agradecer a todas las personas que han participado de una forma u otra en esta tesis.

En primer lugar, tengo que expresar mis más sinceros y profundos agradecimientos a mi director de tesis Jorge. Sé que no hemos estado de acuerdo en muchas cosas durante esta investigación. Sin embargo, tras más de tres años trabajando juntos puedo decir con toda seguridad que, sabiendo mis virtudes y defectos no podría haber tenido un mejor director para mi tesis doctoral. Has estado ahí para resolver todas mis dudas tanto profesional como personalmente manteniendo la calma en todo momento, sabiendo guiarme para mejorar como científico y, lo que es más importante, como persona. Gracias por la oportunidad que me concediste aquel noviembre de 2020 al hacerme la entrevista.

Estos años no habrían sido lo mismo sin mis compañeros de TESLab. Mauricio, qué decir de ti si te has convertido en mi hermano mayor. Podría escribir otra tesis doctoral llena de anécdotas y buenos momentos que hemos compartido durante este tiempo. El único pero que puedo ponerte es que has dejado el listón de compañero de trabajo (y amigo) demasiado alto para cualquier otra persona que llegue en el futuro. Por otro lado, tengo que dar mis más sinceras gracias a Lourdes (The film's master of the group) que ha sido la persona que, a nivel experimental más me ha ayudado durante la tesis. Para una persona como yo que tiene dos manos izquierdas en el laboratorio, has sido de una ayuda increíble todo este tiempo (aunque no lo creas, sigo tus consejos). Of course, I have to thank Opu who arrived after 2 years to carry out his own thesis. Brother, you got integrated into the group environment since the first day and I have learnt a lot of (spicy) Bengali language and food from you. También gracias a los alumnos Marc y Víctor.

Además de mi grupo de laboratorio, durante este tiempo he podido conocer personas maravillosas de las cuales me llevo una amistad increíble. En este sentido, el pasillo donde trabajo me ha llevado a conocer al grupo de Víctor Sans con los cuales he entablado una amistad que espero dure mucho tiempo. Especiales agradecimientos en este sentido a Marci, Gianluca y Sara (aunque ya no vengas a verme) con los que me he relacionado especialmente. Además, gracias también a los demás miembros del INAM que he conocido en mi edificio de trabajo especialmente a Judith, mi compi de gimnasio. Por último, dar gracias a todo el grupo PIMA a los cuales no veo dado que trabajan en otro edificio pero que, cada vez que puedo, me escapo a visitar. En concreto, gracias a Fran por haberme escuchado y aconsejado más de una vez (y de dos, y de tres) cuando no iban bien las cosas.

No solamente en el trabajo se hacen amigos. En este sentido, Castellón me ha dado dos de las mejores personas que jamás he conocido: Cristian y Sonia. Gracias a ambos por vuestra inestimable amistad y compañía, aunque no quedemos mucho por falta de tiempo. Espero seguir siempre en contacto con vosotros.

La marcha a Castellón trajo consigo la distancia con mis amigos de Sevilla. En este sentido, mi carrera de química me llevó a conocer a Cinta y Valle los cuales considero

dos de mis mejores amigos y dos personas muy importantes en mi vida. Además, me gustaría agradecer a Miguel Ángel Partal García por ser la persona (y amigo) que literalmente ``sacó el químico que yo llevaba dentro´´ cuando me empezó a dar clases particulares de química en segundo de bachillerato. Colega, te pasaste el juego porque de un químico de bachiller sacaste a un doctor especializado en termo-electroquímica.

En el ámbito familiar, tengo agradecer desde lo más profundo mi corazón, el apoyo que me han brindado durante estos años tanto mis padres como mi hermano. Papá, quién te iba a decir que aquel niño de 7-8 años que arreglaba televisores contigo sería doctor 20 años después y, además, utilizando los conocimientos de electricidad y soldadura que me enseñaste. Ahora soy yo quién te enseña conceptos sobre impedancias y circuitos eléctricos a ti. Mamá, si de algo estoy orgulloso es de la gran relación que tenemos actualmente. Aunque no siempre te lo diga, te admiro por el esfuerzo que llevas a cabo en el día a día después de todo lo que has pasado. Más de uno habría abandonado a mitad del camino mientras que tú sigues mejorando a diario como persona. Te echo de menos (sobre todo en los desayunos). También gracias a mi hermano Alberto. Tras muchos años llevándonos como el perro y el gato, me he dado cuenta de que somos las dos caras de una misma moneda que, aun siendo diferentes actúan de contrapeso la una de la otra, resultando en un equilibrio perfecto. Gracias por cuidar de mamá, de Ahri (mi amada perrita que siempre me espera cuando bajo) y de la abuela Fina. En este sentido, aunque ya no esté entre nosotros, tengo que dar las gracias a mi abuela Fina (**LA ABUELA**) por el amor brindado desde que nací hasta que te marchaste a mediados de este doctorado. Eres y serás única y siempre te llevaré conmigo gracias al colgante que me dejaste. También quiero dar las gracias a mi abuela Lola por los besos y abrazos que me da cada vez que bajo y nos vemos. Ya quisiera yo tener para mí el apetito que tú tienes, abuela.

Seguidamente, me gustaría hacer dos menciones especiales. En primer lugar, gracias a The Beatles por ser la mejor banda de música de la historia (aunque Jorge no opine igual) y poner música a cada día de mi vida. ¡Quién me iba a decir que se publicaría una canción de ellos en 2023! Finalmente, gracias a Eiichiro Oda por haber creado One Piece que es la mayor, mejor y más absoluta obra maestra de la literatura japonesa (con permiso de Dragon Ball) donde cada capítulo es mejor que el anterior. A veces llegué a pensar que Luffy encontraría el One Piece antes de que yo terminase el doctorado. Por suerte, lo segundo ha ocurrido antes que lo primero.

Lo mejor para el final dicen. Por ello, quiero darte las gracias a ti María, a mi bubu. Vine a Castellón con la mente abierta al conocimiento científico, pero con el corazón cerrado al amor. Si lo primero se ha cumplido con creces, con lo segundo he superado unas expectativas que nunca llegué a imaginar al conocer a mi compañera de vida, mi alma gemela y, si Chuck (*nuestro único y verdadero Dios*) quiere, la mujer con la que formaré una familia. Me has apoyado cada día, querido, aconsejado y escuchado sin importar que tuvieras asuntos propios que tratar en ese momento. Si he podido sobrevivir a la montaña rusa que ha sido esta tesis, ha sido en gran parte por ti. Te amo cada día más.

Gracias también a sus padres, José Manuel y Ana por acogerme en su casa como uno más de su familia cada vez que bajamos a Orihuela.

La correcta comprensión de la frase que se expone a continuación ofrece, desde el punto de vista del autor de esta tesis doctoral, la clave para llegar a ser un buen investigador científico.

A correct understanding of the phrase written below offers, from the point of view of the author of this doctoral thesis, the key to be a valuable scientific researcher.

``La verdadera ciencia es aquella que se realiza fuera del laboratorio´´

``Real science is done outside of the laboratory´´

Sergio Castro Ruiz

List of abbreviations and symbols

TE	Thermoelectric
η_{TE}	Thermoelectric efficiency
zT	Dimensionless figure of merit
S	Seebeck coefficient
σ	Electrical conductivity
κ	Thermal conductivity
T	Temperature
PF	Thermoelectric power factor
ATO	Antimony-doped tin oxide
BMI-I	1-butyl-3-methylimidazolium iodide
TEC	Thermo-electrochemical cell
PEDOT:PSS	Poly(3,4-ethylenedioxythiophene)-poly(styrenesulfonate)
IS	Impedance spectroscopy
α	Temperature coefficient
κ_L	Lattice thermal conductivity
3-MPN	3-methoxypropionitrile
V_{oc}	Open-circuit voltage
P_{out}	Power output (W) or power output density (W/m^2)
SEM	Scanning electron microscopy
XRD	X-ray diffraction
ΔT	Temperature difference
T_C	Cold side temperature
T_H	Hot side temperature
Q_P	Cooling/heater power
I	Electrical current
Π	Peltier coefficient
Q_T	Absorbed/released heat power
β	Thomson coefficient
z	Figure of merit
COP	Coefficient of performance
n	Charge carriers concentration
ΔV_{Load}	Voltage difference across the load
R_{Load}	Load resistance

R_Ω	Ohmic resistance
P_{max}	Maximum power output (W) or maximum power output density (W/m^2)
Q_{in}	Incident heat power
η_{Max}	Maximum thermoelectric efficiency
T_{avg}	Average temperature
η_C	Carnot efficiency
R	Film electric resistance
E_{Redox}	Redox potential
ΔG_{Redox}	Gibbs free energy
F	Faraday constant
ΔH_{Redox}	Redox enthalpy
ΔS_{Redox}	Redox entropy
$\Delta S_{Partial}$	Partial molar entropy
$\Delta S_{Eastman}$	Eastman entropy
$\Delta S_{Electrons}$	Electrons entropy
ΔS_{Red}	Reduced form partial molar entropy
ΔS_{Ox}	Oxidized form partial molar entropy
ΔS_{Solv}	Solvation entropy
ε	Solvent dielectric constant
r	Ionic radii
z_{Ox}	Oxidized form charge
z_{Red}	Reduced form charge
e	Electron charge
N_A	Avogrado's number
R_{dc}	Total resistance
R_s	Series resistance
R_{ct}	Charge-transfer resistance
R_{mt}	Mass-transport resistance
I_{sc}	Short-circuit current
I-V	Current-voltage
i	Faraday current
i_0	Exchange current
A	Electroactive area
k_0	Electron transfer constant

C_{Ox}^{*}	Initial oxidised agent concentration
C_{Red}^{*}	Initial reduced agent concentration
$C_{Ox}(0,t)$	Time-dependent oxidised agent concentration
$C_{Red}(0,t)$	Time-dependent reduced agent concentration
α_a	Anodic charge-transfer coefficient
α_c	Cathodic charge-transfer coefficient
R	Universal gas constant
η	Overvoltage
E	Electrochemical cell potential
E^0	Standard potential
q	Heat flux
A_c	Cross-sectional area
d	Inter-electrode distance
η_{TEC}	Thermo-electrochemical cell efficiency
ΔC_r	Temperature-dependent concentration ratio difference
α_{eff}	Effective temperature coefficient
η_r	Carnot-related efficiency
EDX	Energy-dispersive X-ray spectroscopy
NMR	Nuclear magnetic resonance
PTFE	Polytetrafluoroethylene
Z'	Impedance real part
Z''	Impedance imaginary part
$R_{I\text{-}V}$	Steady-state resistance
C_{dl}	Electrical double layer capacitance
W_s	Warburg shorted element
$\mathcal{E}_R$	Resistances deviation error
FTO	Fluorine-doped tin oxide
Z_{Ws}	Shorted Warburg impedance
j	Imaginary number
ω	Angular frequency
D	Diffusion coefficient
p	Diffusion exponent
PDADMAC	Poly-diallyl dimethylammonium chloride
PEEK	Polyetheretherketone

Abstract

More than 70% of the global energy consumption is lost as waste heat. This is a so huge amount of energy that only a 10% recovery of this waste heat would exceed the summation of the current energy produced by all the renewable energies. On the other hand, different ubiquitous heat sources such as the sun or even our own bodies are also available and could provide enough amount of energy to power low-consumption sensors and wearable devices. Under this scenario, technologies able to efficiently convert heat into electricity are highly desirable. This thesis deals with two of these technologies: Thermoelectricity and thermo-electrochemical cells (TECs), and it intends to improve their current low efficiencies by applying strategies based on electrochemical phenomena in porous media.

Thermoelectric (TE) materials are solid state highly doped semiconductors. Their relatively low efficiency (η_{TE}), is directly connected to the dimensionless figure of merit ($zT=S^2\sigma T/\kappa$), being S the Seebeck coefficient, σ the electrical conductivity, κ the thermal conductivity and T the absolute temperature. It is worth mentioning that the power factor is defined as $PF=S^2\sigma$.

The main pathway to increase zT is through the reduction of κ, while strategies to increase PF have been minor. Our group published a few years ago a pioneering system to increase the PF. This system was based on a hybrid solid-liquid combination, being the solid a nanostructured and porous antimony-doped tin oxide ($Sb:SnO_2$, ATO) which was permeated by different electrolytes (liquids with ions). This system was capable to increase up to 3.4 times the PF. The main enhancements were achieved using a $LiBF_4$ non-electroactive salt and the 1-butyl-3-methylimidazolium iodide (BMI-I) ionic liquid. In this thesis, we pursue to extend this strategy to electrolytes comprising an electroactive (redox) molecule, capable to exchange electrons with the TE solid. We have used chromium (III) acetylacetonate [$Cr(acac)_3$] as redox molecule which was contacted to the previously employed ATO film. A PF improvement of 3.40 times was achieved due to an 83% drop of the film resistance (R) accompanied with a 23% decrease in the absolute value of S. An impedance spectroscopy (IS) analysis unveiled that the main mechanism behind this remarkable result was an electron injection from the liquid to the solid when they were brought into contact.

Thermo-electrochemical cells are mainly focused on the heat-to-electricity conversion at low temperatures (<100 ºC), since they are formed by a redox electrolyte that separates two metallic electrodes (typically Pt). One of the main problems of this system for its commercial viability is the high price of Pt. Different alternatives have been studied in the last few years, mainly carbon-based porous electrodes or the conducting polymer poly(3,4-ethylenedioxythiophene)-poly(styrenesulfonate) (PEDOT:PSS). However, porous oxide materials have been hardly employed, despite being very successful in other fields like solar cells or batteries.

In this thesis, we have studied the performance of nanostructured and porous ATO in a TEC system in contact with the typical aqueous 0.4 M potassium ferro/ferricyanide solution. This system was compared with the common Pt-based TEC. An impedance spectroscopy analysis revealed that the cell with the ATO electrodes exhibited the same excellent kinetics as Pt. On the other hand, no performance improvements were detected when the electrode area in contact with the electrolyte was significantly increased. Finally, the Carnot-related efficiencies estimated for the Sb:SnO_2 cells were in the same order of magnitude as for Pt electrodes.

Apart from the previous study with ATO, we have evaluated in this thesis an alternative TEC configuration to that generally adopted. The new architecture comprises a substrate with the two electrodes at its ends and with the electrolyte added on the top contacting both electrodes, forming a planar configuration. In our study, we explore first the use of the standard Pt electrodes deposited on top of a conductive glass substrate. Then, we replace the Pt by the ATO. The planar configurations are compared with their corresponding typical architectures using the common ferro/ferricyanide electrolyte. It was found that the planar TEC with Sb:SnO_2 reached a temperature coefficient α=1.76 mV/K, higher than the value obtained in the standard configuration with ATO (1.21 mV/K), and also higher than the planar architecture with Pt electrodes, which showed the typical value for the ferro/ferricyanide electrolyte (1.45 mV/K). As a consequence of this significantly higher α value, a 29.7% higher maximum power output than the planar TEC with Pt was observed.

In conclusion, we have demonstrated that the conversion of heat into electricity can be improved by implementing electrochemical strategies in porous materials, either in TEs or TECs. Our results show the possibility to significantly improve the *PF* of TE materials with an electrolyte containing a redox molecule. Also, we have demonstrated that ATO

can be a suitable electrode material to replace Pt electrodes and produce low cost TECs. Moreover, when ATO is employed in a planar configuration, a significantly high temperature coefficient was found, which is a new feature that opens the door to explore in more detail alternative configurations in TECs.

Abstract (Spanish version)

Más del 70% de la energía global consumida se pierde en forma de calor. Es tal cantidad que reutilizando solamente un 10% de dicha energía se excedería la suma de todas las energías renovables utilizadas en la actualidad. Por otro lado, existen diferentes fuentes de calor ampliamente disponibles tales como el solo o incluso nuestro propio cuerpo que podrían otorgar suficiente cantidad de energía para hacer funcionar dispositivos y sensores portátiles de bajo consumo. Ante esta situación, es necesario el desarrollo de diferentes tecnologías que permitan la conversión de calor en electricidad. En este sentido, esta tesis se relaciona con dos de esas tecnologías: La termoelectricidad y las celdas termo-electroquímicas (TECs), y busca la mejora de las bajas eficiencias que actualmente poseen a través de la aplicación de estrategias electroquímicas en medios porosos.

Los materiales termoeléctricos (TEs) de estado sólido son semiconductores altamente dopados. Su relativamente baja eficiencia (η_{TE}), está directamente relacionada con la figura de mérito adimensional ($zT=S^2\sigma T/\kappa$), donde S es el coeficiente de Seebeck, σ la conductividad eléctrica, κ la conductividad térmica y T la temperatura absoluta. Es importante remarcar que el factor de potencia se define como $PF=S^2\sigma$.

La principal forma de incrementar zT es a través de la reducción de κ, mientras que las estrategias para aumentar PF no han sido tan investigadas. En este sentido, nuestro grupo publicó hace algunos años un sistema pionero capaz de incrementar el PF. Este sistema se basó en una combinación híbrida sólido-líquida, siendo el sólido una película de óxido de estaño dopado con antimonio ($Sb:SnO_2$, ATO) nanoestructurado y poroso el cual se impregnó con diferentes electrolitos (líquidos con iones). Este sistema mostró mejoras en el PF de hasta 3.40 veces. Los principales resultados se consiguieron empleando una sal no electroactiva como es el $LiBF_4$ y el líquido iónico yoduro de 1-butil-3-metilimidazolio (BMI-I). En la presente tesis, se ha buscado la extensión de este sistema empleando una molécula electroactiva (rédox), capaz de intercambiar electrones con el sólido TE. Se ha utilizado la molécula rédox acetilacetonato de cromo (III) [$Cr(acac)_3$] la cual se ha puesto en contacto como el mismo material TE nanoestructurado y poroso (ATO). Como resultado, se consiguieron mejoras de hasta 3.40 veces en el PF debido a una disminución del 83% en la resistencia (R) de la película porosa junto con un decrecimiento del 23% en el valor absoluto del S. Un análisis por espectroscopía de impedancia (IS) reveló que

el principal mecanismo responsable de este resultado fue un proceso de inyección electrónica desde el líquido hacia el sólido cuando ambos se pusieron en contacto.

Las celdas termo-electroquímicas están principalmente orientadas a la obtención de electricidad utilizando para ello calor a bajas temperaturas (<100 ºC), dado que están formadas por un electrolito que contiene un par rédox que separa dos electrodos metálicos (normalmente Pt). De hecho, uno de los principales problemas de estos sistemas es el alto precio de mercado del Pt. En este sentido, diversas alternativas han sido desarrolladas en los últimos años, principalmente a través del uso de materiales porosos basados en el carbono y el polímero conductor poli(3,4-etilendioxitiofeno)-poli(estireno sulfonato) (PEDOT:PSS). Sin embargo, los óxidos metálicos porosos apenas se han utilizado en estos dispositivos, a pesar de estar ampliamente empleados en otros campos tales como celdas solares o baterías.

En esta tesis, se ha estudiado el funcionamiento del óxido de estaño dopado con antimonio nanoestructurado y poroso en una TEC en contacto con el electrolito más típicamente empleado en este campo que es una disolución acuosa 0.4 M de ferro/ferricianuro potásico. Este sistema se ha comparado con la TEC que utiliza electrodos de Pt. Un estudio de espectroscopía de impedancia demostró que la TEC con electrodos de ATO poseía tan buenas propiedades cinéticas como la de Pt. Por otro lado, no se encontraron mejoras en el rendimiento de la TEC con ATO a pesar de incrementar notablemente el área electródica en contacto con el electrolito. Finalmente, las eficiencias relativas al ciclo de Carnot estimadas para las TECs con $Sb:SnO_2$ fueron del mismo orden que para el sistema con Pt.

Además del estudio ya mencionado con ATO, en esta tesis se ha evaluado una configuración de TEC alternativa a la generalmente utilizada. Esta nueva arquitectura incluye un substrato con dos electrodos depositados en sus extremos y un electrolito colocado sobre dicho sustrato contactando ambos electrodos, dando lugar a una configuración planar. En este estudio, se han explorado en primer lugar electrodos de Pt depositados sobre un substrato conductor. Tras ello, se ha substituido dicho material por ATO. Las configuraciones planares con ambos materiales se han comparado con la orientación estándar empleada en las TECs utilizando como electrolito una disolución acuosa 0.4 M de ferro/ferricianuro potásico. Se observó un valor inusualmente alto en el coeficiente de temperatura (α) de α=1.76 mV/K en la TEC planar con electrodos de $Sb:SnO_2$, siendo un valor más alto tanto para la TEC en orientación estándar con el mismo

material (1.21 mV/K) como el sistema planar con Pt, el cual mostró el valor más habitual para este electrolito (1.45 mV/K). Como consecuencia de este alto valor de α, la potencia máxima obtenida para la celda planar con ATO encontrada fue un 29.7% mayor que para el sistema en plano con Pt.

En conclusión, se ha demostrado que la conversión de calor en electricidad puede ser mejorada a través de la aplicación de estrategias electroquímicas en materiales porosos, tanto en TEs como en TECs. Nuestros resultados demuestran la posibilidad incrementar el *PF* en materiales TEs de manera significativa utilizando para ello un electrolito que contiene una molécula rédox. Además, también se ha demostrado que el material ATO puede ser empleado como electrodo reemplazando al Pt con la finalidad de producir TECs a menor coste. Finalmente, cuando el ATO se ha empleado en una TEC en configuración planar, se ha encontrado un valor del coeficiente de temperatura significativamente más alto, abriendo la puerta hacia posibles investigaciones de nuevas arquitecturas en el campo de las TECs.

Index

1. Introduction

1.1. Motivation

The rapid growth of the world population is imposing a huge energy demand, and the use of fossil fuels to satisfy this demand linked to the environmental problems related to their combustion, is leading the world to witness one of the most critical climatic situations ever [1,2]. Furthermore, this energy crisis requires the exploitation of the current sustainable sources of energy in order to fulfill the global demand while the efficiency of these processes must be urgently increased [3]. In addition, it is estimated that 72% of the total world energy consumption is currently lost as waste heat (see Fig. 1.1a) [4]. Only a 10% recovery of this waste heat would exceed the summation of the current renewable energies (see Fig. 1.1b) [5,6]. On the other hand, different ubiquitous heat sources such as the sun or even our own bodies could provide enough amount of energy to power low-consumption sensors and wearable devices [7,8].

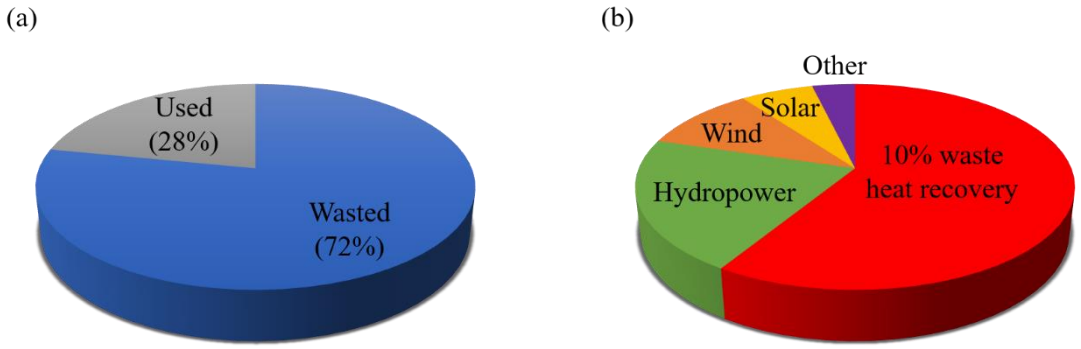

Fig. 1.1. (a) Used and wasted (in form of heat) parts of the total global energy consumption. (b) Representation of the energy produced by current renewable energy sources and 10% of the wasted heat from the global energy consumption. Source: International Energy Agency.

Thermoelectric (TE) devices could significantly contribute to overcome the abovementioned issues, since they are able to convert heat into electricity with no gas emissions (environmentally friendly), free maintenance, and without using moving parts [9,10]. Due to these advantages, they can be employed for different applications such as powering wearable electronic devices [11], energy generation in buildings [12] or recovering industrial waste heat [13]. However, TE devices are not widely spread mainly due to their low efficiency (η_{TE}) and the toxicity and low abundance of many common materials (e.g. Bi_2Te_3, PbTe) [13]. The TE efficiency is directly related to the so-called dimensionless figure of merit ($zT=S^2\sigma T/\kappa$), which is determined by three material properties: the Seebeck coefficient (S), the electrical conductivity (σ) and the thermal conductivity (κ), and also the absolute temperature (T). It is wort noting that the product of the first two parameters is known as the TE power factor ($PF=S^2\sigma$). The most

successful strategy to increase zT has been the κ reduction (specifically, the lattice thermal conductivity κ_L) mainly by nanostructuring [14,15]. In contrast, PF improvements have been minor due to the adverse correlation between S and σ [16].

In 2018, our group reported a novel strategy to improve the PF based on a novel solid-liquid system [17]. In that system, a nanostructured and porous TE solid (antimony-doped tin oxide $Sb:SnO_2$, ATO) was contacted with different liquid electrolytes which were able to significantly increase the PF, showing up to 3.4 times improvements. In that work, the main enhancements were achieved using a $LiBF_4$ non-electroactive salt dissolved in 3-methoxipropionitrile (3-MPN) and the 1-butyl-3-methylimidazolium iodide (BMI-I) ionic liquid. In this thesis (Chapter 3), we pursue to extend this strategy to electrolytes comprising an electro-active (redox) molecule, capable to exchange electrons with the TE solid.

Apart from solid-state TEs, thermo-electrochemical cells (or thermogalvanic cells or thermocells, TECs) have recently gained attention as candidates for the heat-to-electricity conversion at low temperature (<150 ºC). It should be noticed that around 96% of the total waste heat lies in the range from 25-80 ºC [18]. TECs are formed by an electrolyte sandwiched by two electrodes at different temperatures. The electrolyte always includes a redox couple to ensure a constant current output. TECs systems have different advantages when compared with solid-state TEs: (i) they are able to create an open-circuit voltage (V_{oc}) in the order of mV pear each degree of temperature difference [19], (ii) TECs usually use abundant salts (e.g. Fe complexes) in water-based solutions which reduces the cost [20], (iii) they have an inherent low κ as they are liquid-based systems. TECs have a wide range of applications including wearable devices and sensors which use human-body heat [21,22], solar energy harvesting [23] and other applications (e.g. fire alarms) [24]. The main problems of this technology include: (i) the low power output (P_{out}) values they can provide when compared with solid-state TEs due to their high internal resistance, (ii) the encapsulation process needed since they are liquid-based systems and (iii) the very high price of the platinum which is the benchmark electrode material for these systems [25,26]. In this regard, porous materials that exhibit large surface areas have been reported to be an alternative to Pt, since their large area increase can lead to high P_{outs}. These porous materials have been also employed in many other fields like solar cells [27,28], batteries [29,30], supercapacitors [31,32] and even in TECs, being in the majority of cases based on carbon [33]. Because of that, in this thesis

(Chapters 5 to 6), we will explore the use of porous metal oxides in TECs, which has hardly been evaluated despite their possible potential as electrode materials.

1.2. Objectives

The main objective pursued in this thesis is to demonstrate performance improvements in the conversion of heat into electricity in TE systems and TECs induced by electrochemical processes taking place in porous materials.

To achieve this objective, several specific objectives are proposed:

1. To demonstrate *PF* improvements in a nanostructured and porous Sb:SnO_2 TE material in contact with an electrolyte containing a redox molecule (Chapter 3).
2. To fabricate a TEC formed by the same porous metal oxide with suitable performance when compared to Pt (Chapter 5).
3. Explore the performance of a TEC formed by nanostructured and porous Sb:SnO_2 in planar configuration with suitable performance when compared to horizontal configuration (Chapter 6).

1.3. Research strategy

To achieve the mentioned specific objectives, two main research lines were designed: (i) TE solid-liquid system evaluation with the redox electrolyte and, (ii) TECs fabrication employing metal oxide porous electrodes in different orientations (see Fig. 1.2).

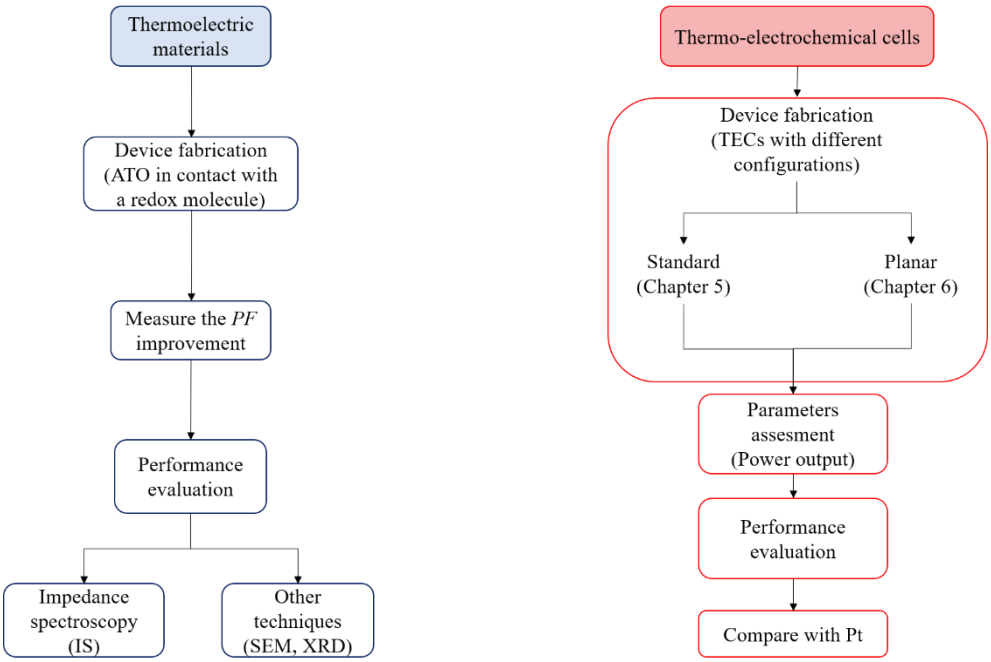

Fig. 1.2. Scheme of the research strategy followed in this thesis.

The first step of both researching lines will be devoted to the device fabrication: (i) porous and nanostructured ATO in contact with the redox molecule (Chapter 3), (ii) TEC with ATO as electrode material in standard configuration (Chapter 5), (iii) TEC with ATO as electrode material in planar orientation (Chapter 6). Then, the *PF* improvements for the solid-liquid system (Chapter 3) will be measured before and after the electrolyte injection, and the possible mechanisms behind the obtained performance will be evaluated by means of impedance spectroscopy (IS) and other techniques (e.g. SEM or XRD). On the other hand, the performance of TECs will be evaluated by measuring the temperature coefficient (α) and P_{outs} under the abovementioned conditions mainly using IS as described in Chapter 4. Finally, all the results obtained in the TECs part of this thesis (Chapters 4 to 6) will be compared with Pt since it is the benchmark material in these systems.

References

[1] Kishore R, Priya S. A Review on Low-Grade Thermal Energy Harvesting: Materials, Methods and Devices. Materials 2018;11:1433–78. https://doi.org/10.3390/ma11081433.

[2] Renewable Energy Agency I. Renewable Power Generation Costs in 2022. 2023.

[3] Coyle ED, Simmons RA. Understanding the Global Energy Crisis. Purdue: Purdue University Press Spring; 2014.

[4] Bianchi G, Panayiotou GP, Aresti L, Kalogirou SA, Florides GA, Tsamos K, et al. Estimating the waste heat recovery in the European Union Industry. Energy Ecol Environ 2019;4:211–21. https://doi.org/10.1007/s40974-019-00132-7.

[5] Forman C, Muritala IK, Pardemann R, Meyer B. Estimating the global waste heat potential. Renewable and Sustainable Energy Reviews 2016;57:1568–79. https://doi.org/10.1016/j.rser.2015.12.192.

[6] Firth A, Zhang B, Yang A. Quantification of global waste heat and its environmental effects. Appl Energy 2019;235:1314–34. https://doi.org/10.1016/j.apenergy.2018.10.102.

[7] Li W, Wang S. Chapter 1 - Principles of low-grade heat harvesting. In: Wang S, editor. Low-Grade Thermal Energy Harvesting, Woodhead Publishing; 2022, p. 1–10. https://doi.org/https://doi.org/10.1016/B978-0-12-823690-1.00011-3.

[8] Huo D, Tian H, Shu G, Wang W. Progress and prospects for low-grade heat recovery electrochemical technologies. Sustainable Energy Technologies and Assessments 2022;49:101802–15. https://doi.org/10.1016/j.seta.2021.101802.

[9] Le W, Yang W, Sheng W, Shuai J. Research Progress of Interfacial Design between Thermoelectric Materials and Electrode Materials. ACS Appl Mater Interfaces 2023;15:12611–21. https://doi.org/10.1021/acsami.2c21035.

[10] d'Angelo M, Galassi C, Lecis N. Thermoelectric Materials and Applications: A Review. Energies (Basel) 2023;16:6409–59. https://doi.org/10.3390/en16176409.

[11] Jia Y, Jiang Q, Sun H, Liu P, Hu D, Pei Y, et al. Wearable Thermoelectric Materials and Devices for Self-Powered Electronic Systems. Advanced Materials 2021;33:2102990–3036. https://doi.org/10.1002/adma.202102990.

[12] Jabri M, Masoumi S, Sajadirad F, West RP, Pakdel A. Thermoelectric energy conversion in buildings. Mater Today Energy 2023;32:101257–79. https://doi.org/https://doi.org/10.1016/j.mtener.2023.101257.

[13] Zheng XF, Liu CX, Yan YY, Wang Q. A review of thermoelectrics research – Recent developments and potentials for sustainable and renewable energy applications. Renewable and Sustainable Energy Reviews 2014;32:486–503. https://doi.org/http://dx.doi.org/10.1016/j.rser.2013.12.053.

[14] Snyder GJ, Toberer ES. Complex thermoelectric materials. Nat Mater 2008;7:105–14. https://doi.org/10.1038/nmat2090.

[15] Mamur H, Ustüner MA, Korucu H, Bhuiyan Amin RM. A review of the performance evaluation of thermoelectric nanostructure materials Bi2-xSbxTe3 (0.20≤X≤1.80). Cleaner Chemical Engineering 2023;6:100101–18.

[16] Dehkordi AM, Zebarjadi M, He J, Tritt TM. Thermoelectric power factor: Enhancement mechanisms and strategies for higher performance thermoelectric materials. Materials Science and Engineering R: Reports 2015;97:1–22. https://doi.org/10.1016/j.mser.2015.08.001.

[17] Márquez-García L, Beltrán-Pitarch B, Powell D, Min G, García-Cañadas J. Large Power Factor Improvement in a Novel Solid–Liquid Thermoelectric Hybrid Device. ACS Appl Energy Mater 2018;1:254–9. https://doi.org/10.1021/acsaem.7b00075.

[18] Luberti M, Gowans R, Finn P, Santori G. An estimate of the ultralow waste heat available in the European Union. Energy 2022;238:121967–84. https://doi.org/10.1016/j.energy.2021.121967.

[19] Qian X, Ma Z, Huang Q, Jiang H, Yang R. Thermodynamics of Ionic Thermoelectrics for Low-Grade Heat Harvesting. ACS Energy Lett 2024:679–706. https://doi.org/10.1021/acsenergylett.3c02448.

[20] Li W, Ma J, Qiu J, Wang S. Thermocells-enabled low-grade heat harvesting: challenge, progress, and prospects. Mater Today Energy 2022;27:101032–10150. https://doi.org/https://doi.org/10.1016/j.mtener.2022.101032.

[21] Yang P, Liu K, Chen Q, Mo X, Zhou Y, Li S, et al. Wearable Thermocells Based on Gel Electrolytes for the Utilization of Body Heat. Angewandte Chemie 2016;128:12229–32. https://doi.org/10.1002/ange.201606314.

[22] Wang Z, Li N, Zhang Z, Cui X, Zhang H. Hydrogel-Based Energy Harvesters and Self-Powered Sensors for Wearable Applications. Nanoenergy Advances 2023;3:315–42. https://doi.org/10.3390/nanoenergyadv3040017.

[23] Wang Y, Zhang Y, Xin X, Yang J, Wang M, Wang R, et al. In situ photocatalytically enhanced thermogalvanic cells for electricity and hydrogen production. Science 2023;381:291–6. https://doi.org/10.1126/science.adg0164.

[24] Yu B, Yang W, Li J, Xie W, Jin H, Liu R, et al. Heat-triggered high-performance thermocells enable a self-powered forest fire alarm. J Mater Chem A Mater 2021;9:26119–26. https://doi.org/10.1039/d1ta06793a.

[25] Dupont MF, MacFarlane DR, Pringle JM. Thermo-electrochemical cells for waste heat harvesting-progress and perspectives. Chemical Communications 2017;53:6288–302. https://doi.org/10.1039/c7cc02160g.

[26] Liu Y, Cui M, Ling W, Cheng L, Lei H, Li W, et al. Thermo-electrochemical cells for heat to electricity conversion: from mechanisms, materials, strategies to applications. Energy Environ Sci 2022;15:3670–87. https://doi.org/10.1039/d2ee01457b.

[27] Rashidi S, Esfahani JA, Rashidi A. A review on the applications of porous materials in solar energy systems. Renewable and Sustainable Energy Reviews 2017;73:1198–210. https://doi.org/10.1016/j.rser.2017.02.028.

[28] Tan WC, Saw LH, Thiam HS, Xuan J, Cai Z, Yew MC. Overview of porous media/metal foam application in fuel cells and solar power systems. Renewable and Sustainable Energy Reviews 2018;96:181–97. https://doi.org/10.1016/j.rser.2018.07.032.

[29] Wang H, Wang X, Li M, Zheng L, Guan D, Huang X, et al. Porous Materials Applied in Nonaqueous Li–O2 Batteries: Status and Perspectives. Advanced Materials 2020;32:2002559–81. https://doi.org/10.1002/adma.202002559.

[30] Chen J, Wang Y, Li S, Chen H, Qiao X, Zhao J, et al. Porous Metal Current Collectors for Alkali Metal Batteries. Advanced Science 2022;10:2205695–723. https://doi.org/10.1002/advs.202205695.

[31] Supiyeva Z, Pan X, Abbas Q. The critical role of nanostructured carbon pores in supercapacitors. Curr Opin Electrochem 2023;39:101249–58. https://doi.org/10.1016/j.coelec.2023.101249.

[32] Pan Z, Yu S, Wang L, Chenyu L, Meng F, Wang N, et al. Recent Advances in Porous Carbon Materials as Electrodes for Supercapacitors. Nanomaterials 2023;13:1744–77. https://doi.org/10.3390/nano13111744.

[33] Duan J, Yu B, Huang L, Hu B, Xu M, Feng G, et al. Liquid-state thermocells: Opportunities and challenges for low-grade heat harvesting. Joule 2021;5:768–79. https://doi.org/https://doi.org/10.1016/j.joule.2021.02.009.

2. Theoretical framework

In this chapter, the main theoretical concepts which are the basics for the correct understanding of this thesis will be covered. First, a brief introduction about solid-state thermoelectrics (TEs) is presented, including the main TE effects and most common TE materials. After that, the initial studies reported about solid TEs combined with electrolytes are shown in detail. Finally, thermo-electrochemical cells (TECs) are introduced, including their fundamentals and the key strategies to increase their performance.

2.1. Solid-state TEs

Here, we cover the main aspects of solid-state TEs. this field including the TE effects and solid TE materials usually employed.

2.1.1. TE effects

There are three main TE effects: (i) The Seebeck coefficient effect which relates the potential gradient that appears as a consequence of a temperature difference, (ii) the Peltier effects that explains the heat absorption/expulsion at different conductor materials junctions and (iii) the Thompson effect which accounts the heat flux generated (or adsorbed) in a non-isothermal TE material. Furthermore, all these abovementioned effects are inter-related by the two Kelvin relationships.

(i) Seebeck effect

In 1822, Thomas Seebeck realised that a compass needle was deflected when it was placed in the vicinity of a closed loop formed from two dissimilar metal conductors if the junctions were maintained at different temperatures [1]. Although he thought that it was a magnetic effect, one year later Hans Christian Ørsted offered the physical explanation to this phenomenon by proving that the magnetic needle was being affected by electrical current [2]. This effect explains the appearance of an open-circuit voltage (V_{oc}) in a non-isothermal electrically conductive material (see Fig. 2.1).

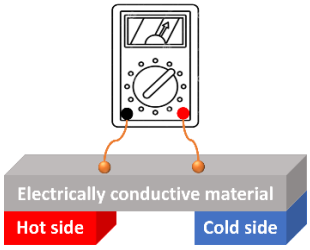

Fig. 2.1. Representation of the Seebeck effect. An open-circuit voltage is generated between the junctions of two dissimilar materials (brown and grey) under a temperature difference.

To explain this phenomenon, one needs to think about the different mobilities of the charge carriers (electrons or holes) at the junctions. The carriers at the hot side will have a larger mobility thanks to the higher thermal energy (high temperature) present there. Due to this fact, they will tend to diffuse toward the cold side pilling up there, and therefore giving rise to a potential difference due to the charge imbalance present in the material (see Fig. 2.2).

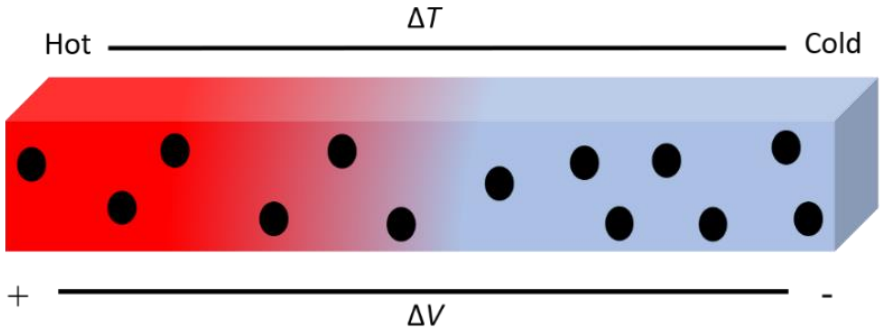

Fig. 2.2. Schematic representation of the reorganization of the electrons under a temperature difference in an n-type conductive material. Electrons are represented by the black points.

The parameter that indicates the voltage provided at open circuit per each degree of temperature difference is called the Seebeck coefficient (S) and its units are V/K, although it is usually given in μV/K. It is defined as,

$$S = \lim_{\Delta T \to 0} \frac{\Delta V}{\Delta T}, \tag{2.1}$$

where ΔV is the potential difference of the cold side with respect to the hot one (TE convention), and $\Delta T = T_C - T_H$ is the temperature difference, being T_C and T_H the temperatures of the cold and hot side, respectively. It is important to remark that if electrons (negative charge) are concentrated at the cold side, the sign of S will be negative (and positive with holes). In the former case, we speak of n-type materials while the latter gives rise to p-type. Typical values for S of TE semiconductors materials (e.g. Bi_2Te_3 alloys) lay around ±200 μV/K, while metals present lower values of ±1-40 μV/K.

One may see that the higher the value of S, the larger the V_{oc} that can be achieved. To have a good TE performance, a high Seebeck coefficient is highly desired.

(ii) Peltier effect

Twelve years later, in 1834, Jean Charles Athanase Peltier discovered the Peltier effect [3]. Regrettably, Peltier interpreted the results of his research work in a wrong way. Only in 1838, Russian academician Emily Lenz proved that the Peltier Effect was an

autonomous physical phenomenon [4], which is based on the absorption/release of heat when a current is flowing between two different conductor materials (see Fig. 2.3). The effect takes place at the materials junctions and it depends on the current direction [5].

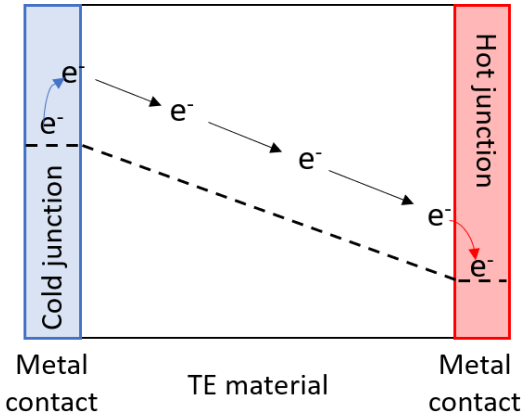

Fig. 2.3. Schematic representation of the Peltier effect with the heat absorption (blue)/release (red) processes that take place at the materials junctions. Dashed line represents the electrochemical potential.

Fig. 2.3 shows a system formed by two metals in contact with an n-type semiconductor. On the one hand, electrons at the left part, need to absorb energy (heat) to jump across the barrier to a higher energy level. Therefore, there is a cooling process at that junction. On the other hand, electrons flowing from the semiconductor to the metal must release energy (heat) to drop to a lower energy level. As a consequence, there is a heating process. To measure the cooling/heating power Q_P , one needs to account the current flow I and the Peltier coefficient Π which are related by,

$$Q_P = \Pi I. \tag{2.2}$$

It is worth noting that, when a TE material (or device) is generating a temperature difference thanks to a current flow, it is working in Peltier mode.

(iii) Thomson effect

More than 20 years later, William Thomson (later, Lord Kelvin) proposed a relationship between the two former effects. Due to this derivation, it was possible for him to stablish the third phenomenon known as Thomson effect [6,7]. He discovered that heat is either absorbed or released when current flows in a non-isothermal material in its whole volume. This heat is proportional to both the electric current and the temperature gradient.

The absorbed/released heat power (Q_T) in the TE material is given by the Thomson coefficient (β), I and ΔT,

$$Q_T = \beta I \Delta T. \tag{2.3}$$

It is worth noting that this is a non-reversible effect which can be neglected in most TE systems working under a low ΔT.

(iv) Kelvin relationships

In 1851, Lord Kelvin (still known as Thomson) stablished a theoretical relationship between the three abovementioned effects: The Seebeck, Peltier and (its own discovered) Thomson effects [8,9].

The first Kelvin relationship shows how *S* and *Π* are linked one to each other.

$$\Pi = ST. \tag{2.4}$$

Thanks to this connection, it can be seen that good TE generators (with high *S*), are also effective coolers (or heaters) (large *Π*).

Furthermore, the second Kelvin relationship was able to relate β with the Seebeck coefficient provided by the material and its temperature variation ($\partial S/\partial T$).

$$\beta = T\frac{\partial S}{\partial T}. \tag{2.5}$$

One may note how is possible to calculate β (and, hence Q_P) and *Π* (and, therefore Q_T) if *S* and $\partial S/\partial T$ are known.

2.1.2. TE materials

Different families of solid-state TE materials exist. However, not all of them offer the same properties (parameters) when employed in different applications. In this regard, highly doped semiconductors (e.g. Bi_2Te_3 alloys) are the benchmark material at room temperature.

To evaluate how good is the performance of a TE material, its electrical and thermal properties must be also analysed. To meet this target, Abram Fiódorovich loffe introduced the concept of figure of merit (*z*) [10]. At present, it is usual to find the temperature-corrected (dimensionless) figure of merit (*zT*) as,

$$zT = \frac{S^2\sigma}{\kappa}T = \frac{PF}{\kappa}T, \tag{2.6}$$

where σ is the electrical conductivity and κ the thermal conductivity. Moreover, the product $S^2\sigma$ is known as the TE power factor (*PF*). Furthermore, this dimensionless *zT* is

also related to the TE efficiency (η_{TE}) and coefficient of performance (*COP*), which are important TE indicators, depending on the mode at which the system is working (Seebeck or Peltier mode, respectively).

As stated by *zT*, an ideal TE material should display a high *PF* (large *S* and σ), since it means a high V_{oc} and *I*, and a low κ, to reach a high ΔT within the material. However, these parameters are not independent at all and they cannot be varied without affecting the others. In fact, all these coefficients are related to the charge carrier concentration (*n*) which makes their optimization the main challenge for the TE community [11]. In this sense, Fig. 2.4 depicts the typical relationships between *n* and all the abovementioned parameters.

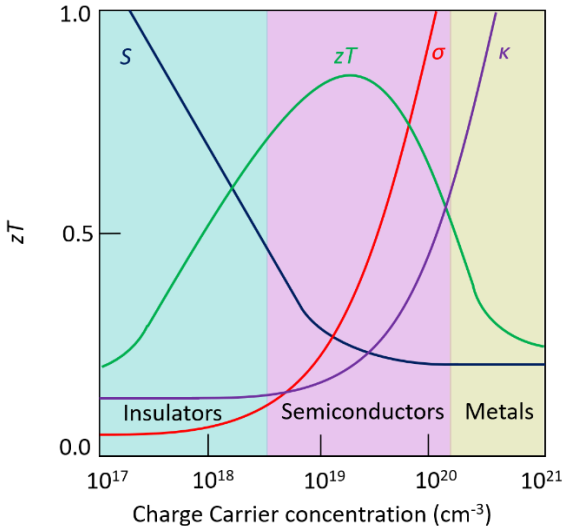

Fig. 2.4. Dependency between all the main thermoelectric parameters: Seebeck coefficient, electrical conductivity, thermal conductivity and dimensionless figure of merit with the charge carrier concentration. The coloured zones indicate the type of material.

It can be seen in Fig. 2.4 how, the higher the carrier concentration, the lower the *S* and eventually *zT*, while thermal and electrical conductivities strongly increase.

Metals are the materials with the highest *n*, which leads to small *S* values. On the other hand, materials with very low carrier concentration (insulators), show prominent Seebeck coefficients but very low σ and κ. Because of these inter-dependent relationships, the highest *zTs* are commonly found in materials with 10^{19}-10^{20} cm^{-3} carrier concentration, which are highly doped semiconductors.

Regrettably, as previously mentioned, not all semiconductors exhibit the same performance at different temperature ranges. For example, the benchmark materials at room temperature are the Bi_2Te_3 alloys, but they do not usually work at high temperatures.

Under those conditions, skutterudites or Half-Heusler compounds present a better TE performance [12]. Fig. 2.5 shows different p- and n-type TE materials and their different *zT* values as a function of temperature [13].

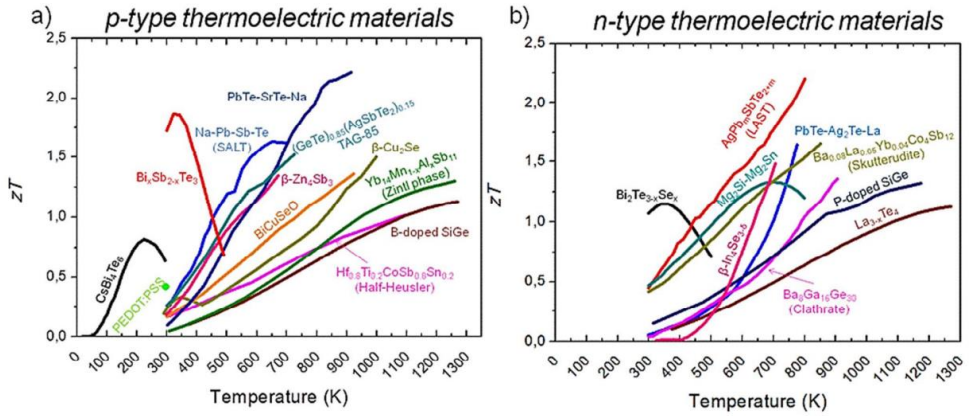

Fig. 2.5. Different families of (a) p-type and (b) n-type TE materials and their *zT* values as a function of temperature. Image reproduced with permission from Ref. [13].

2.1.3. Power output and efficiency of TE materials

If a TE material is subjected to a temperature difference (Seebeck mode operation) a V_{oc} will appear proportional to its *S*. If the system is connected to an external load, an electrical current (*I*) will be produced. The voltage difference across the load (ΔV_{Load}), is given by,

$$\Delta V_{Load} = IR_{Load} = S\Delta T - IR_{\Omega}, \tag{2.7}$$

where R_{Load} is the load resistance and R_{Ω} is the ohmic resistance of the material.

The current produced by the TE material can be given by,

$$I = \frac{S\Delta T}{R_{\Omega} + R_{Load}}. \tag{2.8}$$

Now we can extract the expression for the power output ($P_{out}=\Delta V_{Load}I$) of a TE material by combining Eq. (2.7) and Eq. (2.8),

$$P_{out} = \Delta V_{Load} I = \frac{(S\Delta T)^2 R_{Load}}{(R_{\Omega} + R_{Load})^2}. \tag{2.9}$$

The maximum power output (P_{max}) is found when $R_{\Omega}=R_{Load}$,

$$P_{max} = \frac{(S\Delta T)^2}{4R_{\Omega}}. \tag{2.10}$$

As expected, the larger the *S* (or ΔV) and the lower the R_{Ω} (or higher σ) the best power outputs.

The efficiency for the heat to electricity energy conversion when certain incident heat power (Q_{in}) is present is known as the efficiency of the TE material (η_{TE}),

$$\eta_{TE} = \frac{P_{max}}{Q_{in}}. \tag{2.11}$$

Furthermore, if we combine Eq. (2.11) and Eq. (2.6) the maximum TE efficiency η_{Max} is obtained [14],

$$\eta_{Max} = \left(\frac{T_H - T_C}{T_H}\right)\frac{\sqrt{1+zT_{avg}}-1}{\sqrt{1+zT_{avg}}+\frac{T_C}{T_H}}, \tag{2.12}$$

being $T_{avg}=(T_H+T_C)/2$ the average temperature of the TE material. Moreover, the first term refers to the Carnot efficiency (η_C). From Eq. (2.12), it can be observed how, the larger the zT, the better the material performance. Also, zT increases with the temperature of the system, as shown in Fig. 2.6 [15].

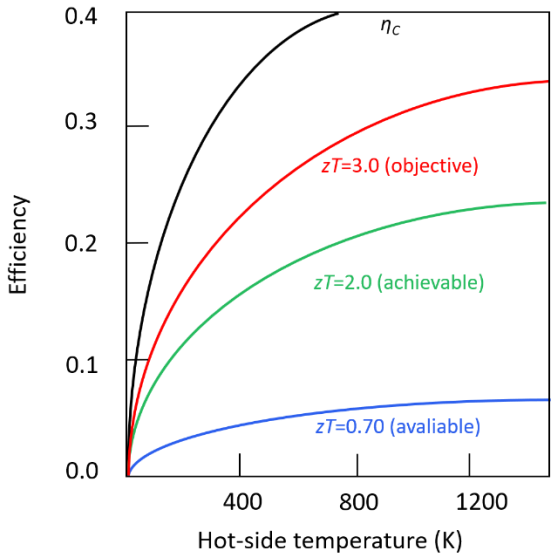

Fig. 2.6. Dependency of the thermoelectric efficiency with the hot side temperature for different zT values. The Carnot efficiency is also shown. Cold side temperature was considered constant at 298 K.

Considering the Carnot imposed limit, zT values close, or even above 3, is the next objective for TE community in order to increase the TE efficiency.

2.2. The solid-electrolyte system

During the last 20 years, the TE community has been mainly focused on reducing the thermal conductivity either by nanostructuring [16] or by introducing phonon scattering [17], since these methods hardly affect the rest of the parameters. Regrettably, κ is achieving its amorphous limit since the phonon mean free path cannot be smaller than the

inter-atomic distance [18]. Due to this fact, improvements in the *PF* have been pursued in the last years [19], mainly either introducing resonant levels [16], modulation doping [20] or making composites [21].

2.2.1. The hybrid system

In this regard, our group reported in the past more than 3 times *PF* improvements in a pioneering solid-liquid hybrid system formed by a nanostructured and porous TE material (Sb:SnO_2, ATO) in contact with different electrolytes (liquids with ions) (see Fig. 2.7) [22].

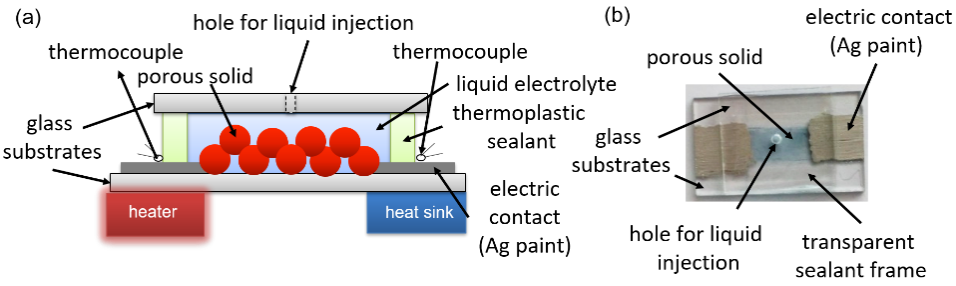

Fig. 2.7. (a) Front-view scheme of the hybrid system and (b) photograph of a device without an electrolyte injected. This figure was reprinted with permission [22].

The system consisted in a nanostructured and porous Sb:SnO_2 film that was permeated by different electrolytes: ionic liquids and inert salts. *PF* improvements were measured before and after the electrolyte injection, achieving more than 3 times enhancements with a 0.1 M solution of $LiBF_4$ dissolved in 3-methoxypropionitrile (3-MPN) due an average drop of 62% in the electrical resistance of the film (*R*) without affecting the Seebeck coefficient. On the other hand, the 1-butyl-3-methylimidazolium (BMI-I) ionic liquid showed improvements higher than 2.50 times since *R* decreased more than 82% while *S* was reduced only by 35%.

This work was performed using inert salts or ionic liquids, which are not expected to exchange electrons with the TE solid. In this thesis it was investigated if *PF* improvements can be achieved employing chromium (III) acetylacetonate [$Cr(acac)_3$], which is a molecule capable to exchange electrons with the TE solid.

2.3. TECs

In this part, the fundamentals (components and parameters) of TECs and the main strategies to increase their performance are reviewed. The main advantage of these devices with respect to solid-state TE materials is that they show higher Seebeck

coefficient values, in the order of mV/K [23,24]. Also, since they are based on liquid or gel electrolytes, their thermal conductivity is low (similar to that of polymers). However, efficiency values for these systems are usually well below 1% due to the high internal resistance of these devices, which is one the main reasons why they are not very extensively studied [25]. It is worth noting that, in this field, the Seebeck coefficient is sometimes employed, but from our point of view is more precise to use the temperature coefficient (α) instead.

2.3.1. Fundamentals

(i) The TEC

Although the thermogalvanic effect was described more than 30 years ago [26–29], TECs have mainly remained hidden until the last years. A TEC is a system formed by two similar electrodes at different temperatures in contact with an electrolyte which contains a redox couple (see Fig. 2.8). The benchmark TEC includes two Pt electrodes permeated by a 0.4 M potassium ferro/ferricyanide aqueous solution (Pt/0.4 M $K_{3/4}Fe(CN)_6$/Pt) [30–33].

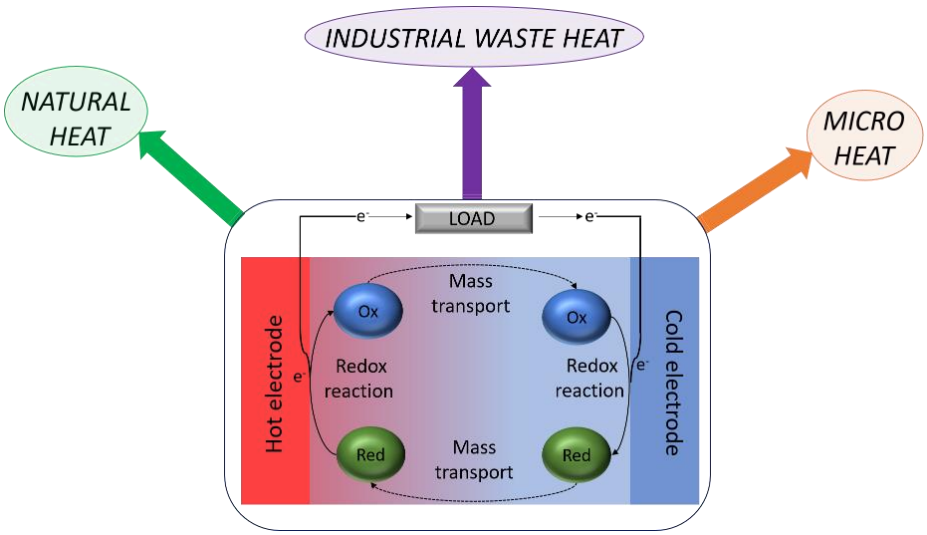

Fig. 2.8. Schematic representation of an ideal thermo-electrochemical cell system where the reduction takes place at the cold side and the oxidation is occurring at the hot part. The main processes and applications are also depicted.

(ii) Temperature (or Seebeck) coefficient

TECs are able to produce electric current when they are subjected to a temperature difference thanks to the temperature dependency of the redox potential (E_{Redox}) [34]. Considering a redox reaction Ox + ne^- ↔ Red ,we can obtain an expression for the temperature coefficient (α) using the relationships between the redox Gibbs free energy

(ΔG_{Redox}), the Faraday constant (F), E_{Redox}, the redox enthalpy (ΔH_{Redox}) and the redox entropy (ΔS_{Redox}),

$$\Delta G_{Redox} = -nFE_{Redox} \tag{2.13}$$

$$\Delta G_{Redox} = \Delta H_{Redox} - T\Delta S_{Redox}. \tag{2.14}$$

If we combine Eq. (2.13) and Eq. (2.14), we obtain the expression,

$$E_{Redox} = -\left(\frac{\Delta H_{Redox}}{nF}\right) + T\left(\frac{\Delta S_{Redox}}{nF}\right). \tag{2.15}$$

To calculate an expression for the temperature coefficient, we need to derive the redox potential with respect to temperature assuming that the redox enthalpy is constant, which is valid for the range of temperatures usually employed in these systems,

$$\alpha = \frac{dE_{Redox}}{dT} = \frac{\Delta S_{Redox}}{nF}. \tag{2.16}$$

Hence, the open-circuit voltage that a TEC is able to create, is directly proportional to the redox entropy difference. In fact, this entropy term is directly related to the partial molar entropy of the redox ions ($\Delta S_{Partial}$), the Eastman entropy ($\Delta S_{Eastman}$) and the entropy of the electrons ($\Delta S_{Electrons}$) through the cables [26,27],

$$\Delta S_{Redox} = \Delta S_{Partial} + \Delta S_{Eastman} + \Delta S_{Electrons}. \tag{2.17}$$

The last two terms can be neglected: The entropy of the cable electrons is negligible when compared with $\Delta S_{Partial}$. Furthermore, $\Delta S_{Eastman}$ considers the solvated ions/solvent interaction when they are travelling through the solvent and can be also discarded according to the literature [23,35]. Hence, Eq. (2.17) can be simplified as,

$$\Delta S_{Redox} = \Delta S_{Partial} = \Delta S_{Red} - \Delta S_{Ox}, \tag{2.18}$$

being ΔS_{Red} and ΔS_{Ox} the partial molar entropies for the reduced and oxidized forms, respectively.

Indeed, $\Delta S_{Partial}$ (and, therefore ΔS_{Redox}) is directly linked to the solvation entropy (ΔS_{Solv}) of the redox ions due to the solvent polarization around their solvation shells. In addition, ΔS_{Solv} can be negative or positive depending on which process (oxidation or reduction) produces a net gain of entropy [30]. For example, if we consider the ferro/ferricyanide redox reaction, the oxidation process will result in a gain of entropy so it will tend to occur at the hot side while the reduction will be at the cold side [30,36]. It produces a total redox entropy difference $\Delta S_{Redox} \approx 135$ kJ/mol which gives rise a

temperature coefficient value of $\alpha \approx 1.40$ mV/K according to Eq. (2.16), which is the value typically found in the literature [23,24,30,32].

Arguably, strategies to improve α have been the most studied so far in this field. Due to this fact, different studies were performed [37] leading to the conclusion that the Born model [38] must be considered since it describes ΔS_{Solv} which is the main contribution to $\Delta S_{Partial}$ as mentioned before. This model implies that ΔS_{Solv} mainly depends on the dielectric constant of the solvent (ε), the ionic radii (r) and the ionic charges of the oxidized (z_{Ox}) and reduced (z_{Red}) forms according to,

$$\Delta S_{Solv} = \frac{e^2 N_A}{2\varepsilon r T}\left(\frac{d ln\varepsilon}{dT}\right)(z_{Ox}^2 - z_{Red}^2), \tag{2.19}$$

where e is the electron charge and N_A the Avogadro's number. Thanks to these dependences, increasing ΔS_{Solv} has been a useful approach to improve α in TECs [32,39].

It is worth noting that, in this thesis, the usual solid-state TEs S convection has been followed, where the hot side is the reference. However, the reader can find in the literature that α for the ferro/ferricyanide system is negative because of the sing convection sometimes followed in TECs.

(iii) Power output of TECs

Several methods can be employed to estimate the power output (P_{out}) in TECs, being chronoamperometry, chronopotentiometry or fixing load resistances the most common techniques [40]. The total (steady state) resistance (R_{dc}) of a TEC has three main contributions [34],

$$R_{dc} = R_s + R_{ct} + R_{mt}, \tag{2.20}$$

where R_s is the series resistance including the electrolyte (mainly) and all the electrical connections (wires and cables), R_{ct} is the charge-transfer resistance due to the redox reactions of the redox couple at the electrode surfaces, and R_{mt} is the mass-transport resistance which accounts for diffusion and convection of the redox species [41].

When the *I-V* curve of a TEC is analyzed a linear response is found as shown in Fig. 2.9 [40].

$$\Delta V_{Load} = I R_{dc}. \tag{2.21}$$

In addition, P_{out} curves of these systems are parabolic with its maximum value (P_{max}) achieved at the half of the curve (see Fig. 2.9) where R_{Load}=R_{dc}.

$$P_{out} = \Delta V_{Load} I = V_{oc} I - I^2 R_{dc} \tag{2.22}$$

$$P_{max} = 0.5(V_{oc} I_{sc}) = \frac{(V_{oc})^2}{4R_{dc}}, \tag{2.23}$$

where I_{sc} is the short-circuit current (value of I when V=0).

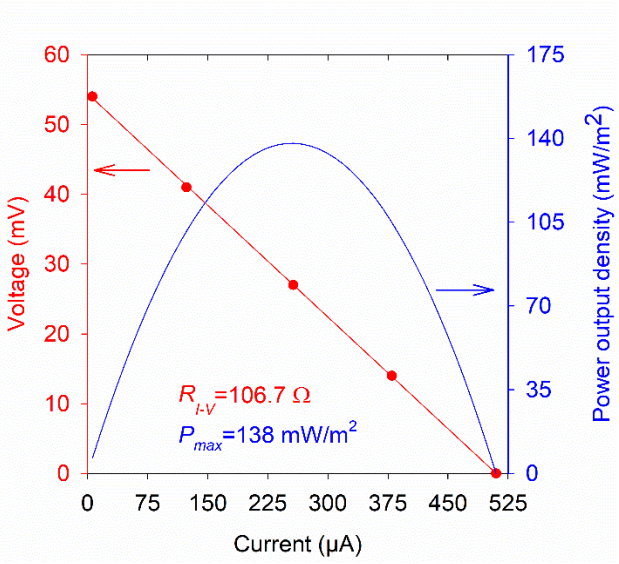

Fig. 2.9. Example of current-voltage and power-current curves of a thermo-electrochemical cell under a temperature difference. This figure was reprinted with permissions [41].

As previously mentioned, R_s is typically related to the resistance of the electrolyte and all the parasitic resistances present in the system. Nevertheless, R_{ct} and R_{mt} do not show such a straightforward determination. Since the core of a TEC is an electrochemical reaction, Butler-Volmer formalism can be employed to assess R_{ct} [42,43]. In this regard, Eq. (2.24) shows redox and mass-transport contributions to the faradaic current in a redox reaction,

$$i = i_0 \left(\frac{C_{ox}(0,t)}{C_{ox}^*} exp[\alpha_a \, nf\eta] - \frac{C_{red}(0,t)}{C_{red}^*} exp[(1-\alpha_c) \, nf\eta] \right), \tag{2.24}$$

where i is the faradaic current produced by the redox reaction, i_0=$nFAk_0C_{ox}^*C_{red}^*$ is the exchange current, A the electroactive area, k_0 the electron transfer constant, C_{Ox}^* and C_{Red}^* are the initial (bulk) oxidised and reduced agent concentrations, $C_{Ox}(0,t)$ and $C_{Red}(0,t)$ are time-dependent concentrations, α_a and α_c are the anodic and cathodic charge-transfer coefficients respectively, f=F/RT being R is the universal gas constant, η=E-E^0 is the overvoltage being E is the electrochemical cell potential and E^0 the standard potential.

Different conclusions can be extracted from Eq. (2.24). On the one hand, by enlarging either the electroactive area or the electrolyte concentration, the generated current will

also increase. One the other hand, R_{mt} is mainly related to the diffusion and convection of the redox ions. These phenomena need also to be improved since ions takes time to travel from electrode to the other. In fact, all of these conclusions led to the development of different methods frequently employed in TECs to increase their P_{out} [32].

(iv) Heat flux

To calculate the efficiency of a TEC the input thermal heat power (Q_{in}) is needed. Arguably, this is the least studied part in TECs systems due to its inherent complexity [27,31,44,45], and generally, Q_{in} is extracted from the conduction of heat through the electrolyte, given by the Fourier's law [31,44], Therefore, the heat flux (q) through the system can be described according to equation,

$$q = \frac{(T_H - T_C)\kappa A_c}{d}, \tag{2.25}$$

where A_c the electrolyte cross-sectional area and d the inter-electrode distance.

For the particular case when Eq. (2.25) is considered to be valid (small d and ΔTs), the TEC efficiency (η_{TEC}) is given by [44,46],

$$\eta_{TEC}(\%) = \frac{P_{max}}{Q_{in}} = \frac{V_{oc} I_{sc}}{4\kappa A_c \frac{\Delta T}{d}} 100. \tag{2.26}$$

However, it was recently demonstrated [44] that Eq. (2.25) fails since it hardly takes into account the rest of the thermal losses: (i) possible cell conduction, (ii) air convection and (iii) radiation. As a consequence, cell engineering is important, and a thermally low conductive material (e.g. PTFE) and suitable cell dimensions should be selected. Regarding the latter, convection in the electrolyte can be managed to increase the total power output of the cell, either if horizontal or cold-above-hot orientations are employed [28,45–48]. In addition, radiation is usually considered a minor process but is has been confirmed to have a considerable effect upon the possible system thermal drops [44,46].

2.3.2. Strategies to increase the performance of TECs

Arguably, strategies related to the temperature coefficient and power output improvements are the most studied in the literature, mainly focusing on solvation entropy alteration [46,49,50] and electrode surface area modification [51–53]. In addition, efforts to reduce the input thermal heat (or thermal conductivity) have also attracted the attention of researchers in the last years [46,54,55].

(i) Open-circuit voltage

Increasing the V_{oc} in a TEC is directly related to an enhancement in the temperature (or Seebeck) coefficient, either due to (a) a solvation entropy alteration [46,50] or (b) an increase in temperature-dependent concentration ratio difference (ΔC_r) within the cell, or sometimes even both effects together [54,56,57].

Both approaches relate to the relationship that α displays in a TEC, which results after combining Eq. (2.16) and the Nernst equation [46],

$$\alpha_{eff} = \alpha - \frac{R}{F}\Delta C_r, \tag{2.27}$$

where α_{eff} is the effective (measured) temperature coefficient. It can be seen how α_{eff} has a second component which depends on the concentration difference of the redox ions apart from the already mentioned solvation entropy part. Eq. (2.27) is a useful tool to predict the possible V_{oc} improvement in a TEC. In this regard, several works have been published in the last years:

(a) Increasing ΔS_{Solv}

The addition of additives to the electrolyte can modify the solvation sphere (and ΔS_{Solv}) producing an increase in the measured temperature coefficient of a TEC. For example, in 2017 Kim et al. added methanol to the ferro/ferricyanide solution to modify the ferrocyanide ΔS_{Solv} giving α=2.9 mV/K, which is more than 2 times the usual value [49]. A major step was achieved by Prof. Jun Zhou's group one year later, obtaining a temperature coefficient of α=4.2 mV/K after inducing a synergistic ΔS_{Solv} modification of ferricyanide (with urea) and ferrocyanide (with guanidium chloride) [50]. Later on, in 2020, the same group achieved an unprecedented Carnot-related efficiency (η_r) value of η_r=11.1% using the guanidium-modified ferro/ferricyanide electrolyte producing a thermo-crystallization effect which boosted α and reduced κ synergistically [46].

(b) Increasing ΔC_r

As shown in Eq. (2.27), increasing the internal concentration difference of the cell can result in a temperature coefficient improvement. Although less investigated than the former, this route has been significantly used by many groups in the last years. For instance, Wang et al. obtained a huge value of α_{eff}=8 mV/K for the ferro/ferricyanide system due to an increase in ΔC_r by inducing a photocatalytic effect with the oxygen evolution reaction [56]. In addition, Yu et al. increased the concentration difference by

using a membrane to selective separate the ions obtaining a fire-sensing TEG which was tested as a fire alarm [57]. Another example was given by Prof. Yamada's group which enlarged this parameter by inducing host-guest chemistry into the iodide/triodide TEC system [35].

(ii) Power output

In general, P_{out} values is the main drawback when TECs are compared with solid-state TE materials which usually are several orders of magnitude lower than solid-state TE materials [32,58]. To overcome this disadvantage, different studies have been focused on optimizing (a) the electrodes or (b) the electrolytes, respectively.

(a) Electrode optimization

Improving electrode kinetics will result in an enhancement of R_{ct}, and therefore, in the current output that a TEC can deliver [32,59]. Platinum has been considered one of the best materials in terms of kinetics. However, the high cost of this material makes it prohibited in order to achieve a larger implementation [60]. In this sense, carbon-based materials have gained attention during the last fifteen years as a valid alternative to Pt due to their larger surface area and good kinetics [61]. In fact, multi-walled [51] and single-walled [62] carbon nanotubes offered η_r values of 1.4% and 2.6%, respectively. A major step was carried out by using Pt-decorated aerogel carbon nanotubes obtaining a value of ηr=3.95% [53]. Recently, the record efficiency value was beaten thanks to the combination of the guanidium-boosted electrolyte [46] with nitrogen-doped carbon nanowires on carbon cloth fibres achieving a value of η_r=13.02% [63]. In addition, this value was again surpassed after using the same electrolyte with asymmetric cobalt oxide electrodes which offered a higher η_r=14.8% [64]. These works open the possibly of the combination between boosted electrolytes and optimized electrodes which can turn into much better performances.

(b) Electrolyte optimization

Although $Fe(CN_6)^{3-/4-}$ is the benchmark redox couple, it has a certain number of limitations (e.g. HCN production under acidic conditions) that make necessary the development of new electrolytes [30,65]. This has been intensively investigated during the last years mainly due to the appearance of new iron-based [36,65], iodide [35,66] and ionic liquid [67,68] electrolytes. In addition, increasing the electrolyte concentration has been reported to offer larger power outputs even after increasing the viscosity (and, hence

R_s) of the electrolyte [69,70]. Due to the abovementioned reasons, electrolyte optimization is also an important strategy for the TEC performance enhancement.

(iii) Thermal conductivity

Unlike α and P_{out}, efforts related to the suppression of κ have been minor in the literature, mainly due to its inherent difficulty to be correctly measured in a TEC [44]. However, this parameter cannot be ignored since keeping the temperature difference within the system is essential for the electric current generation [23]. Because of that, either (a) introducing thermal separators or (b) using gel-based electrolytes have been identified to be valid strategies for the thermal conductivity reduction.

(a) Introducing thermal separators

Under very large ΔT thermal convection cannot be discarded. In fact, it can dominate the κ value [45]. In this regard, it has been reported that thermal separators in electrolytes can effectively increase the TEC performance by suppressing the thermal convection within the electrolyte [71,72]. Thanks to these works, it was discovered that, under appropriate dimensions (e.g. thickness and porosity), large increases in ΔT values can be achieved, reducing the thermal input needed into the cell.

(b) Gel-based electrolytes

Gel electrolytes can be an effective way to reduce the thermal conductivity since thermal convection is sometimes negligible in those system [54,73,74]. However, the movement of ions is also decreased which can turn into a power output reduction under certain conditions. This fact is one of the main reasons why gel-based electrolytes are not widely spread in the literature. On the other hand, gel electrolytes partially solve possible leakage problems usually found in liquids, which can be beneficial for wearable devices [73].

References

[1] Kazuaki Yazawa, Je-Hyeong Bahk, Ali Shakouri - Thermoelectric Energy Conversion Devices and Systems_ 7 (Wspc Series In Advanced Integration And Packaging)-World Scientific Publishing Co (2021) n.d.

[2] ASTM Committee E20 on Temperature Measurement. Manual on the use of thermocouples in temperature measurement. ASTM; 1993.

[3] Gurevich YuG, Velazquez-Perez JE. Peltier Effect in Semiconductors. Wiley Encyclopedia of Electrical and Electronics Engineering, Wiley; 2014, p. 1–21. https://doi.org/10.1002/047134608x.w8206.

[4] Ioffe AF, Stil'bans LS, Iordanishvili EK, Stavitskaya TS, Goldsmid HJ, Set On Vari-Typer BM. Semiconductor Thermoelements and Thermoelectric Cooling. vol. 110. 1956.

[5] Zheng XF, Liu CX, Yan YY, Wang Q. A review of thermoelectrics research - Recent developments and potentials for sustainable and renewable energy applications. Renewable and Sustainable Energy Reviews 2014;32:486–503. https://doi.org/10.1016/j.rser.2013.12.053.

[6] Thomson W. 4. On a Mechanical Theory of Thermo-Electric Currents. Proceedings of the Royal Society of Edinburgh 1857;3:91–8. https://doi.org/10.1017/s0370164600027310.

[7] Snyder GJ, Toberer ES, Khanna R, Seifert W. Improved thermoelectric cooling based on the Thomson effect. Phys Rev B Condens Matter Mater Phys 2012;86:045202–10. https://doi.org/10.1103/PhysRevB.86.045202.

[8] Apertet Y, Goupil C. On the fundamental aspect of the first Kelvin's relation in thermoelectricity. International Journal of Thermal Sciences 2016;104:225–7. https://doi.org/10.1016/j.ijthermalsci.2016.01.009.

[9] Hua YC, Xue TW, Guo ZY. Reversible reciprocal relation of thermoelectricity. Phys Rev E 2021;103:012107–15. https://doi.org/10.1103/PhysRevE.103.012107.

[10] Zabrocki K, Seifert W, Müller E. Effective power factor and thermoelectric figure of merit. AIP Conf Proc, vol. 1449, 2012, p. 427–30. https://doi.org/10.1063/1.4731587.

[11] Snyder GJ, Toberer ES. Complex thermoelectric materials. Nat Mater 2008;7:105–14. https://doi.org/10.1038/nmat2090.

[12] Beretta D, Neophytou N, Hodges JM, Kanatzidis MG, Narducci D, Martin-Gonzalez M, et al. Thermoelectrics: From history, a window to the future. Materials Science and Engineering R: Reports 2019;138:210–55. https://doi.org/10.1016/j.mser.2018.09.001.

[13] Rull-Bravo M, Moure A, Fernández JF, Martín-González M. Skutterudites as thermoelectric materials: Revisited. RSC Adv 2015;5:41653–67. https://doi.org/10.1039/c5ra03942h.

[14] Kim HS, Liu W, Chen G, Chu CW, Ren Z. Relationship between thermoelectric figure of merit and energy conversion efficiency. Proc Natl Acad Sci U S A 2015;112:8205–10. https://doi.org/10.1073/pnas.1510231112.

[15] Wolf M, Hinterding R, Feldhoff A. High Power Factor vs. High zT—A Review of Thermoelectric Materials for High-Temperature Application. Entropy 2019;21:1058–90. https://doi.org/10.3390/e21111058.

[16] Jang J, Koo B-K, Kim M-S, Lee JE. Microstructure change and thermal conductivity reduction in p-type Bi–Sb–Te thermoelectric materials using a metal fatty acid as process control agent. Appl Surf Sci 2023;611:155643–9. https://doi.org/https://doi.org/10.1016/j.apsusc.2022.155643.

[17] Zhou CD, Liang B, Huang WJ, Noudem JG, Tan XJ, Jiang J. Phonon engineering significantly reducing thermal conductivity of thermoelectric materials: a review. Rare Metals 2023;42:2825–39. https://doi.org/10.1007/s12598-023-02302-3.

[18] Heremans JP, Jovovic V, Toberer ES, Saramat A, Kurosaki K, Charoenphakdee A, et al. Enhancement of Thermoelectric Efficiency in PbTe by Distortion of the Electronic Density of States. Science 2008;321:554–7. https://doi.org/10.1126/science.1159725.

[19] Dehkordi AM, Zebarjadi M, He J, Tritt TM. Thermoelectric power factor: Enhancement mechanisms and strategies for higher performance thermoelectric materials. Materials Science and Engineering R: Reports 2015;97:1–22. https://doi.org/10.1016/j.mser.2015.08.001.

[20] Zebarjadi M, Joshi G, Zhu G, Yu B, Minnich A, Lan Y, et al. Power factor enhancement by modulation doping in bulk nanocomposites. Nano Lett 2011;11:2225–30. https://doi.org/10.1021/nl201206d.

[21] Serrano-Claumarchirant JF, Hamawandi B, Ergül AB, Cantarero A, Gómez CM, Priyadarshi P, et al. Thermoelectric Inks and Power Factor Tunability in Hybrid Films through All Solution Process. ACS Appl Mater Interfaces 2022;14:19295–303. https://doi.org/10.1021/acsami.1c24392.

[22] Márquez-García L, Beltrán-Pitarch B, Powell D, Min G, García-Cañadas J. Large Power Factor Improvement in a Novel Solid–Liquid Thermoelectric Hybrid Device. ACS Appl Energy Mater 2018;1:254–9. https://doi.org/10.1021/acsaem.7b00075.

[23] Dupont MF, MacFarlane DR, Pringle JM. Thermo-electrochemical cells for waste heat harvesting-progress and perspectives. Chemical Communications 2017;53:6288–302. https://doi.org/10.1039/c7cc02160g.

[24] Li W, Ma J, Qiu J, Wang S. Thermocells-enabled low-grade heat harvesting: challenge, progress, and prospects. Mater Today Energy 2022;27:101032–10150. https://doi.org/https://doi.org/10.1016/j.mtener.2022.101032.

[25] Duan J, Yu B, Huang L, Hu B, Xu M, Feng G, et al. Liquid-state thermocells: Opportunities and challenges for low-grade heat harvesting. Joule 2021;5:768–79. https://doi.org/https://doi.org/10.1016/j.joule.2021.02.009.

[26] Quickenden TI, Vernon CF. Thermogalvanic Conversion of Heat to Electricity. Solar Energy 1986;36:63–72. https://doi.org/10.1016/0038-092X(86)90061-7.

[27] Quickenden TI, Mua Y. The Power Conversion Efficiencies of a Thermogalvanic Cell Operated in Three Different Orientations. J Electrochem Soc 1995;142:3652–9. https://doi.org/10.1149/1.2048394.

[28] Ikeshoji T, Kimura S, Nelly Bravo de Nahui F, Yoneya M. Computer analysis of natural convection in thin-layer thermocells with a soluble redox couple Part 1. Method and the unsteady problem. J Electroanal Chem 1991;307:29–45. https://doi.org/10.1016/0022-0728(91)85537-Y.

[29] Sumino M, Harada K, Ikeda M, Tanaka S, Miyazaki K, Adachi C. Thermoelectric properties of n-type C60 thin films and their application in organic thermovoltaic devices. Appl Phys Lett 2011;99:93308–12. https://doi.org/doi:http://dx.doi.org/10.1063/1.3631633.

[30] Buckingham MA, Hammoud S, Li H, Beale CJ, Sengel JT, Aldous L. A fundamental study of the thermoelectrochemistry of ferricyanide/ferrocyanide: Cation, concentration, ratio, and heterogeneous and homogeneous electrocatalysis effects in thermogalvanic cells. Sustain Energy Fuels 2020;4:3388–99. https://doi.org/10.1039/d0se00440e.

[31] Salazar PF, Kumar S, Cola BA. Design and optimization of thermo-electrochemical cells. J Appl Electrochem 2014;44:325–36. https://doi.org/10.1007/s10800-013-0638-y.

[32] Duan J, Yu B, Huang L, Hu B, Xu M, Feng G, et al. Liquid-state thermocells: Opportunities and challenges for low-grade heat harvesting. Joule 2021;5:768–79. https://doi.org/10.1016/j.joule.2021.02.009.

[33] Qian X, Ma Z, Huang Q, Jiang H, Yang R. Thermodynamics of Ionic Thermoelectrics for Low-Grade Heat Harvesting. ACS Energy Lett 2024:679–706. https://doi.org/10.1021/acsenergylett.3c02448.

[34] Massetti M, Jiao F, Ferguson AJ, Zhao D, Wijeratne K, Würger A, et al. Unconventional Thermoelectric Materials for Energy Harvesting and Sensing Applications. Chem Rev 2021;121:12465–547. https://doi.org/10.1021/acs.chemrev.1c00218.

[35] Zhou H, Inoue H, Ujita M, Yamada T. Advancement of Electrochemical Thermoelectric Conversion with Molecular Technology. Angewandte Chemie International Edition 2023;62:1–18. https://doi.org/https://doi.org/10.1002/anie.202213449.

[36] Buckingham MA, Marken F, Aldous L. The thermoelectrochemistry of the aqueous iron(ii)/iron(iii) redox couple: Significance of the anion and pH in thermogalvanic thermal-to-electrical energy conversion. Sustain Energy Fuels 2018;2:2717–26. https://doi.org/10.1039/c8se00416a.

[37] Hupp JT, Weaver MJ. Solvent, Ligand, and Ionic Charge Effects on Reaction Entropies for Simple Transition-Metal Redox Couples. vol. 23. 1984.

[38] Born M. Volumen und Hydratationswärme der Ionen. Zeitschrift Für Physik 1920;1:45–8. https://doi.org/10.1007/BF01881023.

[39] Huo D, Tian H, Shu G, Wang W. Progress and prospects for low-grade heat recovery electrochemical technologies. Sustainable Energy Technologies and Assessments 2022;49:101802–15. https://doi.org/10.1016/j.seta.2021.101802.

[40] Buckingham MA, Aldous L. Thermogalvanic cells: A side-by-side comparison of measurement methods. Journal of Electroanalytical Chemistry 2020;872:114280–90. https://doi.org/10.1016/j.jelechem.2020.114280.

[41] Castro-Ruiz S, García-Cañadas J. Impedance Spectroscopy Analysis of a Thermo-Electrochemical Cell Under Operating Conditions. 2022 International Workshop on Impedance Spectroscopy (IWIS), 2022, p. 25–7. https://doi.org/10.1109/IWIS57888.2022.9975126.

[42] Butler JAV. Studies in heterogeneous equilibria. Part III. A kinetic theory of reversible oxidation potentials at inert electrodes. Transactions of the Faraday Society 1924;19:734–9. https://doi.org/10.1039/tf9241900734.

[43] Bard AJ, Faulkner LR. Electrochemical methods : fundamentals and applications. 2nd ed. Wiley; 2001.

[44] Trosheva MA, Buckingham MA, Aldous L. Direct measurement of the genuine efficiency of thermogalvanic heat-to-electricity conversion in thermocells. Chem Sci 2022;13:4984–98. https://doi.org/10.1039/d1sc06340e.

[45] Gunawan A, Li H, Lin CH, Buttry DA, Mujica V, Taylor RA, et al. The amplifying effect of natural convection on power generation of thermogalvanic cells. Int J Heat Mass Transf 2014;78:423–34. https://doi.org/10.1016/j.ijheatmasstransfer.2014.07.007.

[46] Yu B, Duan J, Cong H, Xie W, Liu R, Zhuang X, et al. Thermosensitive crystallization-boosted liquid thermocells for low-grade heat harvesting. Science 2020;370:342–6. https://doi.org/10.1126/science.abd6749.

[47] Ikeshoji T, Nelly Bravo de Nahui F, Kimura S, Yoneya M. Computer analysis on natural convection in thin-layer thermocells with a soluble redox couple Part 2. E-I relation, electric power, heat flux and electrochemical heat pump. J Electroanal Chem 1991;312:43–56. https://doi.org/10.1016/0022-0728(91)85143-D.

[48] Yu X, Shen Z, Qian G, Lu G, Liu H, Huang R, et al. Synergistic improvement of Seebeck coefficient and power density of an aqueous thermocell using natural convection for low-grade heat utilization. Appl Therm Eng 2023;231:121004–16. https://doi.org/10.1016/j.applthermaleng.2023.121004.

[49] Kim T, Lee JS, Lee G, Yoon H, Yoon J, Kang TJ, et al. High thermopower of ferri/ferrocyanide redox couple in organic-water solutions. Nano Energy 2017;31:160–7. https://doi.org/10.1016/j.nanoen.2016.11.014.

[50] Duan J, Feng G, Yu B, Li J, Chen M, Yang P, et al. Aqueous thermogalvanic cells with a high Seebeck coefficient for low-grade heat harvest. Nat Commun 2018;9:5146–54. https://doi.org/10.1038/s41467-018-07625-9.

[51] Hu R, Cola BA, Haram N, Barisci JN, Lee S, Stoughton S, et al. Harvesting waste thermal energy using a carbon-nanotube-based thermo-electrochemical cell. Nano Lett 2010;10:838–46. https://doi.org/10.1021/nl903267n.

[52] Holubowitch NE, Landon J, Lippert CA, Craddock JD, Weisenberger MC, Liu K. Spray-Coated Multiwalled Carbon Nanotube Composite Electrodes for Thermal Energy Scavenging Electrochemical Cells. ACS Appl Mater Interfaces 2016;8:22159–67. https://doi.org/10.1021/acsami.6b05083.

[53] Im H, Kim T, Song H, Choi J, Park JS, Ovalle-Robles R, et al. High-efficiency electrochemical thermal energy harvester using carbon nanotube aerogel sheet electrodes. Nat Commun 2016;7:10600–9. https://doi.org/10.1038/ncomms10600 (2016).

[54] Han C-G, Qian X, Li Q, Deng B, Zhu Y, Han Z, et al. Giant thermopower of ionic gelatin near room temperature. Science 2020;368:1091–8. https://doi.org/10.1126/science.aaz5045.

[55] Li Y, Li Q, Zhang X, Zhang J, Wang S, Lai L, et al. Realizing record-high output power in flexible gelatin/GTA-KCl-FeCN4−/3− ionic thermoelectric cells enabled by extending the working temperature range. Energy Environ Sci 2022;15:5379–90. https://doi.org/10.1039/d2ee02792e.

[56] Wang Y, Zhang Y, Xin X, Yang J, Wang M, Wang R, et al. In situ photocatalytically enhanced thermogalvanic cells for electricity and hydrogen production. Science 2023;381:291–6. https://doi.org/10.1126/science.adg0164.

[57] Yu B, Yang W, Li J, Xie W, Jin H, Liu R, et al. Heat-triggered high-performance thermocells enable a self-powered forest fire alarm. J Mater Chem A Mater 2021;9:26119–26. https://doi.org/10.1039/d1ta06793a.

[58] d'Angelo M, Galassi C, Lecis N. Thermoelectric Materials and Applications: A Review. Energies (Basel) 2023;16:6409–59. https://doi.org/10.3390/en16176409.

[59] Li W, Ma J, Qiu J, Wang S. Thermocells-enabled low-grade heat harvesting: challenge, progress, and prospects. Mater Today Energy 2022;27. https://doi.org/10.1016/j.mtener.2022.101032.

[60] Watson BJ, Eggert RG. Understanding relative metal prices and availability: Combining physical and economic perspectives. J Ind Ecol 2021;25:890–9. https://doi.org/10.1111/jiec.13087.

[61] Volfkovich YM, Sosenkin VE, Rychagov AY, Melezhik A V, Tkachev AG, Kabachkov EN, et al. Carbon material with high specific surface area and high pseudocapacitance: Possible application in supercapacitors. Microporous and Mesoporous Materials 2021;319:111063–70. https://doi.org/https://doi.org/10.1016/j.micromeso.2021.111063.

[62] Romano MS, Li N, Antiohos D, Razal JM, Nattestad A, Beirne S, et al. Carbon nanotube-reduced graphene oxide composites for thermal energy harvesting applications. Advanced Materials 2013;25:6602–6. https://doi.org/10.1002/adma.201303295.

[63] Zhuang X, Jin H, Yu B, Wang H, Luo Y, Liu K, et al. Rational design of carbon electrodes of thermoelectrochemical cells for efficient low-grade heat harvesting. J Mater Chem A 2022;10:17544–51. https://doi.org/10.1039/D2TA05327F.

[64] Zhuang X, Jin H, Dai S, Li X, Guo W, Wang Y, et al. Self-Assembled Asymmetric Electrodes for High-Efficiency Thermogalvanic Cells. Adv Energy Mater 2023;13:2302011–9. https://doi.org/https://doi.org/10.1002/aenm.202302011.

[65] Buckingham MA, Laws K, Cross E, Surman AJ, Aldous L. Developing iron-based anionic redox couples for thermogalvanic cells: Towards the replacement of the ferricyanide/ferrocyanide redox couple. Green Chemistry 2021;23:8901–15. https://doi.org/10.1039/d1gc02989d.

[66] Liang Y, Yamada T, Zhou H, Kimizuka N. Hexakis(2,3,6-tri-: O -methyl)-α-cyclodextrin-I5- complex in aqueous I-/I3- thermocells and enhancement in the Seebeck coefficient. Chem Sci 2019;10:773–80. https://doi.org/10.1039/c8sc03821j.

[67] Salazar PF, Chan KJ, Stephens ST, Cola BA. Enhanced Electrical Conductivity of Imidazolium-Based Ionic Liquids Mixed with Carbon Nanotubes: A Spectroscopic

Study. J Electrochem Soc 2014;161:H481–6. https://doi.org/10.1149/2.0401409jes.

[68] Salazar PF, Stephens ST, Kazim AH, Pringle JM, Cola BA. Enhanced thermo-electrochemical power using carbon nanotube additives in ionic liquid redox electrolytes. J Mater Chem A Mater 2014;2:20676–82. https://doi.org/10.1039/c4ta04749d.

[69] Buckingham MA, Laws K, Li H, Kuang Y, Aldous L. Thermogalvanic cells demonstrate inherent physiochemical limitations in redox-active electrolytes at water-in-salt concentrations. Cell Rep Phys Sci 2021;2:100510–26. https://doi.org/10.1016/j.xcrp.2021.100510.

[70] Laux E, Uhl S, Journot T, Brossard J, Jeandupeux L, Keppner H. Aspects of Protonic Ionic Liquid as Electrolyte in Thermoelectric Generators. J Electron Mater 2016;45:3383–9. https://doi.org/10.1007/s11664-016-4526-1.

[71] Zhang L, Kim T, Li N, Kang TJ, Chen J, Pringle JM, et al. High Power Density Electrochemical Thermocells for Inexpensively Harvesting Low-Grade Thermal Energy. Advanced Materials 2017;29:1605652–9. https://doi.org/10.1002/adma.201605652.

[72] Hasan SW, Said SM, Sabri MFM, Bakar ASA, Hashim NA, Hasnan MMIM, et al. High Thermal Gradient in Thermo-electrochemical Cells by Insertion of a Poly(Vinylidene Fluoride) Membrane. Sci Rep 2016;6:29328–39. https://doi.org/10.1038/srep29328.

[73] Wang Z, Li N, Zhang Z, Cui X, Zhang H. Hydrogel-Based Energy Harvesters and Self-Powered Sensors for Wearable Applications. Nanoenergy Advances 2023;3:315–42. https://doi.org/10.3390/nanoenergyadv3040017.

[74] Li X, Li J, Wang T, Khan SA, Yuan Z, Yin Y, et al. Self-Powered Respiratory Monitoring Strategy Based on Adaptive Dual-Network Thermogalvanic Hydrogels. ACS Appl Mater Interfaces 2022;14:48743–51. https://doi.org/10.1021/acsami.2c14239.

3. Power Factor Improvement in a Solid-Liquid Thermoelectric System Formed by Sb:SnO_2 in Contact with a Chromium Complex Solution

Power Factor Improvement in a Solid-Liquid Thermoelectric System Formed by Sb:SnO_2 in Contact with a Chromium Complex Solution

S. Castro-Ruiz[1], L. Márquez-García[1], M. Solis-de la Fuente[1], B. Beltrán-Pitarch[1], A. Mota-Babiloni[1], F. Vidan[1], P. Íñigo-Rabinal[2], G. Guisado-Barrios[2], J. García-Cañadas[1]*

[1]Department of Industrial Systems Engineering and Design, Universitat Jaume I, Av. Vicent Sos Baynat s/n, 12006 Castelló de la Plana, Spain.

[2]CSIC-Universidad de Zaragoza, Institute for Chemical Synthesis and Homogeneous Catalysis (ISQCH), C/Pedro Cerbuna 12, 50009 Zaragoza, Spain.

* e-mail: garciaj@uji.es

Sustainable Energy & Fuels 7, 4254-4259 (2023).

DOI: 10.1039/d3se00622k.

Graphical abstract

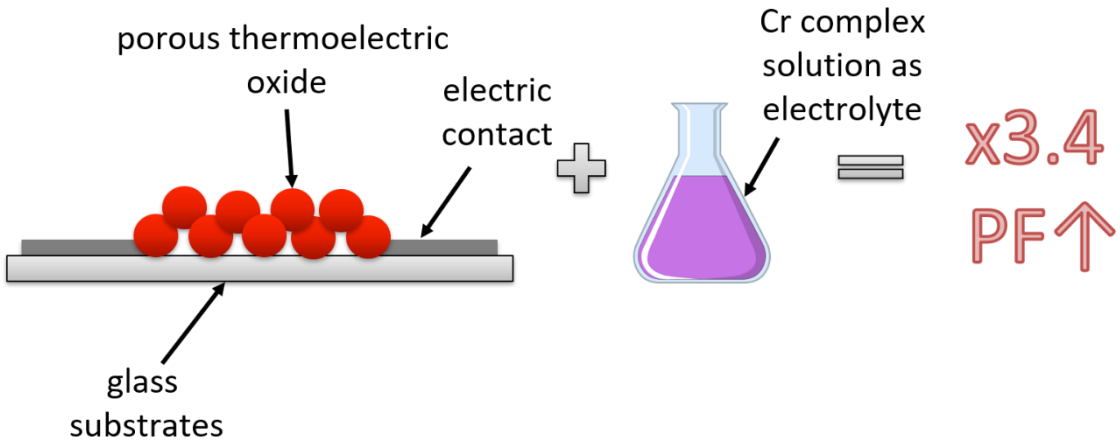

Fig. 3.1. Graphical abstract of the work: Power Factor Improvement in a Solid-Liquid Thermoelectric System Formed by Sb:SnO_2 in Contact with a Chromium Complex Solution.

Abstract

Thermoelectric (TE) materials can convert heat into electricity. Good TE materials should have high power factors (*PFs*) and low thermal conductivities. The $PF=S^2\sigma$ is governed by the Seebeck coefficient S and the electrical conductivity σ. Most recent improvements in TE materials performance have been achieved by the reduction of the thermal conductivity, and strategies to improve the *PF* have been minor. Recently, an innovative concept to significantly increase the *PF*, based on the combination of a porous TE solid with an electrolyte, has been reported. Here, we make use of this new approach but using an electroactive salt (redox molecule) solution as electrolyte, rather than the non-electroactive electrolytes and ionic liquids previously employed. A system formed by a nanostructured and porous Sb:SnO_2 film in contact with Cr (III) acetylacetonate dissolved in 3-methoxypropionitrile was prepared. Using this electrolyte, an average *PF* enhancement of 3.4 times was achieved, due to an average decrease of 23.2% and 82.8% in the absolute value of the Seebeck coefficient and the electrical resistivity of the solid, respectively. An impedance spectroscopy analysis, after checking that no changes take place in the Sb:SnO_2 film due to the presence of electrolytes by scanning electron microscopy and energy-dispersive X-ray spectroscopy, revealed that the improvements come from the donation of electrons from the electrolyte to the solid, which increases its electrical conductivity and the usual drop in the Seebeck coefficient. The remarkable *PF* improvement obtained is among the highest reported and opens a new way of significantly enhance this parameter.

3.1. Introduction

More than 60% of the global power is lost as waste heat. In addition to the waste heat, ubiquitous heat sources such as the sun or even our own bodies are widely available. Thermoelectric (TE) devices can directly convert heat into electricity under safe, clean, and environmentally friendly operation [1,2]. Due to this, TEs can be used in radioisotope TE generators for spacecrafts, as solar TE generators, in automobiles and industries utilizing heat from hot exhausts as heat source, and to power wearable devices and sensors, among other applications [3,4]. A good TE material should have a high power factor (*PF*) and a low thermal conductivity. The $PF=S^2\sigma$ is determined by the Seebeck coefficient (*S*) and the electrical conductivity (σ). Some of the most significant recent improvements in TE materials performance have been mainly achieved by the reduction of the thermal conductivity, but strategies to improve the *PF* have been less successful [5,6], since they require decoupling the Seebeck coefficient from the electrical conductivity [7,8].

Recently, an innovative approach to increase the *PF* has shown above 3 times improvements of this parameter, which are among the highest reported [9]. This new concept is based on the combination of a nanostructured and porous TE solid that is permeated with an electrolyte, with the intention of improving the TE properties of the solid by means of different interactions that can occur with the electrolyte. In that work, using an Sb-doped SnO_2 film as a solid, and 1 M $LiBF_4$ dissolved in 3-methoxipropionitrile (3-MPN) as the electrolyte, the *PF* was increased 3.4 times. The enhancement was due to a more than 60% decrease in the electrical resistivity of the solid without a significant variation of the Seebeck coefficient. In addition, the ionic liquid 1-butyl-3-methylimidazolium iodide was also employed as electrolyte, and showed an enhancement of 2.4 times in the *PF*, due to a more than 82% decrease in the electrical resistivity and a 35% reduction in the absolute value of the Seebeck coefficient.

Here, we explore the use of a different kind of electrolyte in this promising solid-electrolyte system. Unlike the previously employed non-electroactive salts, such as $LiBF_4$, and the ionic liquids, we have used a solution of an electroactive molecule as electrolyte. Electroactive species, also known as redox molecules, are able to exchange electrons with the nanostructured solid, which could lead to new mechanisms of *PF* improvements in the hybrid system. Inorganic complexes are common electroactive species. For our study, we have chosen a Cr (III) acetylacetonate [$Cr(acac)_3$] complex

dissolved in the 3-MPN organic solvent. As TE solid we used the same Sb-doped SnO_2 film. In this different system, we show that significant *PF* improvements are also found. Moreover, using impedance spectroscopy, we analyze the mechanisms that lie behind these identified improvements.

3.2. Experimental section

Nanostructured and porous Sb:SnO_2 films were fabricated using microscope slide glasses of 25 mm x 15 mm size and 1 mm thickness as substrates. They were cleaned before film deposition by means of three sonication steps of 15 min in different media. In the first step, sonication was performed using a soap (Labkem, SOAP-0685K0)/water solution (1:10 v/v). Then, distilled water to remove soap excess was used as second step. Finally, isopropanol (Labkem, PROL-P0P-5K0) media was employed for sonication. After this, substrates were dried under compressed air flow and treated in a UV ozone cleaner (Ossila, L2002A2-UK) for 20 min. Subsequently, an Sb:SnO_2 colloidal aqueous dispersion (Keeling & Walker, A20W) was deposited by spin coating (Laurell, WS-650MZ-23NPPB) at 2500 rpm for 15 s, covering a centred area of the substrate of 10 mm x 5 mm. A total of four layers were deposited. After each deposition, a drying process was carried out on a hot plate at 100 ºC for 10 min. Finally, the films were annealed at 550 °C for 45 min in a furnace (Nabertherm, 400-1) with a 3 °C/min heating rate. Scanning electron microscopy (SEM) images of the films and their composition were obtained using a JEOL 7001F instrument (Oxford Instruments) with energy-dispersive X-ray spectroscopy (EDX). The films structure before and after annealing was tested by X-ray diffraction (XRD) using a Bruker D4-Endeavor instrument.

The films were contacted at their ends by Pt contacts, which were deposited by sputtering (Quorum, Q300T D Plus) during 60 s after growing an initial Cr seeding layer during 15 s (see Fig. 3.2a). A 0.1 M solution of chromium (III) acetylacetonate [$Cr(acac)_3$] (Sigma Aldrich, ref. 202031-5G) dissolved in the high boiling point organic solvent 3-methoxypropionitrile (3-MPN) (Sigma Aldrich, ref. 65290-250MK-F) was employed as electrolyte. All the compounds were used as received and handled in a glove box (MBRAUN, Labstar 4516) under inert atmosphere conditions to avoid the presence of moisture. The stock electrolyte solution was prepared in a sealed vial with septum, and stored under vacuum (pressure of -1 bar) before use. Nuclear magnetic resonance (NMR) spectra were recorded on Bruker spectrometers operating at 300 MHz (^{1}H NMR) and

referenced to $SiMe_4$ (δ in ppm and J in Hertz). ^1H NMR experiments were recorded at room temperature in CD_3CN (Sigma Aldrich, ref.151807-25G) to both the 3-MPN solvent and the 0.1 M [$Cr(acac)_3$] solution prepared.

The Seebeck coefficient and the electrical resistance were measured in a homemade setup (see Fig. 3.2b to d) inside a glove box (Sicco, WV 1992-08-55) under N_2 flow. In order to establish a temperature difference in the setup, two copper blocks were used. One of them, with 3 cartridge heaters inserted (Watlow, ref C1E13-L12) and 30 mm x 30 mm x 10 mm dimensions, acted as the heat source. A second larger copper block (50 mm x 50 mm x 30 mm) was used as the heat sink (see Fig. 3.2b). The glass substrate with the film deposited was placed on top of the copper blocks, which are separated by a polytetrafluoroethylene (PTFE) bridge (see Fig. 3.2b). The latter helps to avoid breaking the sample during the time a pressure is applied by an O-ring. Thermal grease (RS, ref. 2173835) was used at the substrate/copper interfaces to improve the thermal contacts.

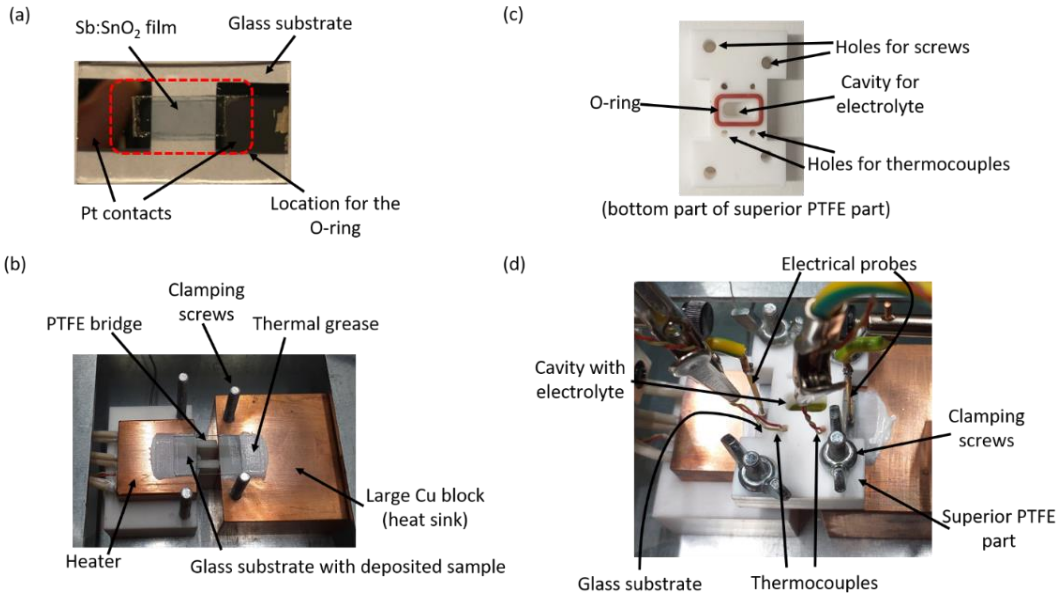

Fig. 3.2. Photographs of (a) the contacted film prepared, (b) the characterization setup with the top PTFE block not assembled, (c) the bottom part of the top PTFE block, and (d) the complete setup assembled.

A holed PTFE block with a rectangular O-ring at the bottom side was placed on top of the glass substrate to allow the location of the electrolyte (see Fig. 3.2c). The location of the O-ring pressing the film can be seen in Fig. 3.2a. It should be noted that the pressure is held on the Pt contacts, not on the Sb-doped SnO_2 film. The PTFE block also has holes for positioning two thermocouples and several screws to provide a gentle pressure for sealing and avoiding liquid electrolyte leakage. Two K-type thermocouples (RS, ref. 8140134) were placed on top of the glass substrate aligned at the ends of the Pt contacts

through the PTFE holes with a bit of thermal grease at their tips for thermalization (see Fig. 3.2d). The electric contacts to the external circuit were made with two spring probes (RS, ref. 2615092) contacting at the edges of the Pt contacts, as shown in Fig. 3.2d.

Seebeck coefficient values were obtained from the slope of the open-circuit potential V_{oc} versus temperature difference ΔT plot. The V_{oc} was measured with a Keithley 2182A nanovoltmeter, and the temperature difference was varied in steps of ≈1 K from 0 up to ≈5 K by powering the cartridge heaters by means of a Watlow EZ-Zone PM temperature controller. The film electrical resistance (R) was obtained from the slope of the current-voltage I-V curve under no temperature difference. The I-V curves were measured using a Keithley 2450 source meter in 4-probe mode, scanning the current with a delay time of 2 s. Two spring probes contacted on the Pt contacts at each side. In this way, the parasitic resistance of the cables could be removed, and only the electrical resistance of the film and the Pt/film contact is taken into account. Since the resistance of the film is expected in the order of kΩ (as it will be shown below), the electrical contact resistance can be neglected. All the electrical measurements were recorded using coaxial cables, to avoid electrical interferences from the surroundings. The relative errors of the slopes from the fittings to the corresponding plots for S and R were lower than 2% and 1%, respectively, for both parameters.

Impedance spectroscopy measurements using the same 4-probe configuration as described above were performed under a ΔT=5 K. Measurements were conducted in galvanostatic mode in the 1-0.01 Hz frequency range, using a dc current value of 0 A and 10 nA amplitude. A Metrohm-Autolab PGSTAT204 instrument, equipped with a FRA32M frequency response analyzer was employed for these measurements.

3.3. Results and discussion

Fig. 3.3 shows the SEM images of different Sb:SnO_2 films prepared. Fig. 3.3a and b correspond to a film before being in contact with an electrolyte. It can be seen that the film is formed by interconnected nanoparticles of sizes from 6 to 10 nm. It can also be observed the presence of pores in the 2-50 nm range. From Fig. 3.3b, the film thickness was estimated to be around 0.9 µm. Fig. 3.4 shows the XRD patterns of a Sb:SnO_2 film before and after the annealing. In both cases, a single phase was identified (cassiterity SnO_2, R040017, RRUFF Database), which is not modified after the annealing process. In addition, no additional peaks were found due to Sb, indicating that it acts as a dopant in

the structure. It should be noticed that the broad background peak that appears at the lower 2θ values is due to the glass substrate, which lies underneath the film.

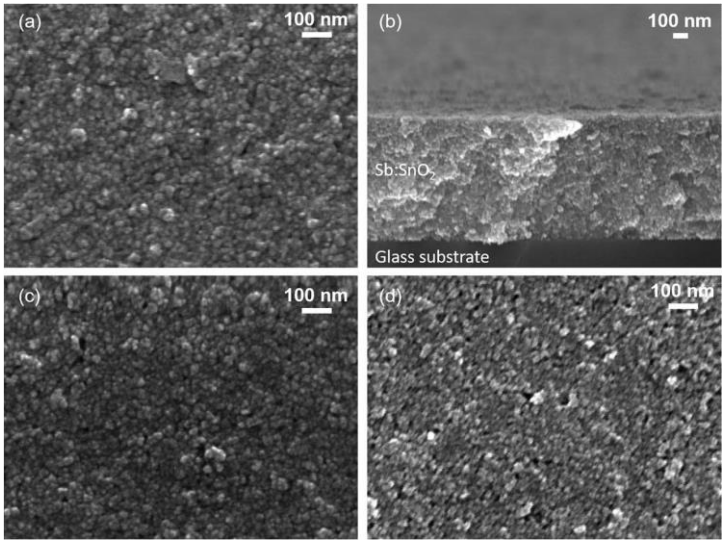

Fig. 3.3. (a) Top and (b) cross-section SEM images of an Sb-doped SnO_2 film before being in contact with an electrolyte. Top SEM images of an Sb:SnO_2 film after being in contact with (c) the 0.1 M $Cr(acac)_3$ solution in 3-MPN and (d) with only 3-MPN.

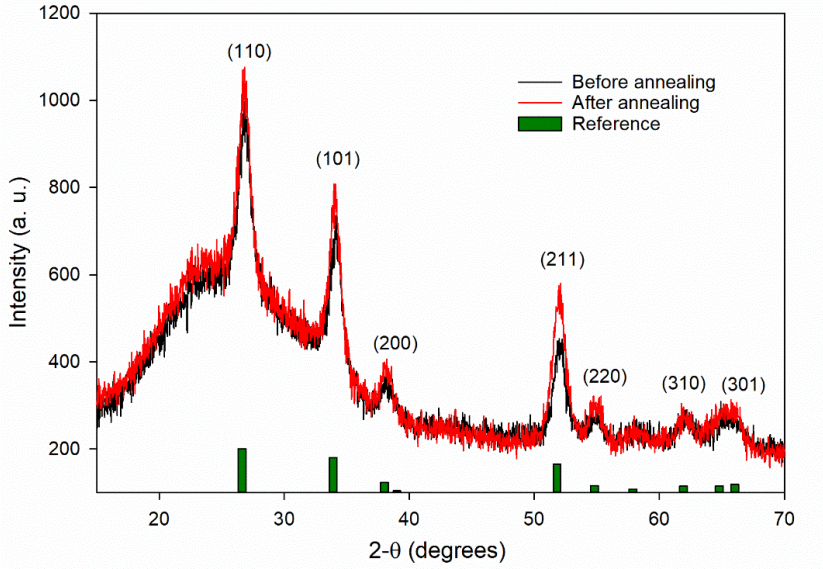

Fig. 3.4. XRD patterns of an Sb:SnO_2 film deposited on a glass substrate before and after annealing. The reference bars correspond to the indexation of the diffraction peaks for SnO_2 cassiterite (R040017, RRUFF Database).

The TE properties of the different systems evaluated can be seen in Table 3.1. These properties are obtained from the measurements shown in Fig. S3.1 and Fig. S3.2. First, three Sb:SnO_2 films without and with the $Cr(acac)_3$ electrolyte were tested (films 1-Cr to 3-Cr). Then, a configuration without the presence of the oxide film, just the Pt contacts and the $Cr(acac)_3$ electrolyte, was analysed (No film). Finally, three Sb:SnO_2 films without and with only the 3-MPN solvent as electrolyte [without $Cr(acac)_3$] were

measured (films 1-3MPN to 3-3MPN). Fig. S3.1 shows the V_{oc}-ΔT and *I-V* plots for the films 1-Cr to 3-Cr, with and without the presence of the $Cr(acac)_3$ electrolyte, and Fig. S3.2 the same plots for the films 1-3MPN to 3-3MPN.

Table 3.1. Seebeck coefficient and resistance of the different systems evaluated, indicating the variations of these parameters and the power factor (*PF*) improvements produced. Temperatures at which the measurements were performed are also indicated between brackets. For the electrical resistance measurements, the values correspond to the temperature when ΔT=0 K.

	Seebeck coefficient (μV/K)			**Electrical resistance (kΩ)**			$PF_{with}/PF_{without}$
	Without electrolyte	With electrolyte	Variation (%)	Without electrolyte	With electrolyte	Variation (%)	
1-Cr	-57.5 (18.4 ºC)	-44.4 (21.0 ºC)	-23.5	11.1 (20.2 ºC)	1.87 (22.6 ºC)	-83.2	3.49
2-Cr	-57.9 (18.8 ºC)	-43.8 (21.6 ºC)	-24.3	11.8 (20.7 ºC)	1.95 (22.1 ºC)	-83.5	3.48
3-Cr	-57.6 (19.3 ºC)	-45.0 (20.1 ºC)	-21.9	11.4 (20.4 ºC)	2.07 (22.3 ºC)	-81.8	3.34
No film	-	-	-	-	890 (17.9 ºC)	-	-
1-3MPN	-53.4 (12.2 ºC)	-40.4 (17.9 ºC)	-24.2	7.44 (15.0 ºC)	4.33 (19.9 ºC)	-41.8	0.99
2-3MPN	-51.3 (14.2 ºC)	-39.2 (19.8 ºC)	-23.4	10.0 (17.1 ºC)	6.25 (20.8 ºC)	-37.6	0.94
3-3MPN	-52.1 (13.2 ºC)	-39.3 (18.4 ºC)	-24.5	8.20 (16.2 ºC)	4.61 (20.4 ºC)	-43.7	1.01

Films 1-Cr to 3-Cr were measured first without the presence of the electrolyte. Then, they were tested after the $Cr(acac)_3$ electrolyte was injected and a steady state value of the V_{oc} was observed, which in some cases took several hours. As it can be seen in Table 3.1, the absolute value of the Seebeck coefficient decreased by an average value of 23.2% due to the presence of the electrolyte. On the other hand, a significant average drop of 82.8% in the electrical resistance was found, therefore, an average 3.4 times improvement in the *PF* was obtained (see Table 3.1). This remarkable *PF* improvement is the same than the highest reported in our previous study [9], which was obtained using a 0.1 M $LiBF_4$ solution in 3-MPN as electrolyte. In order to discard that the reduction in the resistance could be due to electrical conduction through the electrolyte, a configuration with only the electrolyte and the Pt contacts (No film) was measured. A high electrical

resistance of 890 kΩ was found, which indicates that the electronic transport is only taking place through the oxide film. Due to this large resistance value, the Seebeck coefficient could not be determined for the No film configuration, since the instrument could not properly measure the V_{oc}.

To investigate further the role of the $Cr(acac)_3$ complex, three identical systems consisting of Sb:SnO_2 and only the 3-MPN solvent in the electrolyte [no $Cr(acac)_3$ complex] were tested (1-3MPN to 3-3MPN in Table 3.1). In this case, the absolute value of the Seebeck coefficient drops an average value of 24.0%, similar to the case of the system with the Cr complex in the electrolyte. On the other hand, the resistance experiences an average drop of 41.0%, which is lower than the 82.8% drop achieved in the Cr complex system. The observed variations led to basically no average variation of the *PF*. This clearly indicates that the Cr complex is necessary in the electrolyte to produce the *PF* improvements and to achieve lower resistance values. It should be noticed that the temperatures at which the different experiments from Table 3.1 were performed differ in many cases, since it is very difficult to control the ambient temperature of the laboratory. Although significant changes in temperature could produce variations of the properties determined, the variations observed between the systems without and with electrolyte are below 3 ºC for the Cr complex electrolyte, and below 6 ºC for only 3-MPN cases. These not very large temperature differences cannot produce the variations observed in the TE parameters (*S* and *R*). In order to verify this, we measured the variation with temperature of *S* and *R* for one of the films (without the presence of electrolyte). Results can be seen in Fig. S3.4, which shows very small changes in both properties with temperature.

In order to investigate if the variations of the TE properties observed in Table 3.1 come from possible changes in the morphology and composition of the films, both parameters were analysed by SEM and EDX, respectively. Top view SEM images of films before being in contact with electrolytes and after exposure to the 0.1 M solution of the $Cr(acac)_3$ complex and to only 3-MPN are shown in Fig. 3.3. It can be seen that all the films show a similar morphology, no significant differences are found. On the other hand, the chemical compositions of the films shown in the SEM images are presented in Table 3.2. It can be seen that no significant changes occur again. Thus, the variation of the TE properties identified in Table 3.1 are not due to changes produced in the morphology or chemical composition of the films.

Table 3.2. Chemical compositions obtained by EDX for three different Sb:SnO_2 films: (i) before being in contact with an electrolyte, (ii) after being in contact with a 0.1 M $Cr(acac)_3$ solution in 3-MPN and (iii) after exposure to only 3-MPN.

Element	Film	Atomic%
Sn	Before contact with electrolyte	30.2
	After contact with the Cr complex solution	30.5
	After contact with only 3-MPN	30.4
Sb	Before contact with electrolyte	3.72
	After contact with the Cr complex solution	3.37
	After contact with only 3-MPN	3.57
O	Before contact with electrolyte	66.1
	After contact with the Cr complex solution	66.1
	After contact with only 3-MPN	66.1

In order to further understand the reasons behind the variations of the TE properties observed, impedance spectroscopy measurements were performed under 5 K temperature difference, which is a possible temperature gradient for the system under operation using body heat. Fig. S3.5 shows the impedance spectra for the systems in contact with the Cr complex solution and only the 3MPN. It can be observed that all the impedance spectra show points lying around a specific value of the Z' axis, which indicates the presence of only an ohmic resistance in the system [10], attributed to the ohmic electronic conduction through the Sb:SnO_2 film. The presence of semicircles or other features is not found in any of the spectra after adding the electrolyte, which corroborates that no charge transfer to the electrolyte occurs under operation (no electrical conduction through the liquid), and the only existing process is the ohmic electrical conduction through the film. The impedance spectra were fitted to the equivalent circuit shown at the inset of Fig. S3.5a (a resistor) and the fitted parameters with their relative error are included in Table 3.3. It can be observed that the obtained resistances match with the resistances of Table 3.1 measured by the *I-V* curves, as expected.

The variation of the electrical conductivity of the oxide film by the presence of both electrolytes can be explained by the injection of electrons from the electrolyte to the film, since the mobility of the electrons is not expected to change as the films morphology and composition do not significantly vary as mentioned before. For the case of the systems with only 3-MPN, which is a solvent and is not expected to exchange electrons with the film, a possible mechanism leading to an increase in the number of free electrons can

come from the accumulation of electrons at the film/solvent interface after equilibration, which can produce a 'donor effect', since the 3-MPN is a polar molecule. This possible mechanism can be seen in Fig. 10 of ref. [11], and it is observed in SnO_2 when is used as humidity sensor.

Table 3.3. Resistance values without and with electrolytes extracted from the impedance spectra of Fig. S3.5. Relative errors from the fitting are indicated between brackets.

	Resistance (kΩ)	
	Without electrolyte	With electrolyte
1-Cr	10.9 (0.68%)	2.02 (0.42%)
2-Cr	11.6 (1.00%)	2.16 (0.42%)
3-Cr	11.2 (0.41%)	2.46 (0.39%)
1-3MPN	7.25 (0.82%)	4.28 (0.51%)
2-3MPN	9.77 (0.85%)	6.16 (0.50%)
3-3MPN	8.22 (0.76%)	5.02 (0.79%)

In the systems with $Cr(acac)_3$, the injection of electrons can be produced by the presence of both the 3-MPN solvent and the $Cr(acac)_3$ complex, which is an electroactive (redox) molecule, employed due to this property in redox flow batteries [12,13]. A higher injection of electrons is expected in the system with the complex, thus, leading to a higher reduction of the resistance. It is well known that a reduction in the electrical resistivity of a semiconductor typically produces a decrease in the absolute value of the Seebeck coefficient [6], as observed in Table 3.1. In this case, it is not clearly observed a more drastic reduction in the systems with the Cr complex, as it could be expected for their higher resistance variation. In any case, it should be noted that the differences in the variations produced are not extremely different.

3.4. Conclusions

We have studied the possibility of obtaining power factor improvements in a hybrid solid-liquid thermoelectric system. Unlike the electrolytes previously employed, we have used an electrolyte containing an electroactive molecule (chromium acetylacetonate) dissolved in 3-methoxypropionitrile solvent. The electrolyte permeated a nanostructured and porous Sb-doped SnO_2 film. An average power factor improvement of 3.4 times was achieved due to the presence of the electrolyte. The enhancement originated from an average decrease of 23.2% and 82.8% in the absolute value of the Seebeck coefficient and the electrical resistivity of the solid, respectively. Morphological changes and

variations in the chemical composition of the films were not observed by SEM and EDX analysis. An impedance spectroscopy study concluded that the power factor improvements are related to the donation of electrons from the electrolyte to the solid, which increases its electrical conductivity and the consequent drop in the Seebeck coefficient. These results show that the hybrid solid-liquid system concept could be also extended to electrolytes with electroactive species, able to exchange electrons with the solid, opening the possibility to study a huge number of possible redox molecules. In addition, it also offers the opportunity to test this new system using nanostructured and porous solids with better thermoelectric performance than Sb:SnO_2, such as Bi_2Te_3, which could lead to extraordinarily high power factors and also overall performance, since the thermal conductivity of the system is not expected to significantly increase due to the porosity of the solid and the low thermal conductivity of liquids (similar to that of polymers). This possibility will be investigated as future work.

Conflict of interest

The authors declare no conflict of interest.

Acknowledgements

This project has received funding from the European Union's Horizon 2020 research and innovation programme under grant agreement No 863222 (UncorrelaTEd project). We also acknowledge funding support from PID2021-122900NB-I00 financed by MICIN/AEI/10.13039/501100011033/ FEDER "Una manera de hacer Europa". G. G.-B gratefully acknowledges (RYC2019-026693-I/AEI/10.13039/501100011033) "El Fondo Social Europeo invierte en tu futuro'. Gobierno de Aragón/FEDER, UE (GA/FEDER, Reactividad y catálisis en química inorgánica, Group E50_20D). Raquel Oliver and Pepe Ortega are acknowledged for their technical support.

References

[1] Beretta D, Neophytou N, Hodges JM, Kanatzidis MG, Narducci D, Martin-Gonzalez M, et al. Thermoelectrics: From history, a window to the future. Materials Science and Engineering R: Reports 2019;138:210–55. https://doi.org/10.1016/j.mser.2018.09.001.

[2] He J, Tritt MT. Advances in thermoelectric materials research: Looking back and moving forward. Science 2017;357:1369–79. https://doi.org/10.1126/science.aak9997

[3] Champier D. Thermoelectric generators: A review of applications. Energy Convers Manag 2017;140:167–81. https://doi.org/10.1016/j.enconman.2017.02.070.

[4] Siddique ARM, Mahmud S, Heyst B van. A review of the state of the science on wearable thermoelectric power generators (TEGs) and their existing challenges. Renewable and Sustainable Energy Reviews 2017;73:730–44. https://doi.org/10.1016/j.rser.2017.01.177.

[5] Yan Q, Kanatzidis MG. High-performance thermoelectrics and challenges for practical devices. Nat Mater 2021;21:503–13. https://doi.org/10.1038/s41563-021-01109-w.

[6] Mehdizadeh Dehkordi A, Zebarjadi M, He J, Tritt TM. Thermoelectric power factor: Enhancement mechanisms and strategies for higher performance thermoelectric materials. Materials Science and Engineering R: Reports 2015;97:1–22. https://doi.org/10.1016/j.mser.2015.08.001.

[7] Tonga M, Wei L, Wilusz E, Korugic-Karasz L, Karasz FE, Lahti PM. Solution-fabrication dependent thermoelectric behavior of iodine-doped regioregular and regiorandom P3HT/carbon nanotube composites. Synth Met 2018;239:51–8. https://doi.org/10.1016/J.SYNTHMET.2018.03.007.

[8] Mardi S, Cataldi P, Athanassiou A, Reale A. 3D cellulose fiber networks modified by PEDOT:PSS/graphene nanoplatelets for thermoelectric applications. Appl Phys Lett 2022;120:33102–314. https://doi.org/10.1063/5.0075918/2832883.

[9] Márquez-García L, Beltrán-Pitarch B, Powell D, Min G, García-Cañadas J. Large Power Factor Improvement in a Novel Solid–Liquid Thermoelectric Hybrid Device. ACS Appl Energy Mater 2018;1:254–9. https://doi.org/10.1021/acsaem.7b00075.

[10] Bisquert J, Fabregat-Santiago F. Impedance spectroscopy: a general introduction and application to dye-sensitized solar cells. In: Kalyanasundaram K, editor. Dye-sensitized Solar Cells, EPFL Press; 2010, p. 457.

[11] Chen Z, Lu C. Humidity sensors: A review of materials and mechanisms. Sens Lett 2005;3:274–95. https://doi.org/10.1166/SL.2005.045.

[12] Bamgbopa MO, Shao-Horn Y, Almheiri S. The potential of non-aqueous redox flow batteries as fast-charging capable energy storage solutions: demonstration with an iron–chromium acetylacetonate chemistry. J Mater Chem A Mater 2017;5:13457–68. https://doi.org/10.1039/C7TA02022H.

[13] Liu Q, Shinkle AA, Li Y, Monroe CW, Thompson LT, Sleightholme AES. Non-aqueous chromium acetylacetonate electrolyte for redox flow batteries. Electrochem Commun 2010;12:1634–7. https://doi.org/10.1016/J.ELECOM.2010.09.013.

Supplementary information

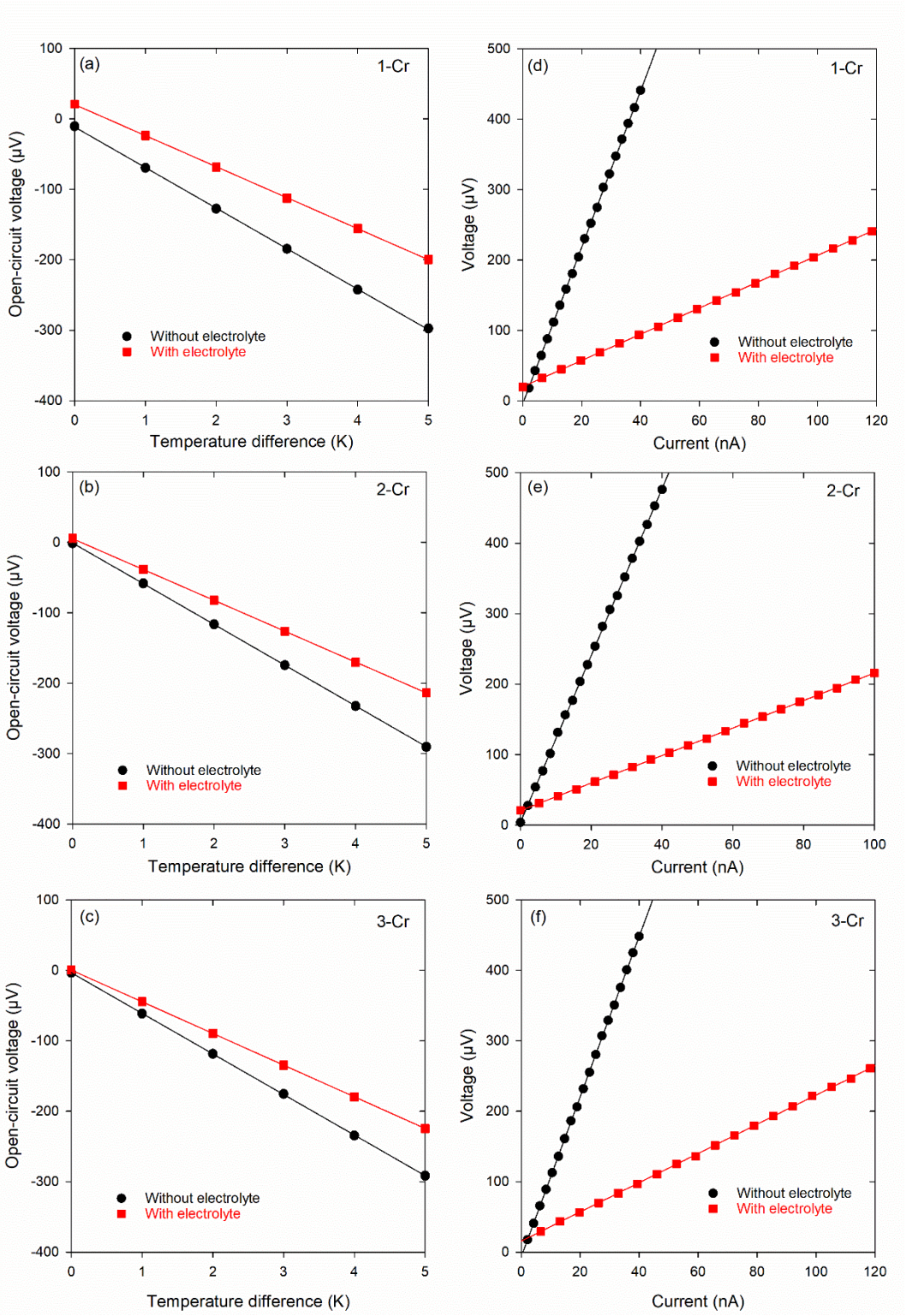

Fig. S3.1. (a-c) Open-circuit voltage vs temperature difference and (d-f) current-voltage plots for the systems 1-Cr to 3-Cr. Results with and without the presence of the 0.1 M $Cr(acac)_3$ in 3-MPN electrolyte are shown.

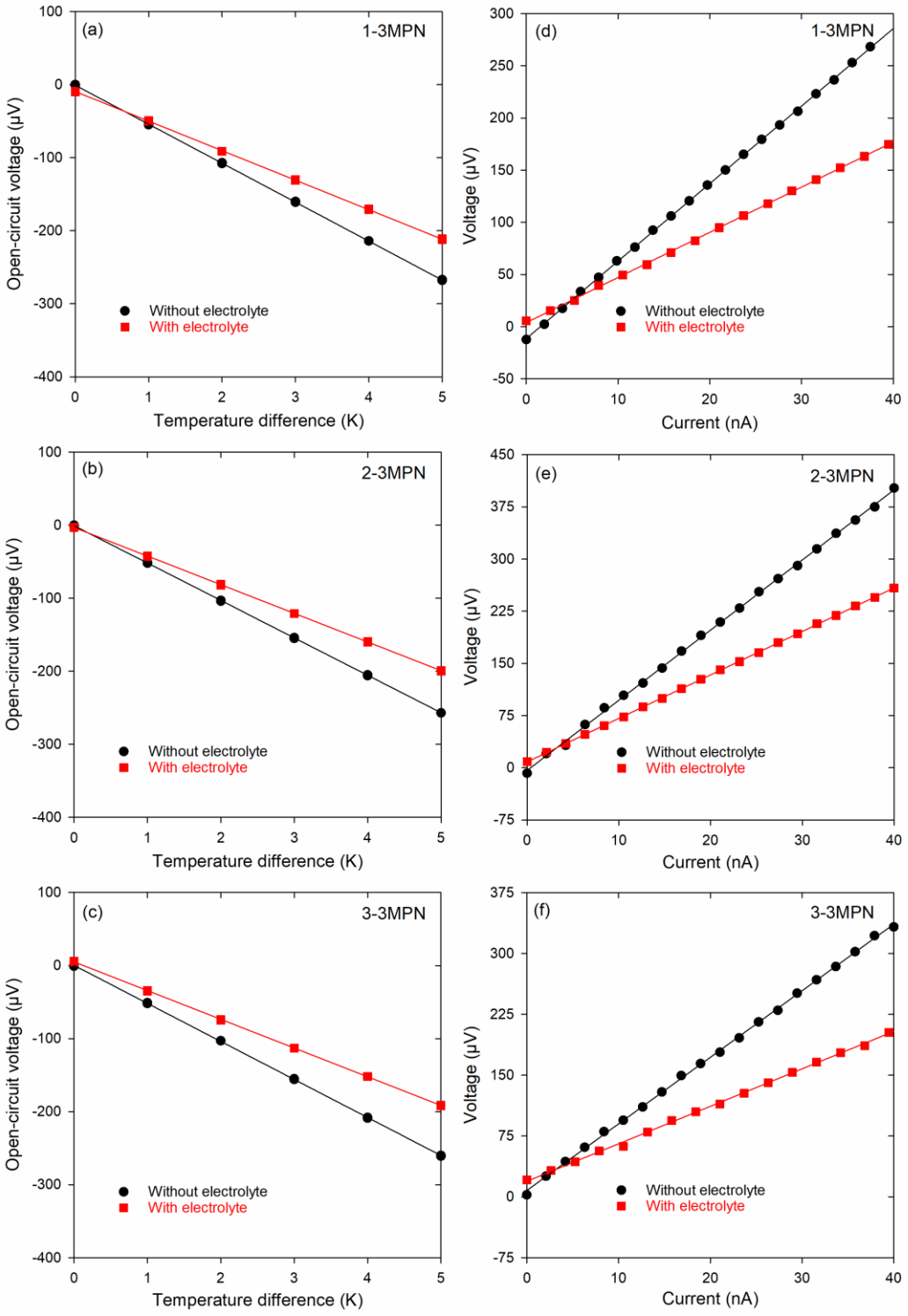

Fig. S3.2. (a-c) Open-circuit voltage vs temperature difference and (d-f) current-voltage plots for the systems 1-3MPN to 3-3MPN. Results with and without the presence of the 3-MPN solvent acting as electrolyte are shown.

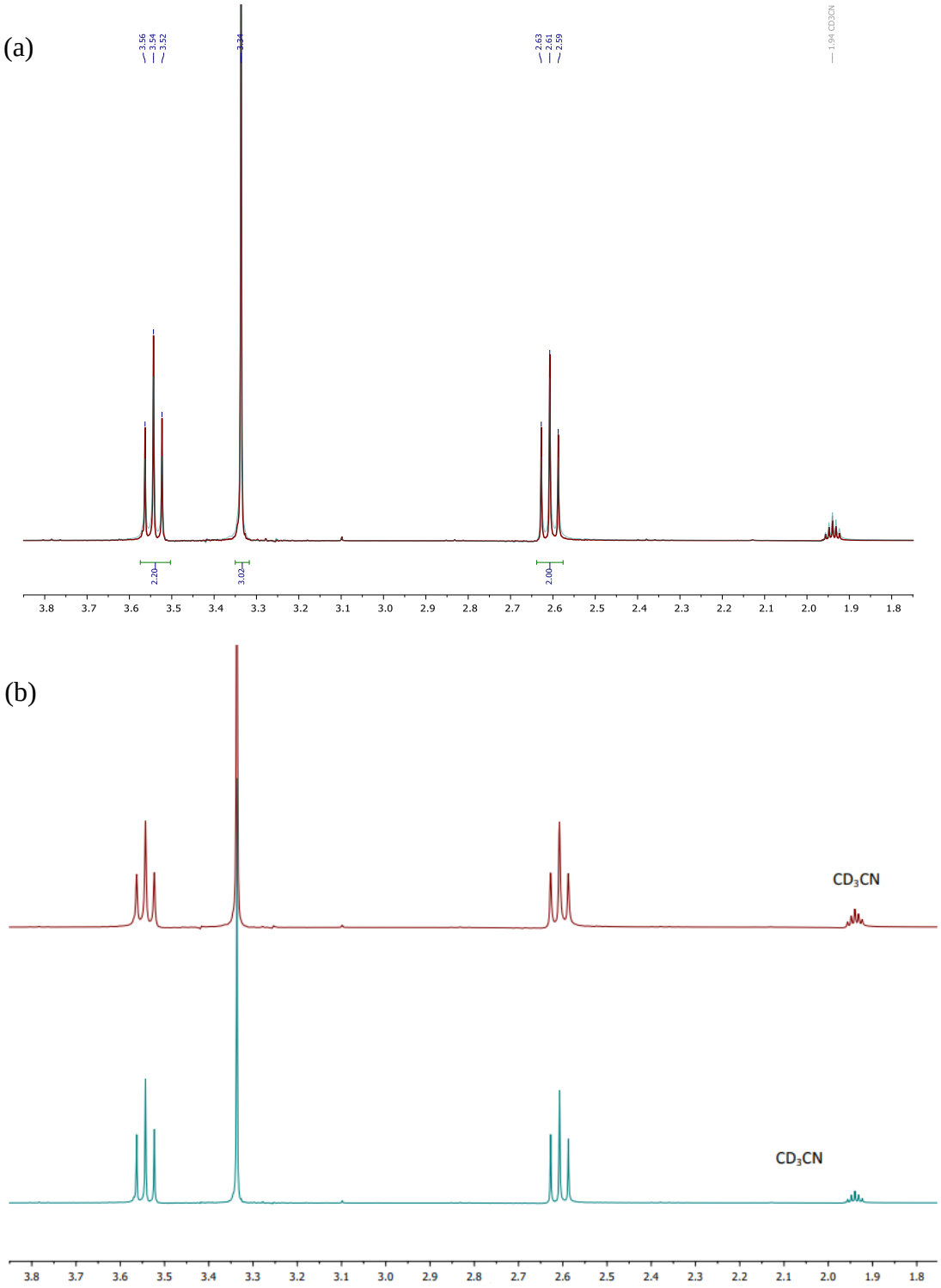

Fig. S3.3. ^{1}H NMR spectra in CD_3CN of the 3-methoxypropionitrile (3-MPN) (blue) and the 0.1M solution of $Cr(acac)_3$ in 3-MPN (red). (a) Overlapped spectra and (b) comparison with magnification. 3-Methoxypropionitrile (3-MPN): ^{1}H NMR (300 MHz, CD_3CN) δ 3.54 (t, *J*=6.0 Hz, 1H), 3.34 (s, 3H), 2.61 (t, *J*=6.0 Hz, 2H).

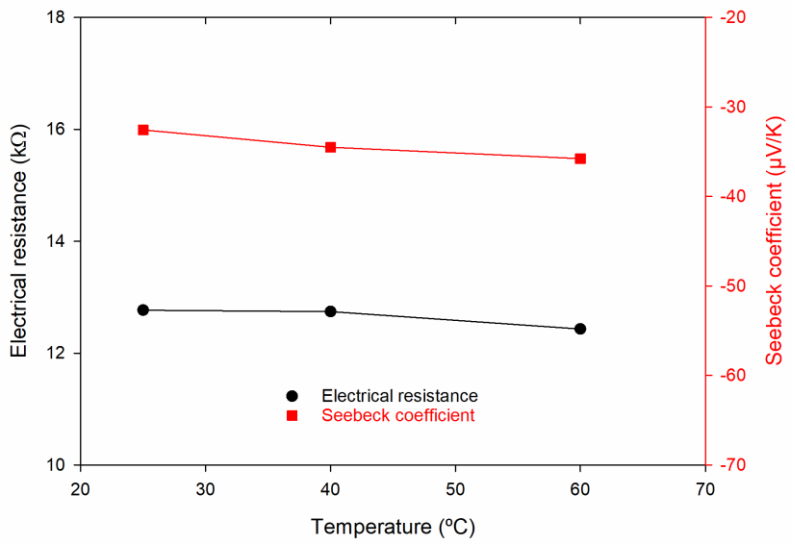

Fig. S3.4. Seebeck coefficient and electrical resistance as a function of temperature for an Sb:SnO_2 film.

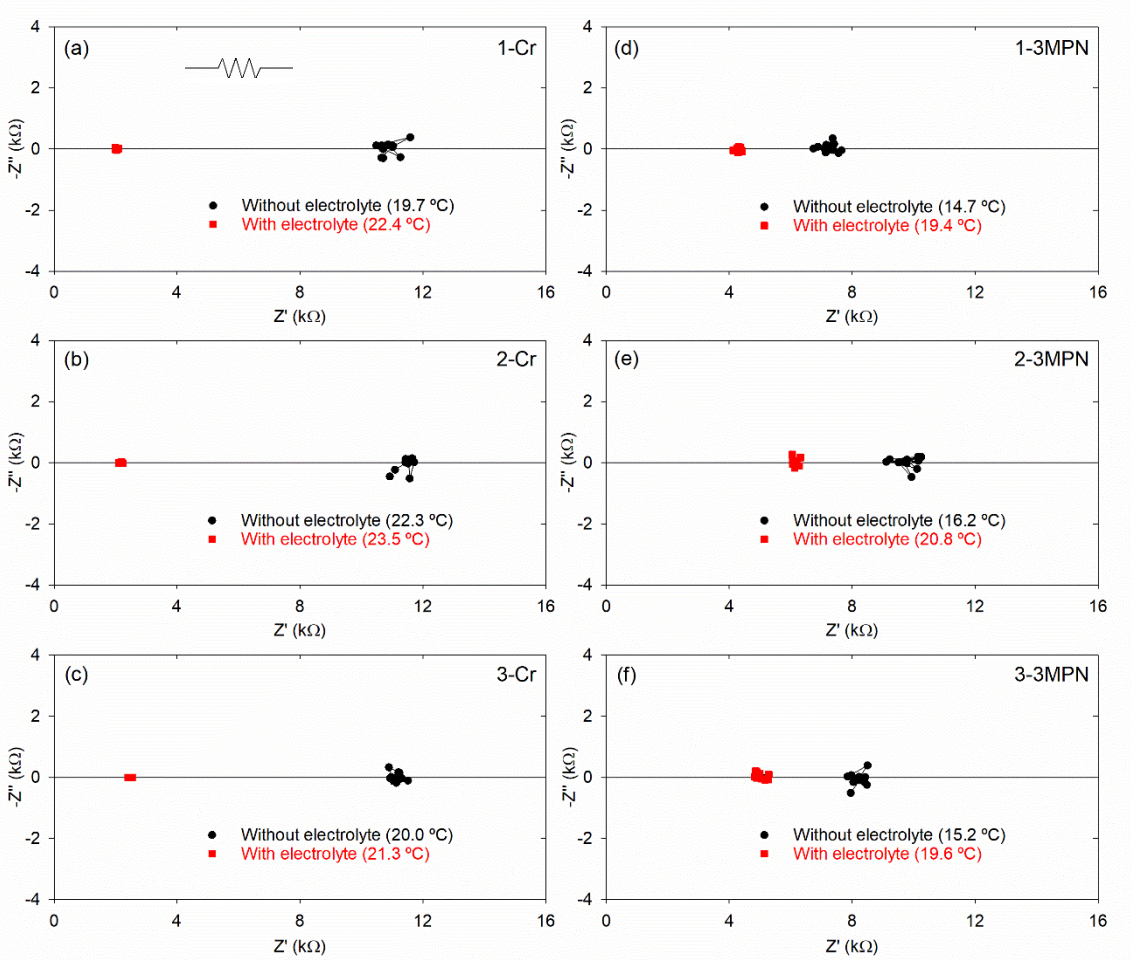

Fig. S3.5. Impedance spectroscopy spectra under ΔT=5 K of the Sb:SnO_2 films from Table 3.1. (a-c) Films 1-Cr to 3-Cr, without and with the presence of the 0.1 M $Cr(acac)_3$ solution in 3-MPN. (d-f) Films 1-3MPN to 3-3MPN, without and with the presence of only 3-MPN. The temperatures indicated in each case are the cold side temperatures. The inset in (a) is the equivalent circuit used.

4. Impedance spectroscopy analysis of a thermo-electrochemical cell under operating conditions

Impedance spectroscopy analysis of a thermo-electrochemical cell under operating conditions

S. Castro-Ruiz and J. García-Cañadas*

Department of Industrial Systems Engineering and Design, Universitat Jaume I, Av. Vicent Sos Baynat s/n, 12006 Castelló de la Plana, Spain.

* e-mail: garciaj@uji.es

2022 International Workshop on Impedance Spectroscopy (IWIS), 25-27 (2022).
DOI: 10.1109/IWIS57888.2022.9975126.

Graphical abstract

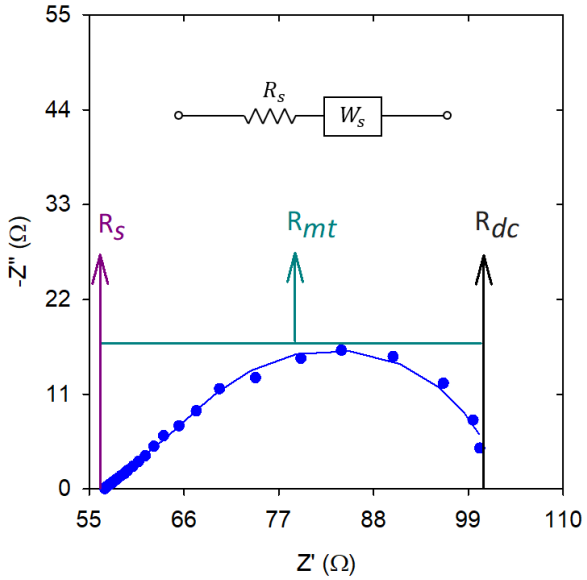

Fig. 4.1. Graphical abstract of the work: Impedance spectroscopy analysis of a thermo-electrochemical cell under operating conditions

Abstract

Low-grade (<200 ºC) heat is an abundant and available energy not generally exploited. In this regard, the so-called thermo-electrochemical cells have become a valid opportunity to harvest this ubiquitous source of heat. They are capable to convert heat into electricity by means of the temperature-redox potential dependency of a redox couple. In fact, they present temperature coefficient values in order of mV/K, much higher than solid-state thermoelectrics. In this work, a system formed by two Pt electrodes in contact with a 0.4 M ferro/ferricyanide aqueous solution has been studied by means of impedance spectroscopy under operating conditions (ΔT=40 K). The main processes which govern the performance of the system have been identified, which lead to different resistances: (i) electrolyte ionic resistance, (ii) charge-transfer resistance and (iii) mass-transport resistance. It was also demonstrated that the current-voltage characteristics of the device can be obtained knowing the open-circuit potential and performing a single impedance spectroscopy measurement, which determines the device dc resistance. This method can save a significant amount of time in many cases

KEYWORDS: Thermocells, thermogalvanic cells, liquid thermoelectrics, redox species.

4.1. Introduction

More than 60% of the total world energy is lost as waste heat. To take advantage of this ubiquitous source of energy, thermoelectric (TE) devices can directly convert heat into electricity under safe, clean, and environmentally friendly operation [1]. A good TE material should have a high Seebeck coefficient (S) and electrical conductivity (σ), but a low thermal conductivity (κ). To date, most of TE materials are inorganic solids, typically exhibiting low S values (200-250 μV/K), so low-temperature heat harvesting is still challenging [2]. In the last decades, thermo-electrochemical cells (or thermocells TECs or thermogalvanic cells) have gained attention as a suitable option for heat-to-electricity conversion at low temperatures (<200 ºC). They can provide temperature (or Seebeck) coefficients (α) values in order of mV/K, almost two orders of magnitude higher than usual solid-state TEs. The origin of this higher α is the redox potential (E)-temperature (T) dependence of the redox species in the electrolyte. Despite this advantage, device resistance values are much higher than in solid-state TEs, and consequently efficiencies are quite low. This is the main limitation of TECs, since thermal conductivities of electrolytes are typically low (<1 $Wm^{-1}K^{-1}$). Among all the TEC systems currently present, the one formed by two Pt electrodes separated by an aqueous solution of 0.4 M $K_3Fe(CN)_6/K_4Fe(CN)_6$ is the benchmark system in the literature. This device shows a high α (≈1.40 mV/K) and high kinetics parameters that lead to relatively large power outputs (P_{outs}) when the system is connected to an external load [3].

In order to obtain the total device resistance ($R_{I\text{-}V}$) and the power output, a current-voltage I-V curve is typically performed under steady state conditions. Waiting for these conditions at each point of the I-V curve can many times take a significant amount of time due to the slow diffusion rate of the redox species present in the electrolyte solution [4]. We present here a way to more easily obtain the I-V curve of a TEC, which requires the knowledge of the open-circuit potential and an impedance spectroscopy (IS) measurement at this voltage. The article shows first the experimental part. Then, explains the typical equivalent circuit of a TEC, and finally analyses the method to obtain the I-V curve.

4.2. Experimental section

A custom setup was built to characterise a fabricated TEC under operating conditions (see Fig. 4.2). The TEC consisted of two Pt electrodes (0.1 mm thickness and 1 cm x 1cm

area from Glentham, ref. GX2917) (see Fig. 4.2a). These pieces were cleaned before using them by means of two sonication steps of 15 min in different media. In the first step, sonication was carried out in distilled water to remove possible impurities. Finally, isopropanol (Labkem, ref. PROL-P0P-5K0) was employed for sonication. A solution of 0.4 M potassium ferrocyanide (Sigma Aldrich, ref. P3289-100G) and 0.4 M potassium ferricyanide (Fluka, ref. BCBT1564) in milli-Q water was employed as the electrolyte. All the chemicals were used as received.

In order to establish a temperature difference in the setup, two copper blocks were employed. One of them, with 30 mm x 30 mm x 10 mm dimensions and 2 cartridge heaters inserted (Watlow, ref. C1A-9604), acted as the heat source. A second larger copper block (40 mm x 40 mm x 10 mm) with a water circulation channel was used as the heat sink (see Fig. 4.2b). A water circulator (PolySicence, ref. SD07R-20-A12E) was employed to circulate the water and control the temperature of the Cu block.

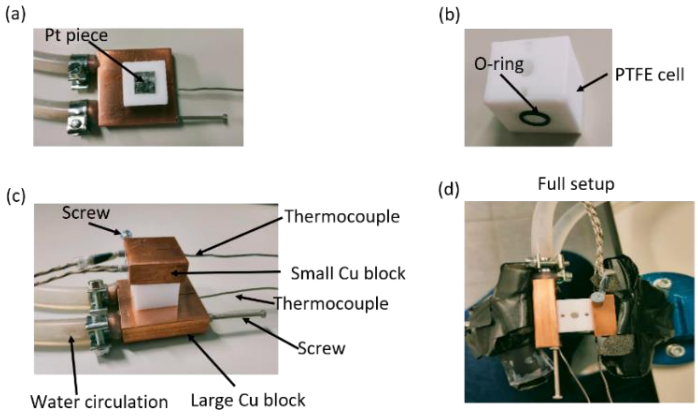

Fig. 4.2. Photographs of (a) a Pt electrode on top of the PTFE cell, (b) the PTFE cell with the O-ring, (c) the setup mounted but not clamped, and (d) the setup clamped.

The Pt electrodes were placed centred on top of the copper blocks, which are separated by a polytetrafluoroethylene (PTFE) cell which contains the electrolyte in a circular channel. The separation of the electrodes d was 14 mm. The channel is connected to a top hole for the injection of the electrolyte (see Fig. 4.2c).

To avoid leaks during the experiments, two O-rings were used pressing each of the electrodes (see Fig. 4.2c). The area of the O-ring, which determines the area of the electrodes in contact with the electrolyte was A=0.5 cm^2. A very little amount of thermal grease (RS, ref. 2173835) was put covering only part of the Pt/Cu interfaces to improve the thermal contacts. To contact the device, two screws were screwed in the Cu blocks, which served as metal contacts (see Fig. 4.2b). The screws were connected to the

apparatuses by crocodile connectors. Once all the elements were mounted, the setup was clamped using pieces of foam at the clamping points to reduce heat losses (see Fig. 4.2d).

The temperature coefficient, which indicates the variation of the open-circuit potential (V_{oc}) with the temperature difference (ΔT) was obtained from the slope of a V_{oc} vs ΔT plot. For all the points the cold side temperature (T_C) was kept constant at 21.5 ± 0.2 ºC. The V_{oc} was measured with a Keithley 2100 nanovoltmeter, and the temperature difference was varied in steps of ≈10 K, from 0 up to ≈40 K, by powering the two cartridge heaters inserted in the small Cu block by means of a Keithley 2601 sourcemeter. Two K-type thermocouples (RS, ref. 8140134) and a dual thermometer (RS, ref. 1316) were used to monitor the hot and cold side temperatures. Both thermocouples were inserted in holes performed at the Cu blocks. An *I-V* curve measurement was performed at ΔT=40 K (T_C =21.5 ºC) by fixing different voltage values and recording the corresponding current after steady state is reached. An IS measurement was carried out at the open-circuit potential when the cell was at ΔT=40 K (T_C =21.5 ºC). An amplitude of 15 mV and the 100 kHz-3 mHz frequency range was employed. The *I-V* and IS measurements were performed using a Vionic potentiostat from Metrohm Autolab, controlled by Intello 1.3.2 software.

4.3. Results and discussion

Fig. 4.3 shows the V_{oc}-ΔT plot of the fabricated TEC. It can be observed that the experimental points perfectly fit to a straight line of 1.35 ± 0.01 mV/K slope value, which is the temperature coefficient of the device. This value is very similar to the one typically reported in the literature (1.40 mV/K) [3].

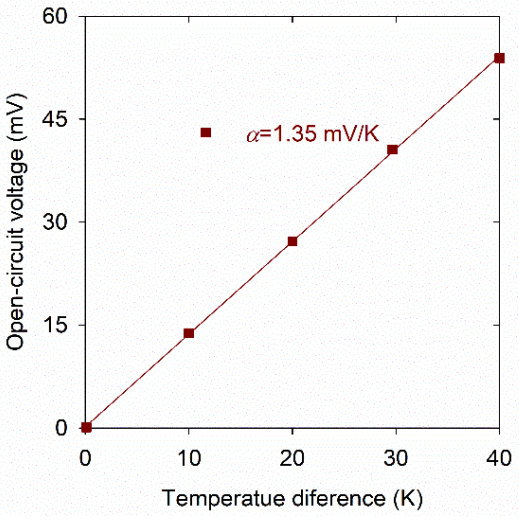

Fig. 4.3. Open-circuit vs temperature difference plot. The line represents the fitting to a straight line. The slope provides the temperature coefficient (α).

IS measurements were performed to the TEC. Before their analysis, we would like to remark that IS is a method that allows to identify and separate the different processes that occur in a device. Impedance results are typically analysed by means of equivalent circuits. Each element of the equivalent circuit describes one of the processes. One of the most well-known equivalent circuits is the Randles circuit [5], which can serve as the basis to analyse the impedance response in a TEC. Fig. 4.4 shows the Randles circuit (inset) and its typical Nyquist plot with absorbed boundary conditions.

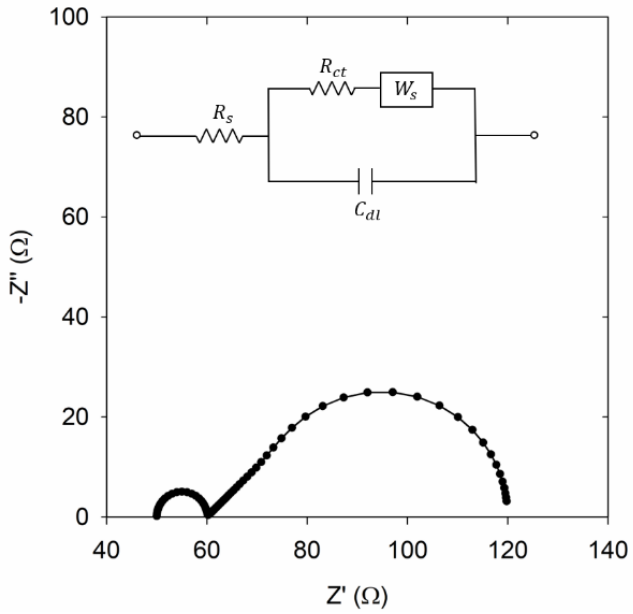

Fig. 4.4. Nyquist plot of a (shorted Warburg) Randles circuit (in the inset) obtained using R_s=50 Ω, R_{ct}=10 Ω, W_r=60 Ω, W_t=25 s, W_p=0.5 and C_{dl}=1 µF.

The intercept with the Z' axis at the left part (50 Ω) is the resistance of the electrolyte solution (R_s). The semicircle at the left is the parallel combination of the charge transfer resistance (R_{ct}) and the capacitance of the electrical double layer (C_{dl}). It should be noted that these two elements might not be observed when Pt electrodes are used, due to the catalytic effect of this metal, which highly reduces R_{ct}. The 45º line overlapped with a semicircle after the previous semicircle relates to the diffusion of redox species from the Pt/electrolyte interfaces towards the bulk of the solution. This process is represented by the Warburg shorted element (W_s). This element contains the mass-transport resistance (R_{mt}) associated with the transport of redox species from the Pt/electrolyte interfaces to the bulk of the solution.

The IS results of the TEC can be seen in Fig. 4.5. It can be observed that the spectrum can be fitted with a Randles circuit where the charge transfer process occurs very quickly (R_{ct} and C_{dl} do not appear, see inset of Fig. 4.5), as expected by the use of Pt as electrodes.

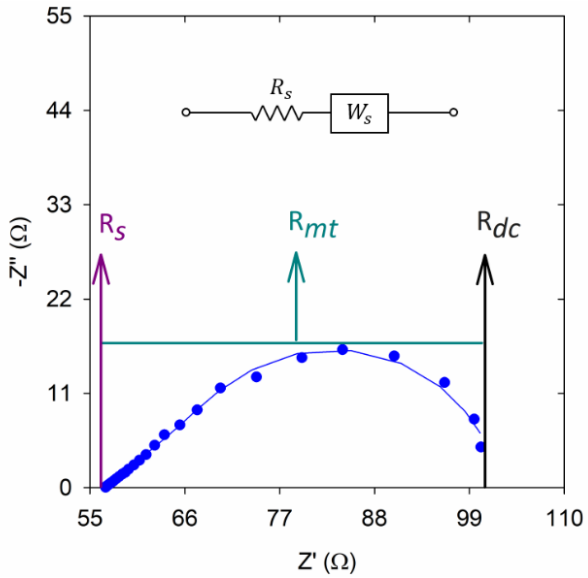

Fig. 4.5. Impedance spectrum of the thermocell under a temperature difference of 40 K (T_C=21.5 ºC). The line is the fitting to the equivalent circuit of the inset. The graphical determination of the series, mass transport and total resistances are also shown.

From the fitting, the values of R_s, R_{mt} and R_{dc} can be obtained (see Table 4.1), being R_{dc} the impedance value when frequency tends to zero (steady state). In this TEC, R_{dc} = R_s+ R_{mt} and is the total resistance of the system. The values of these resistances can also be estimated graphically, as indicated in Fig. 4.5. It should be noted that the Warburg element of the equivalent circuit might not be exactly the Warburg element of a Randles circuit, since the diffusion coefficients of the redox species might be affected by the temperature gradient in the device and other processes such as convection in the electrolyte could take place.

Table 4.1. Different parameters obtained and calculated from the impedance and *I-V* curve measurements. Values between brackets indicate relative errors from the fitting.

R_s (Ω)	R_{mt} (Ω)	R_{dc} (Ω)	$R_{I\text{-}V}$ (Ω)	$\mathcal{E}_R$ (%)	η_{TEC} (%)	η_r (%)
56.8 (0.13)	45.8 (0.75%)	102.6	106.7	3.84	0.0096	0.08

In addition to the IS measurement, the *I-V* curve of the TEC at the same condition (ΔT=40 K) was obtained (see Fig. 4.6). A linear correlation was observed for the current and the voltage. The slope of this correlation, $R_{I\text{-}V}$=106.7 Ω, represents the total device resistance. It can be observed that $R_{I\text{-}V}$ matches well with the R_{dc} value obtained from the IS results. The deviation between them $\mathcal{E}_R$ is just 3.84% (see Table 4.1). This fact allows the determination of the *I-V* curve just by knowing the V_{oc} at the given temperature difference and by extracting R_{dc} from an IS measurement at this voltage, which can

significantly simplify the experimental determination of the *I-V* curve, usually carried out fixing different load resistances (or voltages) and waiting for steady state to be reached, which ends up being a lengthy process in many cases.

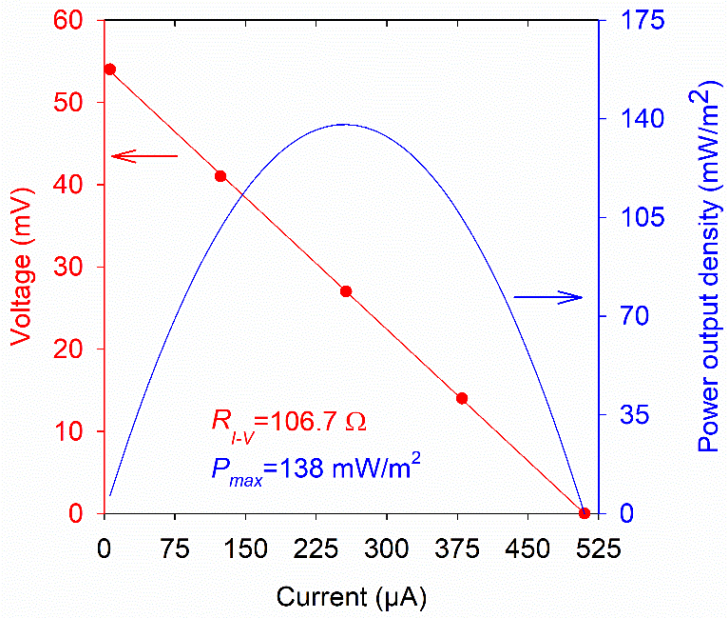

Fig. 4.6. Current-voltage and power output density curves at ΔT=40 K (T_C=21.5 ºC). The red line represents the fitting to a straight line, whose slope value is $R_{I\text{-}V}$.

In addition, the IS measurement makes possible to determine the contributions to the total device resistance, which in this case come from R_s and R_{mt}, contributing both nearly equal (see Table 4.1).

Finally, we would like to remark that the maximum power output density (P_{max}) obtained from the TEC was P_{max}=138 mW/m^2, in the same order of magnitude than the values reported in the literature [3]. The efficiency η_{TEC} and the Carnot efficiency η_r, calculated by means of the equations $\eta_{TEC}=V_{oc}I_{sc}/(4\kappa A\Delta T/d)$ and $\eta_r=\eta_{TEC}/(\Delta T/T_H)$, respectively, being $I_{sc}=I(V=0)$, κ the thermal conductivity of the electrolyte (0.5 Wm^{-1}K^{-1}) for our electrolyte [6], d=0.014 m the inter-electrode distance and T_H the hot side temperature, were also calculated and in agreement with the literature [3].

4.4. Conclusions

We have analysed the impedance spectroscopy results under operating conditions of a standard thermo-electrochemical cell (TEC) fabricated with Pt electrodes and 0.4 M ferro/ferricyanide aqueous electrolyte. A simplified Randles equivalent circuit was used to fit the impedance response at the open-circuit voltage value of the TEC under a temperature difference of 40 K. From the fitting, the resistance at steady state R_{dc} was

calculated as the addition of the series R_s and mass-transport R_{mt} resistances ($R_{dc}=R_s+R_{mt}$). It was found that the device resistance, obtained from the current-voltage curve, matches well with R_{dc}. Hence, knowing R_{dc} and the open-circuit voltage V_{oc} at the given temperature difference, the current-voltage curve can be determined, as well as the power output, which can reduce a significant amount of time in many cases.

Conflict of interest

The authors declare no conflict of interest.

Acknowledgements

This project has received funding from the European Union's Horizon 2020 research and innovation programme under grant agreement No 863222 (UncorrelaTEd project). Mauricio Solis-de la Fuente and Lourdes Márquez-García are also acknowledged for their technical support.

References

[1] He J, Tritt MT. Advances in thermoelectric materials research: Looking back and moving forward. Science 2017;357:1369–79. https://doi.org/10.1126/science.aak9997.

[2] Beretta D, Neophytou N, Hodges JM, Kanatzidis MG, Narducci D, Martin-Gonzalez M, et al. Thermoelectrics: From history, a window to the future. Materials Science and Engineering R: Reports 2019;138:210–55. https://doi.org/10.1016/j.mser.2018.09.001.

[3] Li W, Ma J, Qiu J, Wang S. Thermocells-enabled low-grade heat harvesting: challenge, progress, and prospects. Mater Today Energy 2022;27:101032–10150. https://doi.org/https://doi.org/10.1016/j.mtener.2022.101032.

[4] Massetti M, Jiao F, Ferguson AJ, Zhao D, Wijeratne K, Würger A, et al. Unconventional Thermoelectric Materials for Energy Harvesting and Sensing Applications. Chem Rev 2021;121:12465–547. https://doi.org/10.1021/acs.chemrev.1c00218.

[5] Macdonald JR. Impedance Spectroscopy. Wiley; 1987. https://doi.org/10.1002/0471716243.

[6] Quickenden TI, Mua Y. A Review of Power Generation in Aqueous Thermogalvanic Cells. J Electrochem Soc 1995;142:3985–93. https://doi.org/10.1149/1.2048446.

5. Nanostructured and porous antimony-doped tin oxide as electrode material for the heat-to-electricity conversion in thermo-electrochemical cells

Nanostructured and porous antimony-doped tin oxide as electrode material for the heat-to-electricity energy conversion in thermo-electrochemical cells

S. Castro-Ruiz and J. García-Cañadas*

Department of Industrial Systems Engineering and Design, Universitat Jaume I, Av. Vicent Sos Baynat s/n, 12006 Castelló de la Plana, Spain.

* e-mail: garciaj@uji.es

Electrochemistry Communications 161, 107683-107689 (2024).

DOI: 10.1016/j.elecom.2024.107683.

Graphical abstract

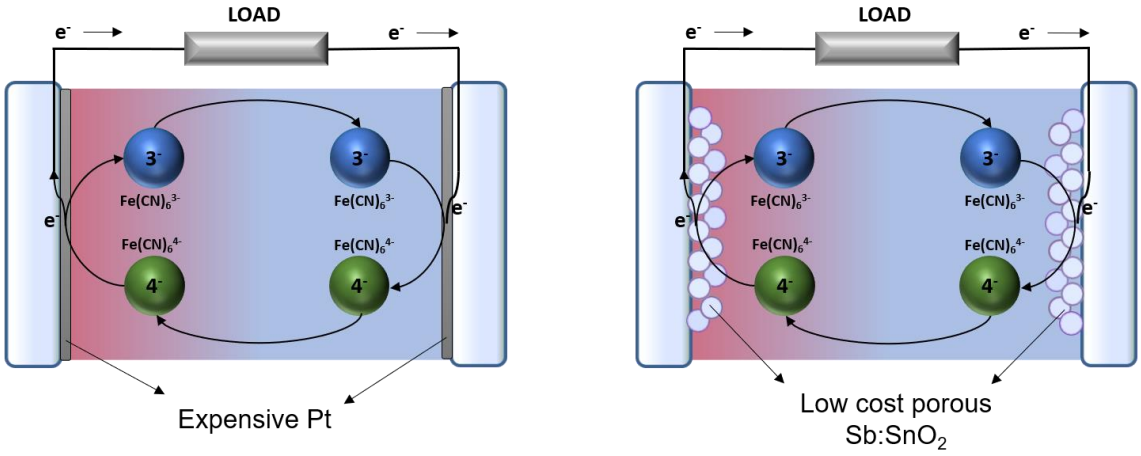

Fig. 5.1. Graphical abstract of the work: nanostructured and porous antimony-doped tin oxide as electrode material for the heat-to-electricity energy conversion in thermo-electrochemical cells

Abstract

Thermo-electrochemical cells (or thermogalvanic cells or thermocells, TECs) have gained attention as devices able to convert low temperature heat into electricity. Within TECs, Pt is one of the most employed electrodes, since it exhibits a fast transfer of electrons with the redox couple in the electrolyte. However, its high price represents a serious drawback. Here, we analyze the use of nanostructured and porous antimony-doped tin oxide ($Sb:SnO_2$) as electrode material. Electrodes of different thickness (320, 550 and 1550 nm) were fabricated by spin coating to study the effect of the electrode area in contact with the electrolyte. $F:SnO_2$ (FTO) glass was used as a substrate and the typical 0.4 M potassium ferro/ferricyanide aqueous solution served as electrolyte. An impedance spectroscopy analysis under operating conditions (10 K temperature difference) showed that the $Sb:SnO_2$ electrodes exhibit the same excellent kinetics as Pt for all the different thickness. On the other hand, the power output density was thickness independent, since the temperature coefficients and the series and mass-transport resistances were similar, leading to no performance improvements when the electrode area in contact with the electrolyte was significantly increased. Finally, the Carnot-related efficiencies estimated for the $Sb:SnO_2$ cells were in the same order of magnitude as for Pt electrodes. These results open the possibility to use $Sb:SnO_2$ as a suitable electrode in TECs at low cost.

KEYWORDS: Thermocell, thermogalvanic cell, metal oxide, ATO, porous electrode.

5.1. Introduction

Our planet is currently facing a very critical situation related to the high energy demand imposed by our society. This demand is still mostly covered by the use of fossil fuels, which produce large amounts of greenhouse gases that are causing the global warming. Under this scenario, it is imperative to develop more sustainable and environmentally friendly energy routes [1]. More than 60% of the total energy used is lost as waste heat, being more than 80% at low temperature (<100 ºC) [2]. Therefore, it would be highly convenient to use this vast amount of energy cleanly, sustainably and cheaply in order to obtain useful energy (e.g. electricity) [3,4].

Thermo-electrochemical cells (or thermocells, or thermogalvanic cells, TECs) have gained attention in the last decade due to their capability to produce electricity by using low-temperature heat [5,6]. Liquid TECs are formed by two electrodes (usually Pt) in contact with a solution that contains a redox couple (electrolyte). The benchmark TEC consists of two Pt electrodes in contact with an aqueous solution of 0.4 M potassium ferro/ferricyanide [7]. When a temperature difference ΔT is present, these devices generate an open-circuit voltage V_{oc} due to the temperature dependency of the redox couple potential. One of the main advantages of TECs is that their temperature coefficient α (also called Seebeck coefficient) is in the order of mV/K, which is one/two orders of magnitude higher than in solid-state thermoelectric materials. However, their efficiency η_{TEC} and Carnot-related efficiency [$\eta_r=\eta_{TEC}/(\Delta T/T_H)$, being T_H the hot side temperature] values are still low (below 0.1% and 1.0%, respectively) in most of the cases, mainly due to their high electric resistance [8]. In addition, the commonly used electrode, Pt, is very expensive, which is another serious drawback for their widespread application.

Suitable electrodes for TECs should have high electrical conductivity to effectively transport the electrons to/from the external circuit and small charge-transfer resistance (fast exchange of electrons between the redox species and the electrodes) at low cost. Several alternative electrodes to Pt have been reported, many of them exhibiting porosity to achieve a large surface area to minimize the charge-transfer resistance. Some examples are single- and multi-walled carbon nanotubes [9,10] or aerogel-printed carbon nanotubes [11]. In addition, increasing the electrolyte concentration has been reported to be an effective method to obtain large P_{out} in TECs [12]. In this sense, concentrations up to 2.4 m were obtained for the ferro/ferricyanide electrolyte producing the so-called water-in-

salt electrolyte. Furthermore, a 0.9 M concentration was achieved by replacing K^+ by NH_4 cations in the same electrolyte increasing P_{out} [13].

Here, we explore the use of nanostructured and porous antimony-doped tin oxide $Sb:SnO_2$ (ATO) as electrode in TECs. Porous metal oxides, like ATO, are used as electrodes in different energy-related systems, such as batteries [14], solar cells [15] and supercapacitors [16], where they show high chemical stability and large surface area. Nevertheless, these metal oxides have been hardly employed in TECs, although they have been reported to display good electrochemical behaviour [17]. To our knowledge, there are only two cases in the literature. On one hand, it was reported the use of nanostructured Ni/NiO micro-sphered electrodes in a TEC that achieved a power density value of 1.72 W/m^2 [18]. On the other hand, a record of η_r=14.8% was recently achieved using asymmetric CoO electrodes in contact with a guanidium-boosted $Fe(CN)_6^{-3/-4}$ electrolyte [19]. In this article, we have prepared ATO films deposited on fluorine-doped tin oxide (FTO) coated glass substrates which also act as current collectors. The standard 0.4 M potassium ferro/ferricyanide aqueous electrolyte was used as electrolyte. We studied the effect of the ATO thickness and compared the performance with the standard Pt electrodes, obtaining similar behaviours.

5.2. Experimental section

Nanostructured and porous $Sb:SnO_2$ films were fabricated following a previously described procedure [20] using FTO-coated glasses of 25 mm x 25 mm size and 2.2 mm thickness as substrates (Sigma Aldrich, 735167-EA). These substrates were cleaned before the ATO film deposition by means of three sonication steps of 15 min in different media. In the first step, sonication was performed using a soap (Labkem, SOAP-0685K0)/water solution (1:10 v/v). Then, distilled water to remove soap excess was used as second step. Finally, isopropanol (Labkem, PROL-P0P-5K0) media was employed for sonication. After this, substrates were dried under compressed air flow and treated in a UV-ozone cleaner (Ossila, L2002A2-UK) for 20 min. Subsequently, an $Sb:SnO_2$ colloidal aqueous dispersion (Keeling & Walker, A20W) was deposited by spin coating (Laurell, WS-650MZ-23NPPB) at 2500 rpm for 15 s, covering a centred area of the substrate of 15 mm x 15 mm. Several layers (2, 5 and 10) were deposited. After each deposition, a drying process was carried out on a hot plate at 100 ºC for 10 min. Finally, the films were annealed at 550 °C for 45 min in a furnace (Nabertherm, 400-1) with a 3

°C/min heating rate. Scanning electron microscopy (SEM) images of the films were obtained using a JEOL 7001F instrument (Oxford Instruments).

Five different symmetrical TECs were prepared. Three of them using the FTO/ATO electrodes with the different number of ATO layers (2, 5 and 10). Another cell was fabricated using Pt electrodes, which were prepared by depositing Pt by sputtering (Quorum, Q300T D Plus) on FTO glass during 6 min. The last TEC employed only FTO glass as electrodes. All these electrodes can be seen in Fig. 5.2a. To improve the electrical contact, certain area of the electrodes was painted with Ag paint (RS, 186-3600), as also shown in Fig. 5.2a. A solution of 0.4 M potassium ferrocyanide (Sigma Aldrich, P3289-100G) and 0.4 M potassium ferricyanide (Fluka, BCBT1564) in milli-Q water was employed as electrolyte in all the cells. All the chemicals were used as received.

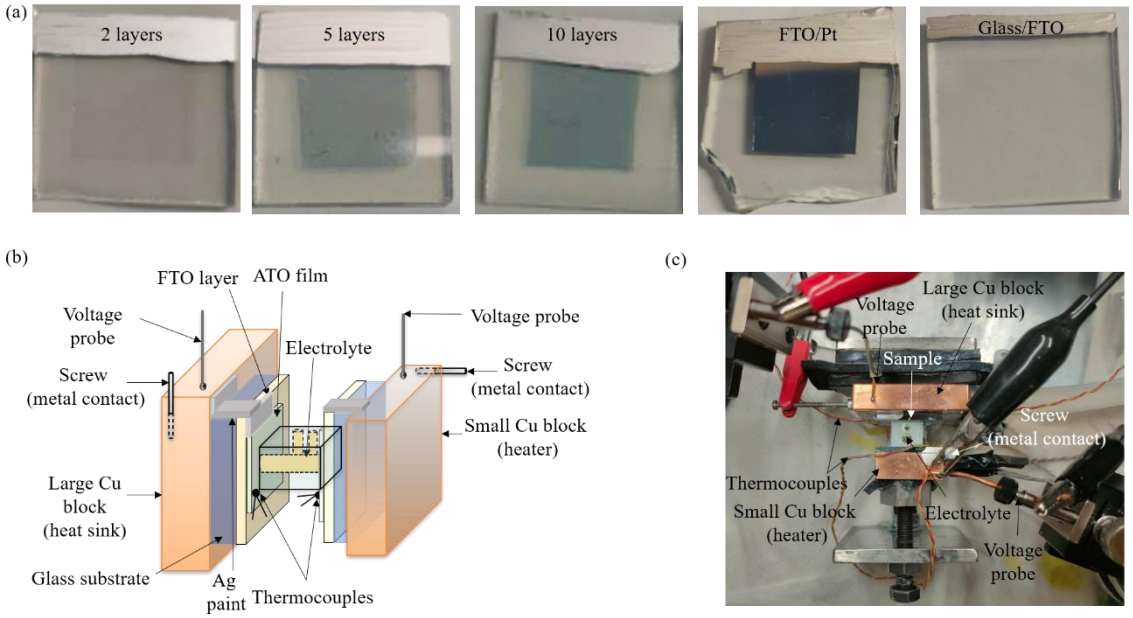

Fig. 5.2. (a) Different electrodes fabricated. (b) Scheme and (c) picture of the setup employed.

A custom setup was built up to characterize the fabricated TECs (see Fig. 5.2b, c). In order to establish a temperature difference in the setup, two copper blocks were employed. One of them, with 30 mm x 30 mm x 10 mm dimensions and 2 cartridge heaters inserted (Watlow, C1A-9604), acted as the heat source. The heaters were powered using a Keithley 2601 source meter. A second larger copper block (40 mm x 40 mm x 10 mm, Tangxi X00170O3IZ) with a water circulation channel was used as the heat sink. A water circulator (PolySicence, SD07R-20-A12E) was employed to circulate the water at a certain temperature along the Cu block.

The electrodes for each cell were centred on top of the copper blocks. Thermal grease (RS, 1938247) was used at all the glass/Cu interfaces to improve the thermal contacts. The electrodes were separated by a polytetrafluoroethylene (PTFE) cell which contained the electrolyte in a cylindrical channel of 10 mm length and 4 mm diameter. The channel connected to two top holes for the injection of the electrolyte. These holes were covered with tape after inserting the electrolyte to avoid evaporation (see Fig. 5.2b, c).

To avoid electrolyte leakage, two O-rings were located at the sides of the PTFE cell and were pressed against the electrodes by a system formed by stainless steel plates and screws. The area delimited by the O-rings, which determines the geometrical area A of the electrodes in contact with the electrolyte, was 0.5 cm^2. Two stainless steel screws inserted in the Cu blocks were used as electrical contacts for the current flow. In addition, two spring probes were contacted on top of the Cu blocks and were employed to sense the voltage (see Fig. 5.2b, c). The Cu blocks were electrically connected to the electrodes by extending the Ag paint (see Fig. 5.2b, c).

The temperature coefficient α, which indicates the variation of the open-circuit potential V_{oc} with the temperature difference, was obtained from the slope of a V_{oc} vs ΔT plot. The V_{oc} was measured with a Keithley 2100 nanovoltmeter, and the temperature difference was increased in steps of ≈2.5 K, from 0 up to ≈10 K, keeping the cold side temperature fixed at 25.0 ºC. Two K-type thermocouples (RS, 8140134) and a dual thermometer (RS, 123-2214) were used to monitor the hot (T_H) and cold-side (T_C) temperatures. The thermocouples were placed on top of the electrodes, close to the PTFE cell, with a bit of thermal grease at their tips for thermalisation (see Fig. 5.2b, c).

To evaluate the performance of the TECs, impedance spectroscopy (IS) was used. IS measurements were carried out at the V_{oc} value when the cells were under a ΔT=10 K (T_C=25.0 ºC) using an amplitude of 15 mV in a frequency range from 1 MHz to 1 mHz. A Metrohm-Autolab PGSTAT204 potentiostat equipped with a FRA32M frequency response analyzer controlled by Nova 1.11 software was used. ZView 3.5h was employed to fit the experimental impedance results to different equivalent circuits.

5.3. Results and discussion

Fig. 5.3 shows the SEM images of the different Sb:SnO_2 films prepared. It can be seen that the films are formed by interconnected nanoparticles of sizes below 10 nm. Also, pores are present with sizes not larger than c.a. 30 nm (see inset of Fig. 5.3a). The

thickness of the films can be estimated from the cross-sectional views (see Fig. 5.3b-d). For the films with 2, 5 and 10 layers, thickness values of 320, 550 and 1550 nm were found. It should be noted that the expected phase (cassiterite SnO_2) was previously identified by XRD experiments in our previous article [20]. Also, it can be seen in that reference that no changes in the XRD patterns were observed after the annealing process. Similarly, an EDX analysis from the same article showed no changes in the chemical composition of the film after the thermal treatment.

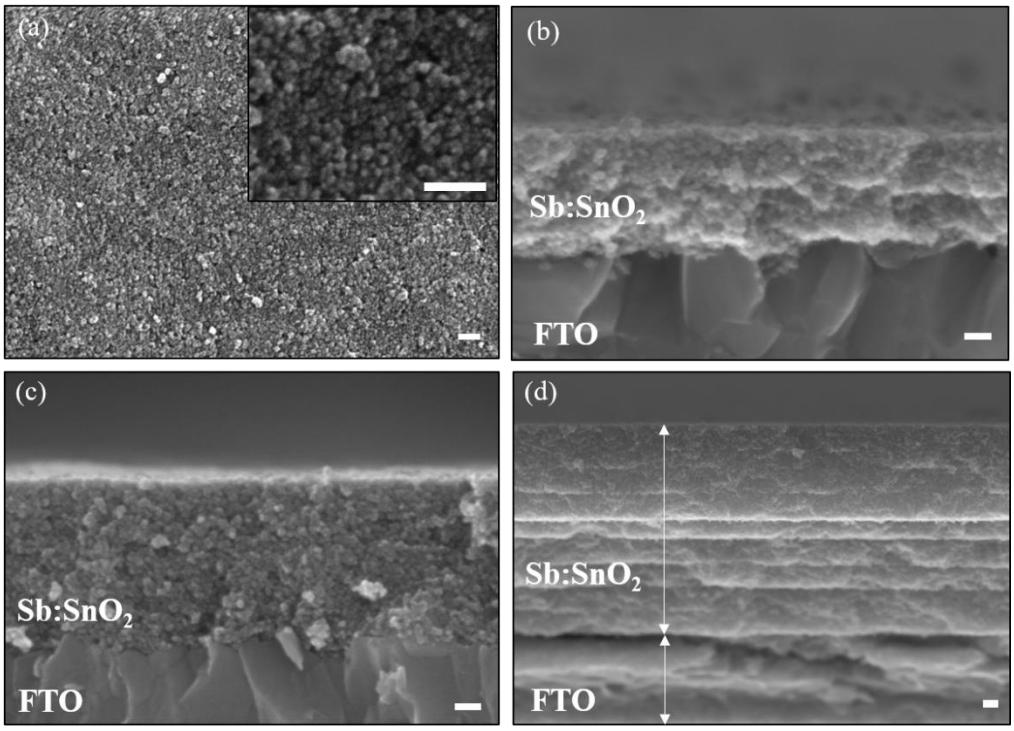

Fig. 5.3. SEM images of the different $Sb:SnO_2$ films prepared. (a) Top view of the sample with 5 layers. (b-d) Cross-sectional views of the 2, 5 and 10-layer films, respectively. All scale bars shown are 100 nm width.

To evaluate the performance of the different TECs prepared, IS measurements at the open-circuit voltage (under ΔT=10 K) were performed. Fig. 5.4 shows the results obtained for each cell with their corresponding fittings, performed using the equivalent circuits in the insets. The fitted parameters with their corresponding errors are shown in Table 5.1. For the TECs with the ATO and Pt electrodes, an equivalent circuit formed by a series resistance R_s (accounting for the cables, contacts and electrolyte resistances) and the finite-length Warburg impedance with a transmissive boundary (short circuit terminus W_s), both connected in series, was used (see Fig. 5.4a). The impedance of the W_s element is defined as $Z_{Ws}=R_{mt}\,(j\omega d^2/D)^{-p}\tanh[(j\omega d^2/D)^p]$, being R_{mt} the mass-transport resistance, related to the diffusion of the redox species to/from the electrodes, $j=(-1)^{0.5}$, ω the angular

frequency, *d* the diffusion length (distance between electrodes), *D* the diffusion coefficient of the redox species (assumed equal for both molecules) and *p* an exponent, which accounts for deviations from the ideal value (*p*=0.5) [21,22].

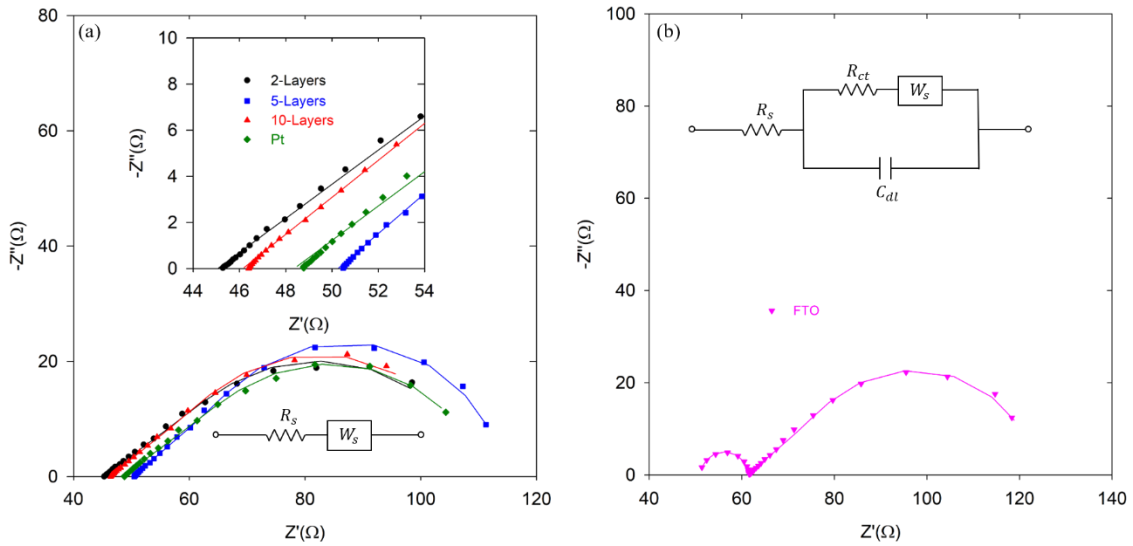

Fig. 5.4. Impedance results (Nyquist plots) for (a) the cells with the Sb:SnO_2 films and the Pt electrodes and (b) the FTO-only cell. The lines are the fittings performed using the equivalent circuits in the insets.

Table 5.1. Temperature coefficient (α), series (R_s) and charge-transfer (R_{ct}) resistances, double-layer capacitance (C_{dl}), mass-transfer resistance (R_{mt}), exponent (p) and R_{dc} of the different thermo-electrochemical cells when ΔT=10 K. Relative errors are shown between brackets. The maximum power output density (P_{max}) and the Carnot-related efficiencies (η_r) are also indicated.

	α (mV/K)	**R_s (Ω)**	**R_{ct} (Ω)**	**C_{dl} (μF)**	**R_{mt} (Ω)**	***p***	**R_{dc} (Ω)**	**P_{max} (mW/m²)**	**η_r (%)**
2 layers	1.20 (0.36%)	45.1 (0.12%)	-	-	64.6 (1.00%)	0.410 (0.66%)	110	6.55	0.040
5 layers	1.21 (0.89%)	50.3 (0.10%)	-	-	64.0 (0.53%)	0.459 (0.48%)	114	6.42	0.040
10 layers	1.24 (0.10%)	46.1 (0.13%)	-	-	63.0 (1.08%)	0.428 (0.66%)	109	6.80	0.042
FTO/ Pt	1.46 (0.19%)	48.4 (0.17%)	-	-	62.5 (0.98%)	0.408 (0.49%)	111	9.60	0.059
Glass /FTO	1.29 (0.13%)	51.2 (0.32%)	10.0 (1.73%)	0.603 (4.59%)	62.5 (0.97%)	0.46 (0.83%)	124	6.71	0.041

For the TEC with only FTO electrodes, two additional elements were added to the equivalent circuit, a charge-transfer resistance R_{ct}, related to the kinetics of the transfer of electrons between the redox species and the electrodes, and a double-layer capacitor, accounting for the accumulation of charge at the electrode/electrolyte interface (see Fig. 5.4b). These two elements (R_{ct} and C_{dl}) produce the semicircle observed in Fig. 5.4b,

which has also been observed before [23]. This semicircle is not present in the TECs with the ATO and Pt electrodes (Fig. 5.4a), which indicates a fast charge-transfer kinetics for the ATO TECs, similar to the Pt electrodes, which is a remarkable result, since this is not always the case for many electrode materials [19,24–27]. It should be noticed that the kinetics is not influenced by the electrode surface area, which increases with the ATO film thickness (number of layers), since a lack of a charge-transfer resistance is already observed in Fig. 5.4a for the thinnest film (2 layers, 320 nm). Related to the good kinetics, we found that Sb:SnO_2 has already been reported to display high faradaic currents on cyclic voltammograms when it was brought into contact with the ferro/ferricyanide electrolyte (same redox reaction) [28].

Fig. 5.4 and Table 5.1 also show similar values of R_s in all cases. This is expected, since the main contributions to R_s, the resistance of the substrate (FTO) and the electrolyte resistance, are both the same in all the systems [29]. Concerning the mass transport of the redox species (R_{mt}), all the values are again similar, which is expected since all the cells are formed by the same electrolyte and have the same interelectrode distance.

In order to compare the performance (power output at ΔT=10 K) of all the systems, the value of the temperature coefficient and the dc resistance R_{dc} was considered. This dc resistance governs the slope of the current-voltage (*I*-*V*) curve, and comprises the addition of all the resistances extracted from the impedance analysis ($R_{dc}=R_s+R_{ct}+R_{mt}$) [30]. In other words, the impedance spectroscopy analysis can extract all the different contributions behind the value of the slope of the *I*-*V* curve. Hence, if the values of the open-circuit voltage ($V_{oc}=\alpha\Delta T$) and R_{dc} are known, the maximum power density can be obtained as [$P_{max}=V_{oc}^2/(4AR_{dc})$] (see Fig. S5.2 and the values in Table 5.1) [30]. As shown in Table 5.1, the values obtained for α were very close to 1.24 mV/K in all cases, except for FTO/Pt that showed a somewhat larger value (1.46 mV/K). All the values agree with the literature for this electrolyte, which show variations from 1.2 to 1.6 mV/K [6,31].

Analysing the R_{dc} values, it can be seen from Table 5.1 that for all the systems, the value is very similar (≈110 Ω), except for the cell with only FTO, which shows a higher value due to the presence of the charge-transfer resistance. It is interesting to note that R_{dc} is basically the same for all the TECs with the ATO layers, and thus the maximum power density. Hence, no increase in P_{max} was obtained due to the increase of the electrode area in contact with the electrolyte, which significantly increases (from 2 to 5 and 10 layers).

This occurs since R_{ct} is negligible in all cases and R_{mt} is not affected by the surface area of the electrode, but by the electrolyte channel area. We would like to remark that it is expected that the electrolyte fully permeates the whole ATO electrode, due to its nanostructured and porous nature. In order to support this, we show in Fig. S5.1 how a solid electrolyte, with even higher viscosity than the ferro/ferricyanide aqueous electrolyte, can permeate an ATO film prepared by us under the same conditions.

The Carnot-related efficiencies of the TECs $\eta_r=\eta_{TEC}[\Delta T/T_H]$, being $\eta_{TEC}=P_{max}/(\kappa\Delta T/d)$, were also estimated, assuming the thermal conductivity of the electrolyte κ=0.5 W/(m K). It should be noted that this way of estimating the efficiency, although commonly used, can lead to values somewhat far from reality, since it neglects several heat-transfer processes that actually occur (e.g. conduction through the PTFE cell, convection and radiation, etc.) [32]. The η_r value obtained for the FTO/Pt TEC agrees well with the literature [30,31], and it is remarkable that with only 2 layers of ATO, a value in the same order of magnitude can be reached (see Table 5.1), at a much smaller cost.

5.4. Conclusions

We have fabricated thermo-electrochemical cells with nanostructured and porous Sb-doped tin oxide films deposited on F:SnO_2 (FTO) glasses as electrodes. Three different thickness of the films were evaluated (320, 550 and 1550 nm). The standard 0.4 M ferro/ferricyanide aqueous electrolyte was used. An impedance spectroscopy analysis under operating conditions revealed that the charge-transfer resistance was negligible for all the different thickness, indicating excellent kinetics, as it is the case for the typically employed expensive Pt electrodes. On the other hand, the temperature coefficients and the series and mass-transport resistances were similar, which led to similar power outputs. Hence, no performance improvements were obtained when the electrode area in contact with the electrolyte was significantly increased. The Carnot-related efficiencies estimated for the Sb:SnO_2 cells were in the same order of magnitude as for Pt electrodes. These results show Sb:SnO_2 as an excellent electrode material for thermo-electrochemical cells, providing similar performance than Pt at a much lower cost.

Authors contribution

Sergio Castro-Ruiz: methodology, validation, formal analysis, investigation, writing - original draft, visualization. **Jorge García-Cañadas**: conceptualization, methodology,

formal analysis, resources, writing - review and editing, visualization, supervision, project administration, funding acquisition.

Conflict of interest

The authors declare no conflict of interest.

Acknowledgements

This project has received funding from the European Union's Horizon 2020 research and innovation programme under grant agreement No 863222 (UncorrelaTEd project). Mauricio Solís and Lourdes Márquez are acknowledged for their technical support.

References

[1] Hassan Q, Abdulateef AM, Hafedh SA, Al-samari A, Abdulateef J, Sameen AZ, et al. Renewable energy-to-green hydrogen: A review of main resources routes, processes and evaluation. Int J Hydrogen Energy 2023;48:17383–408. https://doi.org/https://doi.org/10.1016/j.ijhydene.2023.01.175.

[2] Luberti M, Gowans R, Finn P, Santori G. An estimate of the ultralow waste heat available in the European Union. Energy 2022;238:121967. https://doi.org/https://doi.org/10.1016/j.energy.2021.121967.

[3] Kothari R, Tyagi V V, Pathak A. Waste-to-energy: A way from renewable energy sources to sustainable development. Renewable and Sustainable Energy Reviews 2010;14:3164–70. https://doi.org/https://doi.org/10.1016/j.rser.2010.05.005.

[4] Hur S, Kim S, Kim H-S, Kumar A, Kwon C, Shin J, et al. Low-grade waste heat recovery scenarios: Pyroelectric, thermomagnetic, and thermogalvanic thermal energy harvesting. Nano Energy 2023;114:108596. https://doi.org/https://doi.org/10.1016/j.nanoen.2023.108596.

[5] Zhou H, Inoue H, Ujita M, Yamada T. Advancement of Electrochemical Thermoelectric Conversion with Molecular Technology. Angewandte Chemie International Edition 2023;62:1–18. https://doi.org/https://doi.org/10.1002/anie.202213449.

[6] Duan J, Yu B, Huang L, Hu B, Xu M, Feng G, et al. Liquid-state thermocells: Opportunities and challenges for low-grade heat harvesting. Joule 2021;5:768–79. https://doi.org/https://doi.org/10.1016/j.joule.2021.02.009.

[7] Buckingham MA, Hammoud S, Li H, Beale CJ, Sengel JT, Aldous L. A fundamental study of the thermoelectrochemistry of ferricyanide/ferrocyanide: Cation, concentration, ratio, and heterogeneous and homogeneous electrocatalysis effects in thermogalvanic cells. Sustain Energy Fuels 2020;4:3388–99. https://doi.org/10.1039/d0se00440e.

[8] Li W, Ma J, Qiu J, Wang S. Thermocells-enabled low-grade heat harvesting: challenge, progress, and prospects. Mater Today Energy 2022;27:101032. https://doi.org/https://doi.org/10.1016/j.mtener.2022.101032.

[9] Romano MS, Li N, Antiohos D, Razal JM, Nattestad A, Beirne S, et al. Carbon nanotube-reduced graphene oxide composites for thermal energy harvesting applications. Advanced Materials 2013;25:6602–6. https://doi.org/10.1002/adma.201303295.

[10] Hu R, Cola BA, Haram N, Barisci JN, Lee S, Stoughton S, et al. Harvesting waste thermal energy using a carbon-nanotube-based thermo-electrochemical cell. Nano Lett 2010;10:838–46. https://doi.org/10.1021/nl903267n.

[11] Im H, Kim T, Song H, Choi J, Park JS, Ovalle-Robles R, et al. High-efficiency electrochemical thermal energy harvester using carbon nanotube aerogel sheet electrodes. Nat Commun 2016;7:10600. https://doi.org/10.1038/ncomms10600.

[12] Li W, Ma J, Qiu J, Wang S. Thermocells-enabled low-grade heat harvesting: challenge, progress, and prospects. Mater Today Energy 2022;27:101032–10150. https://doi.org/https://doi.org/10.1016/j.mtener.2022.101032.

[13] Zhang L, Kim T, Li N, Kang TJ, Chen J, Pringle JM, et al. High Power Density Electrochemical Thermocells for Inexpensively Harvesting Low-Grade Thermal Energy. Advanced Materials 2017;29:1605652–9. https://doi.org/10.1002/adma.201605652.

[14] Chen J, Wang Y, Li S, Chen H, Qiao X, Zhao J, et al. Porous Metal Current Collectors for Alkali Metal Batteries. Advanced Science 2023;10:2205695. https://doi.org/https://doi.org/10.1002/advs.202205695.

[15] Duan Y, Zheng J, Fu N, Fang Y, Liu T, Zhang Q, et al. Enhancing the performance of dye-sensitized solar cells: doping SnO 2 photoanodes with Al to simultaneously improve conduction band and electron lifetime. J Mater Chem A 2015;3:3066–73. https://doi.org/10.1039/C4TA05923A.

[16] Simon P, Gogotsi Y. Materials for electrochemical capacitors. Nat Mater 2008;7:845–54. https://doi.org/10.1038/nmat2297.

[17] Adegoke KA, Maxakato NW. Porous metal oxide electrocatalytic nanomaterials for energy conversion: Oxygen defects and selection techniques. Coord Chem Rev 2022;457:214389. https://doi.org/10.1016/J.CCR.2021.214389.

[18] Artyukhov D, Kiselev N, Boychenko E, Asmolova A, Zhelenov D, Artyukhov I, et al. High-Power-Density Thermoelectrochemical Cell Based on Ni/NiO Nanostructured Microsphere Electrodes with Alkaline Electrolyte. Nanomaterials 2023;13:2290–304. https://doi.org/10.3390/nano13162290.

[19] Zhuang X, Jin H, Dai S, Li X, Guo W, Wang Y, et al. Self-Assembled Asymmetric Electrodes for High-Efficiency Thermogalvanic Cells. Adv Energy Mater 2023;13:2302011–9. https://doi.org/https://doi.org/10.1002/aenm.202302011.

[20] Castro-Ruiz S, Márquez-García L, Solis-De la Fuente M, Beltrán-Pitarch B, Mota-Babiloni A, Vidan F, et al. Power factor improvement in a solid-liquid thermoelectric system formed by Sb:SnO2 in contact with a chromium complex solution. Sustain Energy Fuels 2023;7:4254–9. https://doi.org/10.1039/d3se00622k.

[21] Lazanas AC, Prodromidis MI. Electrochemical Impedance Spectroscopy-A Tutorial. ACS Measurement Science Au 2023;3:162–93. https://doi.org/10.1021/acsmeasuresciau.2c00070.

[22] Lasia A. Electrochemical impedance spectroscopy and its applications. Springer New York; 2014. https://doi.org/https://doi.org/10.1007/978-1-4614-8933-7.

[23] Yang P, Fan H. Electrochemical Impedance Analysis of Thermogalvanic Cells. Chem Res Chin Univ 2020;36:420–4. https://doi.org/10.1007/s40242-020-0126-y.

[24] Wang Y, Mukaida M, Kirihara K, Lyu L, Wei Q. Poly(3,4-Ethylene Dioxythiophene)/Poly(Styrene Sulfonate) Electrodes in Electrochemical Cells for

Harvesting Waste Heat. Energy Technology 2020;8:1900998. https://doi.org/https://doi.org/10.1002/ente.201900998.

[25] Wijeratne K, Ail U, Brooke R, Vagin M, Liu X, Fahlman M, et al. Bulk electronic transport impacts on electron transfer at conducting polymer electrode–electrolyte interfaces. Proc Natl Acad Sci U S A 2018;115:11899–904. https://doi.org/10.1073/pnas.1806087115.

[26] Wijeratne K, Vagin M, Brooke R, Crispin X. Poly(3,4-ethylenedioxythiophene)-tosylate (PEDOT-Tos) electrodes in thermogalvanic cells. J Mater Chem A Mater 2017;5:19619–25. https://doi.org/10.1039/c7ta04891b.

[27] Jung SM, Kwon J, Lee J, Han IK, Kim KS, Kim YS, et al. Cost-efficient nickel-based thermo-electrochemical cells for utilizing low-grade thermal energy. J Power Sources 2021;494:229705. https://doi.org/10.1016/j.jpowsour.2021.229705.

[28] Pellitero MA, Colina Á, Villa R, del Campo FJ. Antimony tin oxide (ATO) screen-printed electrodes and their application to spectroelectrochemistry. Electrochem Commun 2018;93:123–7. https://doi.org/10.1016/j.elecom.2018.06.012.

[29] Massetti M, Jiao F, Ferguson AJ, Zhao D, Wijeratne K, Würger A, et al. Unconventional Thermoelectric Materials for Energy Harvesting and Sensing Applications. Chem Rev 2021;121:12465–547. https://doi.org/10.1021/acs.chemrev.1c00218.

[30] Castro-Ruiz S, García-Cañadas J. Impedance Spectroscopy Analysis of a Thermo-Electrochemical Cell Under Operating Conditions. 2022 International Workshop on Impedance Spectroscopy (IWIS), 2022, p. 25–7. https://doi.org/10.1109/IWIS57888.2022.9975126.

[31] Quickenden TI, Mua Y. A Review of Power Generation in Aqueous Thermogalvanic Cells. J Electrochem Soc 1995;142:3985–93. https://doi.org/10.1149/1.2048446.

[32] Trosheva MA, Buckingham MA, Aldous L. Direct measurement of the genuine efficiency of thermogalvanic heat-to-electricity conversion in thermocells. Chem Sci 2022;13:4984–98. https://doi.org/10.1039/d1sc06340e.

Supplementary information

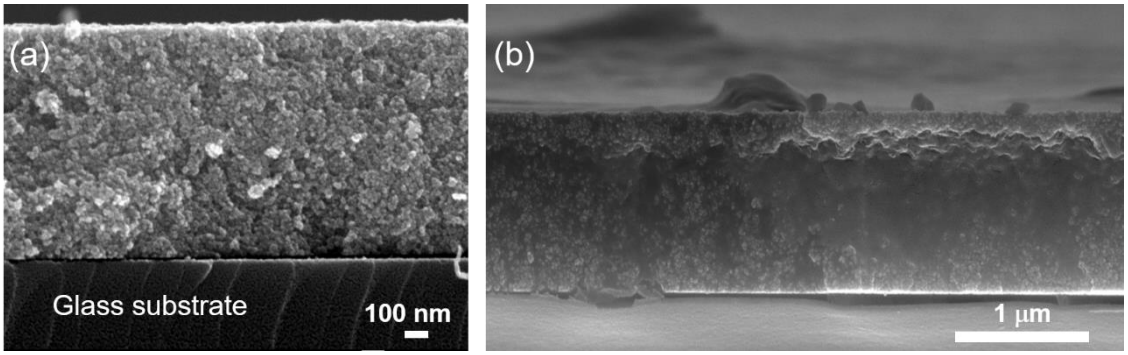

Fig. S5.1. SEM images of Sb:SnO_2 films (a) without and (b) with the addition of the solid electrolyte poly-diallyl dimethylammonium chloride (PDADMAC), which was added by drop casting a 20% wt. aqueous solution. After addition, it was left to dry overnight at room conditions, reaching a gel-like aspect. Image from ref. [1].

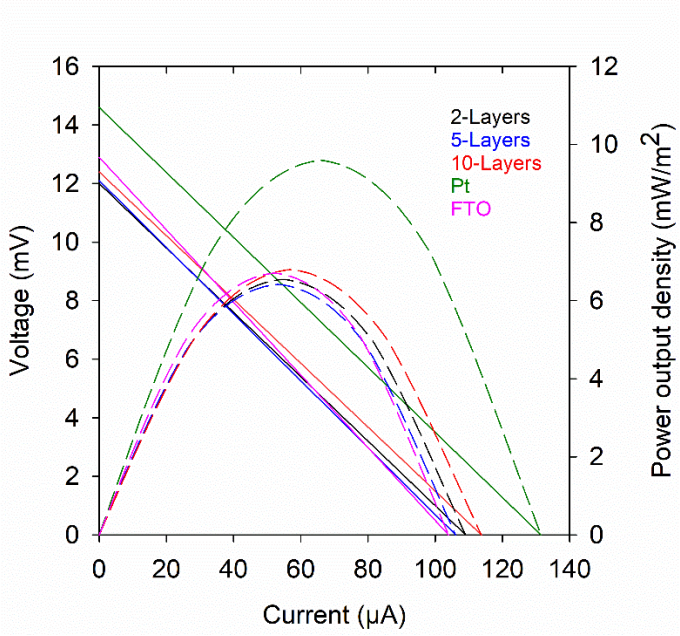

Fig. S5.2. Current-voltage (solid lines) and power output density-current (dashed lines) curves under a 10 K temperature difference (cold side temperature kept fixed at 25 ºC) for the cells with the Sb:SnO_2 films, the Pt electrodes, and the FTO-only cell.

References

[1] M. Solis-de la Fuente, S. Castro-Ruiz, L. Márquez-García, P. Rullière, S. Fantini, R. del Olmo, N. Casado, J. García-Cañadas. Large improvement in the power factor of a nanostructured and porous thermoelectric oxide using a solid electrolyte. Abstracts of the International Conference on Thermoelectrics 2023, Seattle (USA), 2023, 212. https://thermoelectric-conference.eu/admin/scripts/source/Book%20of%20Abstracts_ECT2023_final%20version.pdf.

6. Evaluation of in-plane architecture in a thermo-electrochemical cell with nanostructured and porous Sb:SnO_2 electrodes

Evaluation of in-plane architecture in a thermo-electrochemical cell with nanostructured and porous Sb:SnO_2 electrodes

S. Castro-Ruiz and J. García-Cañadas*

Department of Industrial Systems Engineering and Design, Universitat Jaume I, Av. Vicent Sos Baynat s/n, 12006 Castelló de la Plana, Spain.

* e-mail: garciaj@uji.es

Electrochemistry Communications. Under review.

Graphical abstract

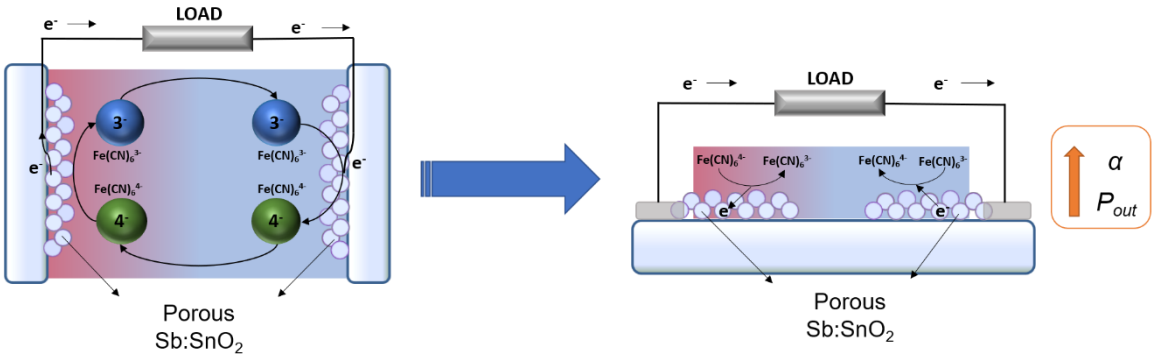

Fig. 6.1. Graphical abstract of the work: In-plane study of a thermo-electrochemical cell formed by nanostructured and porous Sb:SnO_2

Abstract

Thermo-electrochemical cells (TECs) are able to convert heat into electricity. They are formed by two electrodes (typically Pt) separated by a redox electrolyte (usually 0.4M aqueous ferro/ferricyanide). The widely adopted architecture of TECs consists of the two electrodes separated by an electrolyte channel. To our knowledge, no studies have been reported exploring a different architecture. Here, we evaluate an alternative configuration, which comprises a substrate with the two electrodes at its ends and with the electrolyte added on the top contacting both electrodes, forming a planar configuration. We explore first the use of the standard Pt electrodes deposited on top of a conductive glass substrate. Then, we replace the Pt by nanostructured and porous Sb-doped SnO_2. The planar configurations are compared with their corresponding typical architectures using the common ferro/ferricyanide electrolyte. It was found that the planar TEC with Sb:SnO_2 reached a temperature coefficient of 1.76 mV/K, higher than the value obtained in the standard configuration with Sb:SnO_2 (1.21 mV/K), and also higher than the planar architecture with Pt electrodes, which showed the typical value for the ferro/ferricyanide electrolyte (1.45 mV/K). As a consequence of this significantly larger value, a 29.7% higher maximum power output than the planar TEC with Pt was observed. Our study identifies for the first time interesting new features when a planar architecture is employed, opening the door to explore in more detail this alternative configuration in TECs.

6.1. Introduction

More than 60% of the global energy consumed is lost as waste heat, being more than 80% at low temperature (<100 ºC) [1]. Only a 10% recovery of this waste heat would exceed the summation of the current renewable energies [2]. On the other hand, different heat sources such as the sun or even our own bodies are widely spread and could provide enough amount of energy to power low-consumption sensors and wearable devices [3]. Hence, it would be highly beneficial to have a technology able to convert this vast amount of energy into electricity.

Thermo-electrochemical cells (TECs, or thermogalvanic cells or thermocells) are able to perform this by means of electrochemical processes [4]. They are formed by two electrodes separated by a redox electrolyte, which is typically a liquid or a gel. For this reason, they are intended for low temperature (<100 ºC) applications [5,6]. Unlike conventional thermoelectrics, they show larger open-circuit potential vs temperature difference ratios, typically in the order of mV/K. The open-circuit potential in these cells rises due to the temperature dependency of the redox potential of the electrolyte (thermogalvanic effect) [7]. The benchmark TEC is formed by two Pt electrodes at different temperatures contacted by a 0.4 M ferro/ferricyanide aqueous redox electrolyte. This redox couple exhibits a temperature coefficient α of 1.40 mV/K [8].

The widely adopted architecture of TECs consists of the two electrodes separated by an electrolyte channel. To our knowledge, no studies have been reported where a different architecture has been explored. Here, we evaluate an alternative configuration, which comprises a substrate with the two electrodes at its ends and the electrolyte is added on the top contacting both electrodes, forming a planar configuration. In our study, we explore first the use of the standard Pt electrodes deposited on top of a conductive glass substrate. Then, we replace the Pt by nanostructured and porous Sb-doped SnO_2 (ATO), which has been recently reported to be a suitable electrode material in TECs [9]. The planar configurations are compared with their corresponding typical architectures using the common ferro/ferricyanide electrolyte. Interesting new features were found that encourage the further exploration of this architecture in TECs.

6.2. Experimental section

Electrodes fabrication: Nanostructured and porous Sb:SnO_2 films were deposited on top of F-doped SnO_2 (FTO) glass substrates (Sigma Aldrich, 735167-EA) of 25 mm x 25

mm x 2.2 mm size, for the standard configuration, and 25 mm x 15 mm x 2.2 mm size for the in-plane case (see Fig. 6.2a). A previously described procedure was followed [10]. The substrates were cleaned before the ATO film deposition by means of three sonication steps of 15 min in different media. In the first step, sonication was performed using a soap (Labkem, SOAP-0685K0)/water solution (1:10 v/v). Then, distilled water to remove soap excess was used as second step. Finally, isopropanol (Labkem, PROL-P0P-5K0) media was employed for sonication. After this, substrates were dried under compressed air flow and treated in a UV-ozone cleaner (Ossila, L2002A2-UK) for 20 min. To avoid creating a short circuit in the planar configuration systems, two scratches were made on the FTO layer prior to the ATO deposition. These scratches were separated 3 mm, which is the separation distance between electrodes (see Fig. 6.2a). Subsequently, an Sb:SnO_2 colloidal aqueous dispersion (Keeling & Walker, A20W) was deposited by spin coating (Laurell, WS-650MZ-23NPPB) at 2500 rpm for 15 s, covering a centred area of the substrate of 15 mm x 15 mm, for the standard configurations, and the whole substrate, except the area that separates the electrodes, for the planar systems (see Fig. 6.2a). Five Sb:SnO_2 layers were deposited in all cases. After each layer deposition, a drying process was carried out on a hot plate at 100 ºC for 10 min. Finally, the films were annealed at 550 °C for 45 min in a furnace (Nabertherm, 400-1) with a 3 °C/min heating rate. The morphology of the films was analysed by scanning electron microscopy (SEM) using a JEOL 7001F instrument (Oxford Instruments).

On the other hand, Pt electrodes were prepared by depositing Pt (target from Aname, SC502-314C) by sputtering (Quorum, Q300T D Plus) on the abovementioned cleaned FTO glasses during 6 min. The dimensions and location of the films were identical to the case of the ATO samples above, and the scratches to separate 3 mm the electrodes in the planar configuration samples were also performed (see Fig. 6.2a).

Apart from the ATO and Pt electrodes, a bare FTO glass was also tested for comparison, which was also scratched as discussed. All the electrodes employed can be seen in Fig. 6.2a.

Cells preparation: Three different symmetrical cells were prepared in the standard configuration. One of them using the FTO/ATO electrodes, another one with the Pt films deposited onto FTO glass, and the final one using only FTO glass. To improve the electrical contact in this configuration, a certain top area of the samples was painted with Ag paint (RS, 186-3600), as shown in Fig. 6.2a. In addition to the standard configuration

cells, their corresponding planar versions were also prepared. In these cases, Ag paint was added at the ends of the electrodes and the 3 mm gap between electrodes was covered with tape to avoid contact with the electrolyte Fig. 6.2a). A solution of 0.4 M potassium ferrocyanide (Sigma Aldrich, P3289-100G) and 0.4 M potassium ferricyanide (Fluka, BCBT1564) in milli-Q water was employed as electrolyte in all the cells. All the chemicals were used as received.

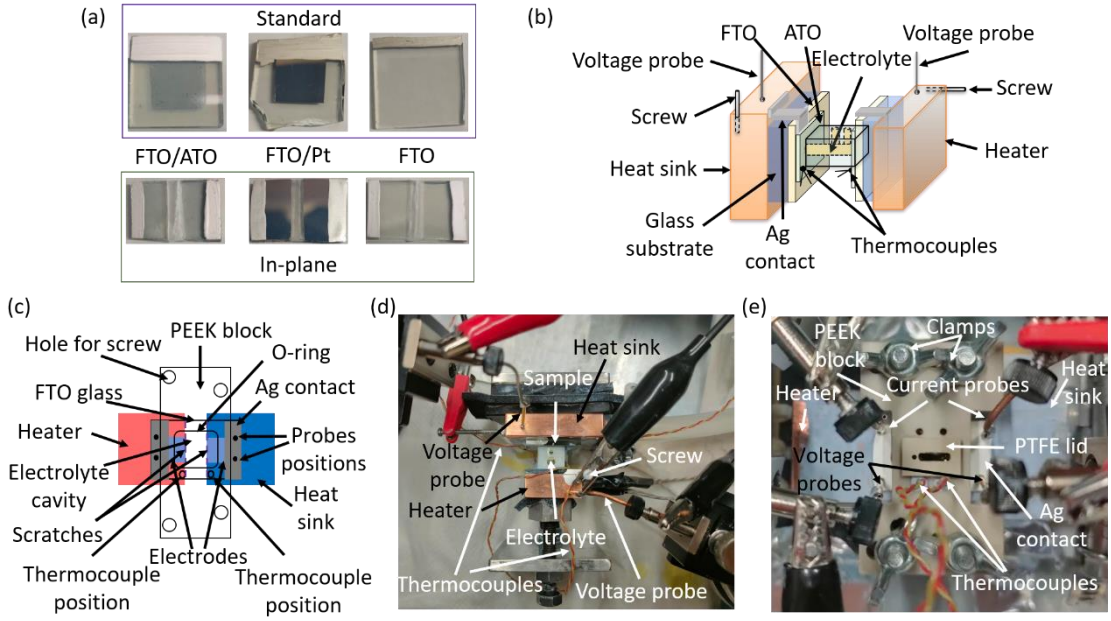

Fig. 6.2. (a) Different electrodes employed. (b,c) Schemes and (d,e) pictures of the setups employed.

Characterization setups: To characterize the TECs in standard configuration, a custom setup was employed (see Fig. 6.2b and d). In order to establish a temperature difference across the cell, two copper blocks were employed. One of them, with 30 mm x 30 mm x 10 mm dimensions and 2 cartridge heaters inserted (Watlow, C1A-9604), acted as the heat source. The heaters were powered using a Keithley 2601 source meter. A second larger copper block (Tangxi X00170O3IZ) of 40 mm x 40 mm x 10 mm dimensions with a water circulation channel was used as the heat sink. A water circulator (PolySicence, SD07R-20-A12E) served to circulate the water at a certain temperature along the Cu block.

The electrodes for each cell were centred on top of the copper blocks. Thermal grease (RS, 1938247) was used at all the glass/Cu interfaces to improve the thermal contacts. The electrodes were separated by a polytetrafluoroethylene (PTFE) piece which contained the electrolyte in a cylindrical channel of 10 mm length and 4 mm diameter.

The channel connected to two top holes for the injection of the electrolyte (see Fig. 6.2d). These holes were covered with tape after inserting the electrolyte to avoid evaporation.

To avoid electrolyte leakage, two O-rings of 8 mm internal diameter were located at the sides of the PTFE piece and were pressed against the electrodes by a system formed by stainless steel plates and screws. Two stainless steel screws inserted in the Cu blocks were used as electrical contacts for the current flow and two spring probes were contacted on top of the Cu blocks to sense the voltage (see Fig. 6.2b and d). The Cu blocks were electrically connected to the electrodes by Ag paint (see Fig. 6.2b and d).

On the other hand, a different setup was fabricated for the planar TECs. In order to establish the temperature difference in this setup, two metal blocks were employed. One of them made by Cu, with 30 mm x 30 mm x 10 mm dimensions and 3 cartridge heaters inserted (Watlow, C1A-9604), acted as the heat source. The heaters were also powered using a Keithley 2601 source meter. A second block made of Al of 30 mm x 30 mm x 12 mm dimensions (Flyphant 30B3334A) with a water circulation channel was used as the heat sink. The same water circulator (PolySicence, SD07R-20-A12E) was employed to circulate the water at a certain temperature along this block. The FTO substrates with the electrodes were placed on top of the metal blocks, which were separated 3 mm by a PTFE bridge (see Fig. 6.2c). The latter helps to avoid breaking the sample during the time a pressure is applied by an O-ring to allocate the liquid electrolyte. Thermal grease (RS, 2173835) was used at the substrate/metal block interfaces to improve the thermal contacts. It should be noted that the bridge length is the same as the gap between the electrodes.

A holed polyetheretherketone (PEEK) block with a rectangular O-ring at the bottom side was placed on top of the glass substrate to allow the location of the electrolyte (see Fig. 6.2c and e). The location of the O-ring pressing the film can be seen in Fig. 6.2c. Once the electrolyte was added, a PTFE lid was placed to avoid evaporation. The PEEK block also has holes for positioning two thermocouples and several screws to provide a gentle pressure to avoid electrolyte leakage. The electric contacts to the external circuit were made with four spring probes (RS, 261-5092) contacting on the Ag contacts, as shown in Fig. 6.2c. The area of each electrode in contact with the electrolyte for this setup was 8.5 mm x 4.5 mm.

Measurements: The temperature coefficient α, was obtained from the slope of an open-circuit voltage V_{oc} vs the temperature difference ΔT plot. The V_{oc} was measured

with a Keithley 2100 nanovoltmeter. The temperature difference was increased in steps of ≈2.5 K, from 0 up to ≈10 K, keeping the cold side temperature T_C fixed at 25.0 ºC. To monitor the temperature, two K-type thermocouples (RS, 814-0134) and a dual thermometer (RS,123-2214) were employed. The thermocouples were positioned on top of the electrodes in the standard setup (see Fig. 6.2b) and on top of the substrate, aligned with the ends of the metal blocks (see Fig. 6.2c), in the planar system. In both cases, a bit of thermal grease was applied at their tips for thermalization.

To evaluate the performance of the TECs, impedance spectroscopy was used. Impedance measurements were carried out oscillating around the V_{oc} value when the cells were under a ΔT=10 K (T_C=25.0 ºC) using an amplitude of 15 mV in a frequency range from 1 MHz to 1 mHz. A Metrohm-Autolab PGSTAT302N potentiostat equipped with a FRA32M frequency response analyser controlled by Nova 1.11 software was used. ZView 3.5h was employed to fit the experimental impedance results to different equivalent circuits.

6.3. Results and discussion

Fig. 6.3 shows SEM images of the ATO film employed. It can be seen that the film is formed by interconnected nanoparticles of sizes below 10 nm. Moreover, pores are present with sizes not larger than around 30 nm (see inset of Fig. 6.3a). A thickness value of 550 nm was estimated from the cross-sectional image (Fig. 6.3b). It should be noted that the expected phase (cassiterite SnO_2) was previously identified by XRD experiments in our previous article [10]. Also, it can be seen in that reference that no changes in the XRD patterns were observed after the annealing process. Similarly, an EDX analysis from the same article showed no changes in the chemical composition of the film after the thermal treatment.

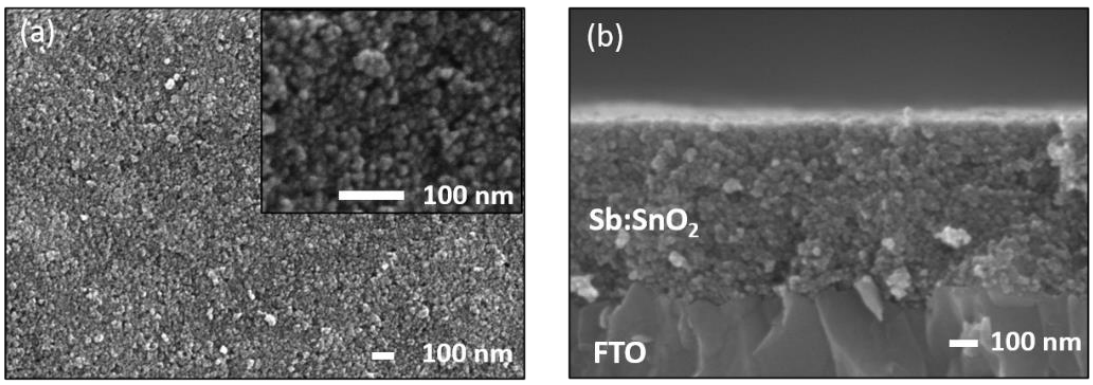

Fig. 6.3. (a) Top and (b) cross-sectional SEM images of an Sb:SnO_2 film prepared.

Fig. 6.4 shows the impedance results obtained for each cell with their corresponding fittings, performed using the equivalent circuits shown in the inset [9,11]. The fitted parameters with their corresponding errors are shown in Table 6.1. On the one hand, for the TECs with the ATO and Pt electrodes, either in standard or planar configuration, an equivalent circuit formed by a series resistance R_s (accounting for the cables, contacts and electrolyte resistances) and the finite-length Warburg impedance with a transmissive boundary (short-circuit terminus W_s), both connected in series, was used (see inset of Fig. 6.4a). The impedance of the W_s element is defined as $Z_{Ws}=R_{mt}(j\omega d^2/D)^{-p}\tanh[(j\omega d^2/D)^p]$, being R_{mt} the mass-transport resistance, related to the diffusion of the redox species to/from the electrodes, $j=(-1)^{0.5}$, ω the angular frequency, d the diffusion length, D the diffusion coefficient of the redox species (assumed equal for both molecules), and p an exponent, which accounts for deviations from the ideal value (p=0.5) [12,13].

On the other hand, when bare FTO glasses were used as electrodes two new elements in the equivalent circuit, a charge-transfer resistance R_{ct}, related to the kinetics of the transfer of electrons between the redox species and the electrodes, and a double-layer capacitor, accounting for the accumulation of charge at the electrode/electrolyte interface, were added to the previous equivalent circuit (see inset of Fig. 6.4b). These two elements (R_{ct} and C_{dl}) produce the semicircle observed at the left part in the Nyquist plots (see Fig. 6.4) [14]. In the case of the ATO and Pt electrodes, this semicircle does not appear, indicating good redox kinetics, as previously reported by our group [9].

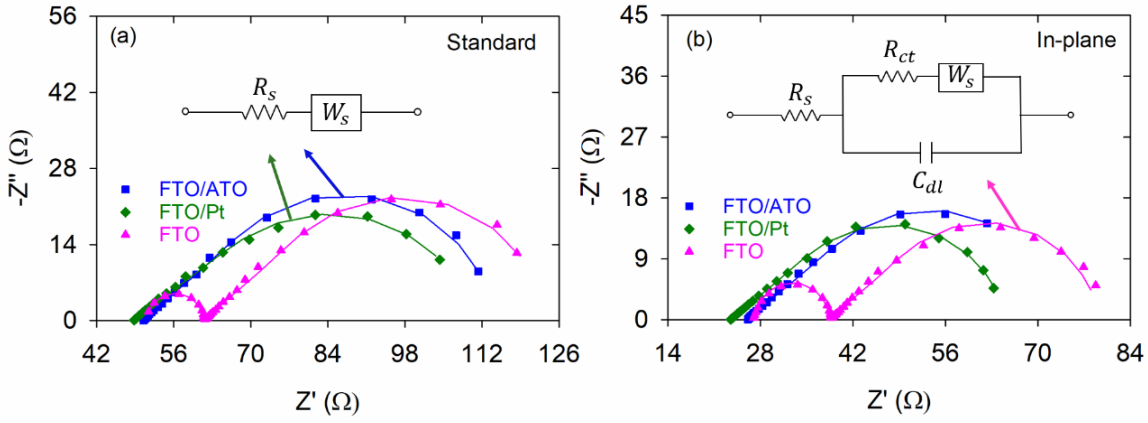

Fig. 6.4. Impedance spectra (Nyquist plots) for the cells in (a) standard and (b) in-plane configurations with Sb:SnO_2 (blue), Pt (green) and bare FTO (pink) electrodes. The lines correspond to the fittings performed.

Table 6.1. Temperature coefficient (α), series (R_s) and charge-transfer (R_{ct}) resistances, double-layer capacitance (C_{dl}), mass-transfer resistance (R_{mt}), exponent (p) and R_{dc} of the different thermo-electrochemical cells in both horizontal and in-plane configurations when ΔT=10 K. Relative errors are shown between brackets. The maximum power output (P_{max}) is also indicated.

	Electrodes	***α*** **(mV/K)**	***R_s*** **(Ω)**	***R_{ct}*** **(Ω)**	***C_{dl}*** **(μF)**	***R_{mt}*** **(Ω)**	***p***	***R_{dc}*** **(Ω)**	***P_{max}*** **(μW)**
Standard	FTO/ATO	1.21 (0.89%)	50.3 (0.10%)	-	-	64.0 (0.53%)	0.459 (0.48%)	114	0.321
	FTO/Pt	1.46 (0.19%)	48.4 (0.17%)	-	-	62.5 (0.98%)	0.408 (0.49%)	111	0.480
	FTO	1.29 (0.13%)	51.2 (0.32%)	10.0 (1.73%)	0.603 (4.59%)	62.5 (0.97%)	0.455 (0.83%)	124	0.335
In-plane	FTO/ATO	1.76 (0.41%)	25.9 (0.14%)	-	-	48.3 (0.85%)	0.430 (0.59%)	74	1.05
	FTO/Pt	1.45 (0.29%)	23.4 (0.11%)	-	-	41.8 (0.44%)	0.428 (0.42%)	65	0.809
	FTO	1.42 (0.22%)	27.3 (0.28%)	11.0 (0.88%)	0.493 (2.52%)	41.1 (0.90%)	0.442 (0.94%)	79	0.638

From the impedance analysis (Table 6.1), the different processes that govern the performance of the cells can be identified. First, it can be seen that the R_s values are similar within each configuration, which is expected since the electrolyte and dimensions of the different cell elements are similar. When comparing both configurations, a higher R_s value is found for the standard case, which we attribute to a larger electrolyte resistance due to the higher separation between electrodes (10 mm in the standard case vs 3 mm in the planar configuration).

Regarding the mass transport, R_{mt} values are again similar within the cells of each configuration, as expected, since the same electrolyte is used. However, this is not the case for the system with ATO electrodes in in-plane configuration, which shows a R_{mt} value around 7 Ω higher than the other two planar cells. This could be due to the somewhat more difficult diffusion of the redox species within the nanostructured and porous morphology of the electrodes in the direction parallel to the substrate. In the standard configuration, the diffusion basically takes place in the direction perpendicular to the electrode. When comparing both configurations, again higher R_{mt} values are

observed for the standard case (see Table 6.1), which we also attribute to the larger inter-electrode distance.

If we analyse now the different temperature coefficient values shown in Table 6.1, a significantly higher value of 1.76 mV/K was measured for the ATO system in planar configuration, which is 21.4% higher than the value found for the cell with Pt electrodes in the same configuration (1.45 mV/K), which is in agreement with the standard value reported for this electrolyte (1.40 mV/K). Although we cannot find a clear explanation for this significant increase at this stage, we think that it might be related to the restrictions that the redox species can find when located within the intricated porous structure of the ATO film. In the standard configuration, where the temperature coefficient was 1.21 mV/K, the length of the diffusion path of the species within the ATO electrode is very short, since the film thickness is 550 nm. However, due to the change in orientation, in the planar configuration the diffusion paths can reach a few mm (electrodes length is 4.5 mm) when moving in the direction parallel to the substrate, which is a much higher value. This suggestion is in agreement with the higher R_{mt} value found discussed above. In any case, further studies will be conducted to try to explain in more detail this new effect observed.

In order to analyse the performance of the different cells, the current-voltage *I-V* curves and the power output were obtained at ΔT=10 K (see Fig. 6.5). For the determination of the *I-V* curves the values of the V_{oc} and the dc resistance R_{dc} were considered. This dc resistance, which comprises the addition of all the resistances extracted from the impedance analysis ($R_{dc}=R_s+R_{ct}+R_{mt}$), governs the slope of the *I-V* curve (see values in Table 6.1) [9,11]. Hence, if the open-circuit voltage ($V_{oc}=\alpha\Delta T$) and R_{dc} are known, the *I-V* curves and the maximum power [$P_{max}=V_{oc}^2/(4R_{dc})$] can be obtained (Fig. 6.5 and Table 6.1). When comparing the cells in planar configuration, it can be observed that a 29.7% higher P_{max} can be reached in the ATO cell than in the Pt case. This is due to the larger temperature coefficient, despite having a somewhat higher R_{mt}.

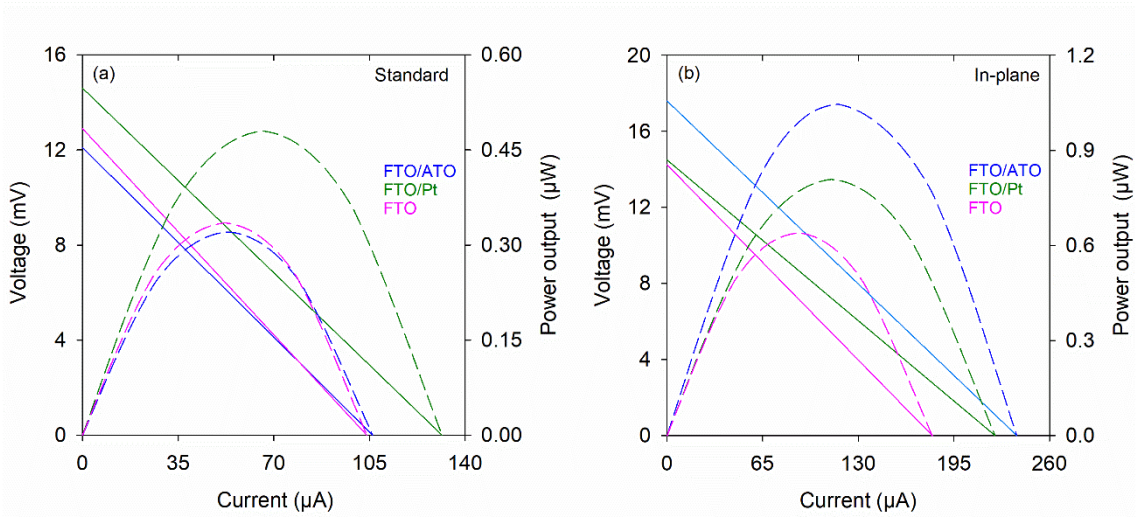

Fig. 6.5. Current-voltage (solid lines) and power output-current (dashed lines) curves under a 10 K temperature difference (cold side temperature kept fixed at 25 ºC) for the cells with the Sb:SnO_2 films, the Pt electrodes, and the FTO-only cell in both configurations.

It should be noticed that larger P_{max} values were obtained in all the in-plane systems when compared to their corresponding standard cells. However, this is not a fair comparison since the dimensions of both systems differ and the transport of the redox species is not exclusively one-dimensional in the in-plane architecture, as it is in the standard case.

6.4. Conclusions

An analysis of a new architecture for a thermo-electrochemical cell has been performed. Unlike the standard configuration where a redox electrolyte is sandwiched by two similar electrodes (typically Pt), the new architecture comprises a substrate (FTO glass) with the two electrodes deposited at its ends and the 0.4M aqueous ferro/ferricyanide electrolyte added on the top contacting both electrodes, forming a planar configuration. Different cells were prepared using Pt films and nanostructured and porous Sb-doped SnO_2 electrodes in both architectures (standard and in-plane). Interestingly, a significantly higher temperature coefficient was found for the in-plane configuration when Sb:SnO_2 was used as electrode (1.76 mV/K), higher than the value obtained in the standard configuration with Sb:SnO_2 (1.21 mV/K), and also higher than the planar architecture with Pt electrodes, which showed the typical value for the ferro/ferricyanide electrolyte (1.45 mV/K). An analysis of these systems by impedance spectroscopy revealed that the main difference between the cells with planar configuration relies on a somewhat higher mass-transport resistance found for the

Sb:SnO_2 system. In any case, the temperature coefficient improvement was more relevant and the maximum power output for the in-plane Sb:SnO_2 cell was 29.7% higher than when using the typical Pt electrodes. Our study identifies for the first time interesting new features when a planar architecture is employed, opening the door to explore in more detail this alternative configuration.

Authors contributions

Sergio Castro-Ruiz: methodology, validation, formal analysis, investigation, writing - original draft, visualization. Jorge García-Cañadas: conceptualization, methodology, formal analysis, resources, writing - review and editing, visualization, supervision, project administration, funding acquisition.

Conflict of interest

The authors declare no conflict of interest.

Acknowledgements

This project has received funding from the European Union's Horizon 2020 research and innovation programme under grant agreement No 863222 (UncorrelaTEd project).

References

[1] International Energy Agency. World Energy Outlook. 2023.

[2] Renewable Energy Agency I. Renewable Power Generation Costs in 2022. 2023.

[3] Farhat O, Faraj J, Hachem F, Castelain C, Khaled M. A recent review on waste heat recovery methodologies and applications: Comprehensive review, critical analysis and potential recommendations. Clean Eng Technol 2022;6:100387–409. https://doi.org/10.1016/j.clet.2021.100387.

[4] Liu Y, Cui M, Ling W, Cheng L, Lei H, Li W, et al. Thermo-electrochemical cells for heat to electricity conversion: from mechanisms, materials, strategies to applications. Energy Environ Sci 2022;15:3670–87. https://doi.org/10.1039/d2ee01457b.

[5] Li W, Ma J, Qiu J, Wang S. Thermocells-enabled low-grade heat harvesting: challenge, progress, and prospects. Mater Today Energy 2022;27:101032–10150. https://doi.org/https://doi.org/10.1016/j.mtener.2022.101032.

[6] Duan J, Yu B, Huang L, Hu B, Xu M, Feng G, et al. Liquid-state thermocells: Opportunities and challenges for low-grade heat harvesting. Joule 2021;5:768–79. https://doi.org/https://doi.org/10.1016/j.joule.2021.02.009.

[7] Qian X, Ma Z, Huang Q, Jiang H, Yang R. Thermodynamics of Ionic Thermoelectrics for Low-Grade Heat Harvesting. ACS Energy Lett 2024:679–706. https://doi.org/10.1021/acsenergylett.3c02448.

[8] Dupont MF, MacFarlane DR, Pringle JM. Thermo-electrochemical cells for waste heat harvesting-progress and perspectives. Chemical Communications 2017;53:6288–302. https://doi.org/10.1039/c7cc02160g.

[9] Castro-Ruiz S, García-Cañadas J. Nanostructured and porous antimony-doped tin oxide as electrode material for the heat-to-electricity energy conversion in thermo-electrochemical cells. Electrochem Commun 2024;161:107683–9. https://doi.org/10.1016/j.elecom.2024.107683.

[10] Castro-Ruiz S, Márquez-García L, Solis-De la Fuente M, Beltrán-Pitarch B, Mota-Babiloni A, Vidan F, et al. Power factor improvement in a solid-liquid thermoelectric system formed by Sb:SnO2 in contact with a chromium complex solution. Sustain Energy Fuels 2023;7:4254–9. https://doi.org/10.1039/d3se00622k.

[11] Castro-Ruiz S, García-Cañadas J. Impedance Spectroscopy Analysis of a Thermo-Electrochemical Cell Under Operating Conditions. 2022 International Workshop on Impedance Spectroscopy (IWIS), 2022, p. 25–7. https://doi.org/10.1109/IWIS57888.2022.9975126.

[12] Lazanas AC, Prodromidis MI. Electrochemical Impedance Spectroscopy-A Tutorial. ACS Measurement Science Au 2023;3:162–93. https://doi.org/10.1021/acsmeasuresciau.2c00070.

[13] Lasia A. Electrochemical impedance spectroscopy and its applications. Springer New York; 2014. https://doi.org/https://doi.org/10.1007/978-1-4614-8933-7.

[14] Yang P, Fan H. Electrochemical Impedance Analysis of Thermogalvanic Cells. Chem Res Chin Univ 2020;36:420–4. https://doi.org/10.1007/s40242-020-0126-y.

7. Discussion and general conclusions

General conclusions

The main objective of this thesis has been to implement different electrochemical strategies in porous materials to improve the conversion of heat into electricity. This objective has been achieved, and the principal conclusions are as follows:

1. An extension of our previously published solid-liquid thermoelectric (TE) system was carried out. Unlike the electrolytes previously employed, we have used an electrolyte containing an electroactive molecule (chromium acetylacetonate) dissolved in 3-methoxypropionitrile solvent. The electrolyte permeated a nanostructured and porous Sb-doped SnO_2 film. An average power factor (*PF*) improvement of 3.4 times was achieved due to the presence of the electrolyte. The enhancement originated from an average decrease of 23.2% and 82.8% in the absolute value of the Seebeck coefficient (*S*) and the electrical resistivity (*R*) of the solid, respectively. Morphological changes and variations in the chemical composition of the films were not observed by SEM and EDX analysis. An impedance spectroscopy (IS) study concluded that the *PF* improvements are related to the donation of electrons from the electrolyte to the solid, which increases its electrical conductivity (σ) and the consequent drop in the *S* coefficient (see Chapter 3).

2. It is demonstrated that IS technique is capable to characterize the main mechanisms behind the performance of a standard thermo-electrochemical cell (TEC), fabricated with Pt electrodes and 0.4 M ferro/ferricyanide aqueous electrolyte under operating conditions. A simplified Randles equivalent circuit was used to fit the impedance response at the open-circuit voltage value of the TEC under a temperature difference (ΔT) of 40 K. From the fitting, the resistance at steady state (R_{dc}) was calculated as the addition of the series (R_s) and mass transport (R_{mt}) resistances ($R_{dc}=R_s+R_{mt}$). It was found that the steady-state resistance ($R_{I\text{-}V}$) obtained from the current-voltage (*I*-*V*) curve, matches well with R_{dc}. Hence, knowing R_{dc} and the open-circuit voltage (V_{oc}) at the given ΔT, the *I*-*V* curve can be determined, as well as the power output (P_{out}), which can reduce a significant amount of time in many cases (see Chapter 4).

3. It has been proved that nanostructured and porous Sb-doped SnO_2 is an excellent electrode material for TECs, providing similar performance than Pt at a much lower cost when both are in contact with the standard 0.4 M potassium

ferro/ferricyanide aqueous electrolyte. An IS analysis under operating conditions revealed that the R_{ct} was negligible for all the different thickness, indicating excellent kinetics, as it is the case for the typically employed expensive Pt electrodes. On the other hand, the temperature coefficients, R_s and R_{mt} were similar, which led to similar P_{outs}. Hence, no performance improvements were obtained when the electrode area in contact with the electrolyte was significantly increased. The Carnot-related efficiencies (η_r) estimated for the Sb:SnO_2 cells were in the same order of magnitude as for Pt electrodes (see Chapter 5).

4. A new architecture including a substrate (FTO glass) with the two electrodes deposited at its ends and the usual 0.4 M aqueous ferro/ferricyanide electrolyte added on the top contacting both electrodes, forming a planar configuration has been studied. This new configuration differs from the standard configuration where a redox electrolyte is sandwiched by two similar electrodes (typically Pt). Different TECs well prepared using either Pt or nanostructured and porous Sb-doped SnO_2 electrodes in both standard and planar configurations. Remarkably, a significantly higher temperature coefficient was found for the in-plane configuration when Sb:SnO_2 was used as electrode (1.76 mV/K). This value is higher than the one observed in the standard configuration with the same material (1.21 mV/K), and also 29.7% larger than the planar architecture with Pt electrodes, which showed the typical value for the ferro/ferricyanide electrolyte (1.45 mV/K). An impedance spectroscopy study revealed that the main difference found rely on a somewhat higher mass-transport resistance found for the Sb:SnO_2 system in planar configuration. In conclusions, our study identifies for the first time interesting new features when a planar architecture is employed, opening the door to explore in more detail alternative configurations in TECs (see Chapter 6).

General conclusions (Spanish version)

El principal objetivo de esta tesis ha sido implementar diversas estrategias electroquímicas en materiales porosos para mejorar la conversión de calor en electricidad. Este objetivo se ha conseguido, dando como resultado las principales conclusiones que se exponen a continuación:

1. Se ha realizado una extensión de nuestro sistema termoeléctrico (TE) sólido-líquido previamente publicado. A diferencia de los electrolitos anteriormente empleados, se han utilizado una molécula electroactiva (acetilacetonato de cromo) disuelta en 3-metoxipropionitrilo. El electrolito impregnó una película de SnO_2 dopado con antimonio. Como resultado, se obtuvieron mejoras de 3.4 veces de media en el factor de potencia (*PF*) debido a la presencia del líquido. Esta mejora fue alcanzada debido a la reducción media del 23.2% que sufrió el valor absoluto del coeficiente de Seebeck (*S*) y al decrecimiento medio de la resistencia eléctrica (*R*) del sólido, respectivamente. Tras el análisis con técnicas microscópicas como SEM y EDX, no se encontraron cambios morfológicos ni variaciones en la composición química. Sin embargo, un estudio por espectroscopía de impedancia (IS) reveló que las mejoras del *PF* encontradas se debían a un efecto de donación electrónica desde el electrolito hacia el sólido, que da como resultado un incremento en la conductividad eléctrica (σ) junto con la consecuente disminución del *S* (ver capítulo 3).

2. Se ha demostrado que la técnica IS es capaz de caracterizar los principales mecanismos detrás del funcionamiento de una celda termo-electroquímica (TEC) estándar, fabricada con electrodos de Pt y en contacto con una disolución acuosa 0.4 M de ferro/ferricianuro potásico. Se utilizó un circuito equivalente de Randles simplificado para ajustar la respuesta de impedancia en el valor de voltaje de circuito abierto del TEC bajo una diferencia de temperatura (ΔT) de 40 K. A partir del ajuste, la resistencia total del sistema (R_{dc}) se calculó como la suma de la resistencia en serie. (R_s) y las resistencias de transporte de masa (R_{mt}) ($R_{dc} = R_s + R_{mt}$). Además, se encontró que la resistencia bajo estado estacionario ($R_{I\text{-}V}$) obtenida de la curva corriente-voltaje (*I-V*), coincide bien con R_{dc}. Por lo tanto, conociendo R_{dc} y el voltaje de circuito abierto (V_{oc}) a cada ΔT, se puede determinar la curva *I-V*, así como la potencia (P_{out}), de la TEC, lo que puede reducir una cantidad significativa de tiempo en muchos casos (ver Capítulo 4).

3. Se ha probado que el material SnO_2 dopado con Sb nanoestructurado y poroso es un excelente material electródico para una TEC, que proporciona un rendimiento similar al del Pt a un costo mucho menor cuando ambos están en contacto con una disolución acuosa 0.4 M de ferro/ferricianuro potásico. Un análisis de IS en condiciones operativas reveló que el R_{ct} era insignificante para todos los diferentes espesores, lo que indica una cinética rédox excelente, como en el caso de los costosos electrodos de Pt típicamente empleados. Por otro lado, los coeficientes de temperatura, R_s y R_{mt}, fueron similares, lo que condujo a P_{outs} similares. Por lo tanto, no se obtuvieron mejoras de rendimiento cuando se aumentó significativamente el área del electrodo en contacto con el electrolito. Las eficiencias relacionadas con el principio de Carnot (η_r) estimadas para los sistemas con $Sb:SnO_2$ fueron del mismo orden de magnitud que para los electrodos de Pt (ver Capítulo 5).

4. Se ha estudiado por primera vez, una nueva arquitectura planar en una celda termo-electroquímica, que incluye un substrato conductor (cristal recubierto con óxido de titanio dopado con flúor, FTO) con dos electrodos depositados en sus extremos, sobre los cuales se ha contactado una disolución acuosa 0.4 M de ferro/ferricianuro potásico. Este sistema difiere del empleado típicamente en este campo que consta de un electrolito insertado entre dos electrodos similares (normalmente Pt). Se han preparado diferentes celdas tanto con Pt como con SnO_2 dopado con antimonio nanoestructurado y poroso en ambas configuraciones (estándar y planar). Como resultado, se observó un valor de coeficiente de temperatura notablemente alto (1.76 mV/K) para la arquitectura planar con $Sb:SnO_2$ como electrodo. Este valor es mayor que el observado para la configuración estándar con el mismo material electródico (1.21 mV/K), y es hasta un 29.7 % más alto que el valor encontrado para la configuración planar con electrodos de Pt (1.45 mV/K). Tras un estudio por espectroscopía de impedancia, se observó que la principal diferencia era un valor inusualmente alto de la resistencia al transporte de masa en el sistema planar con $Sb:SnO_2$. En conclusión, nuestro estudio ha identificado interesantes nuevas características cuando una arquitectura planar ha sido empleado, abriendo la puerta al estudio de nuevas configuraciones en el campo de las celdas termo-electroquímicas (ver Capítulo 6).

List of figures

List of tables

UNIVERSITAT JAUME·I